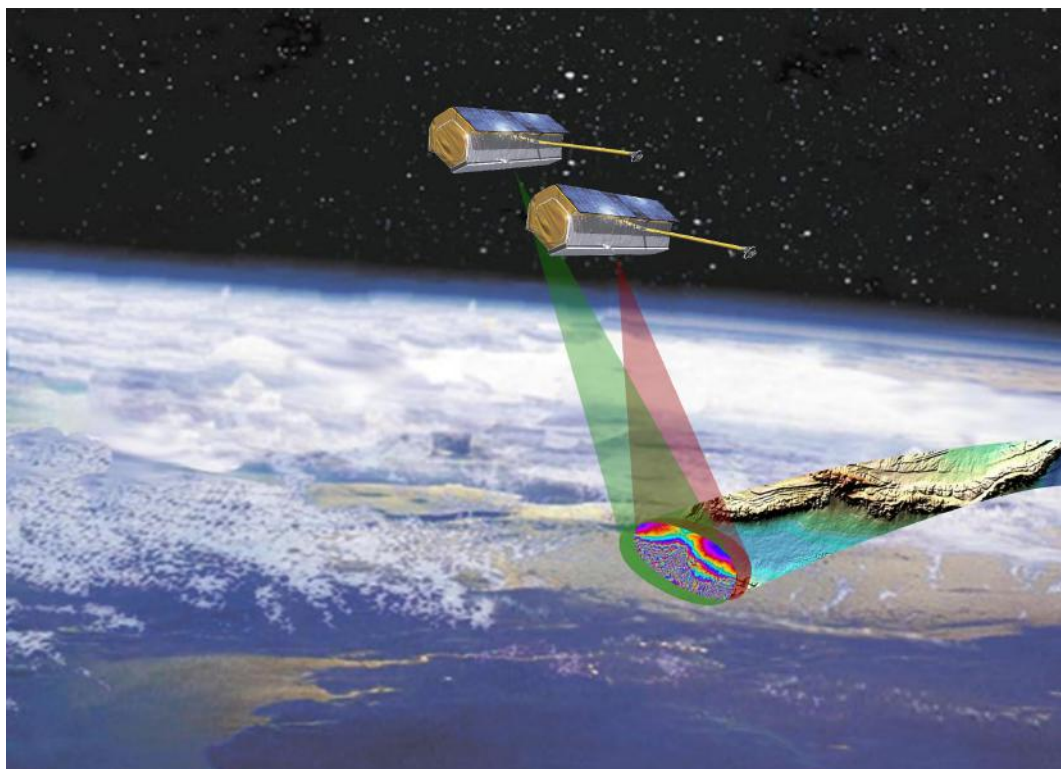


# Satellite Formation Flying for High-Precision Earth Observation

Pol Francesch Huc, Sydney Hsu



AA 279D - Spacecraft Formation-Flying and Rendezvous  
Stanford University

## Revision History

Rev	Changes
PS1	- Created document - Added problem set 1 material
PS2	- Added problem set 2 material - Revised PS1 orbital elements and updated document accordingly
PS3	- Added problem set 3 material
PS4	- Added problem set 4 material
PS5	- Added problem set 5 material
PS6	- Added problem set 6 material
PS7	- Added problem set 7 material - Finalized impulsive control and updated sections 5.2
PS8	- Added problem set 8 material
PS9	- Added problem set 9 material - Updated problem set 1–8 - Initial conditions made consistent throughout for final project submission

## Contents

<b>0 Scope</b>	<b>11</b>
<b>1 Problem Set 1</b>	<b>11</b>
1.1 Mission Overview . . . . .	11
1.1.a Reference Mission . . . . .	11
1.1.b Mission Objectives . . . . .	11
1.1.c Spacecraft Specification . . . . .	12
1.1.d Launch and Orbit . . . . .	13
1.1.e Synthetic Aperture Radar Payload . . . . .	14
1.1.f Key Dynamics, Guidance, Navigation & Control Requirements . . . . .	14
1.2 Orbit Simulation, Review of Astrodynamics . . . . .	15
1.2.a Initial Orbital Elements . . . . .	15
1.2.b Initial Position and Velocity . . . . .	15
1.2.c Numerical Simulations of Unperturbed and J2 Propagation . . . . .	16
1.2.d Numerical and Analytical Comparison of the Unperturbed Orbit . . . . .	16
1.2.e Numerical Simulation of Osculating Orbital Elements . . . . .	18
1.2.f Mean Classical Orbital Elements . . . . .	20
1.2.g Reconciling Osculating and Mean Orbital Elements . . . . .	22
<b>2 Problem Set 2</b>	<b>23</b>
2.1 Everything is Relative . . . . .	23
2.1.a Chief and Deputy Orbit Initialization . . . . .	23
2.1.b Numerical Integration of Relative Equations of Motion . . . . .	23
2.1.c Analytical Solution to Fundamental Orbital Differential Equations . . . . .	25
2.1.d Numerical and Analytical Comparison . . . . .	27
2.1.e Drift Correction Maneuver . . . . .	29
2.1.f Maneuver Simulation . . . . .	30
<b>3 Problem Set 3</b>	<b>32</b>
3.1 Problem 1: We are Close in Near-Circular Orbits . . . . .	32
3.1.a Initial Conditions . . . . .	32

3.1.b	Initial Position and Velocity . . . . .	32
3.1.c	Hill-Clohessy-Wilshire Integration Constants . . . . .	32
3.1.d	HCW in Rectilinear Coordinates . . . . .	33
3.1.e	HCW in Rectilinear Coordinates . . . . .	34
3.2	Problem 2: We are Close in Eccentric Orbits . . . . .	35
3.2.a	Initial Conditions . . . . .	35
3.2.b	Yamanaka-Ankersen Integration Constants . . . . .	35
3.2.c	Yamanaka-Ankersen Solution . . . . .	36
3.2.d	Discussion of YA Solution . . . . .	38
3.2.e	Quasi-Nonsingular Relative Orbit Elements . . . . .	38
3.2.f	Relative Orbital Elements Geometric Linear Mapping . . . . .	39
3.2.g	Relationship between Relative Orbital Elements and YA Integration Constants . .	41
3.2.h	True Relative Propagation . . . . .	42
3.2.i	Difference in Semi-major Axis & Highly Eccentric Orbits . . . . .	44
<b>4</b>	<b>Problem Set 4</b>	<b>48</b>
4.1	Problem 1: These are Relative Orbits! . . . . .	48
4.1.a	Chief Osculating Initial Conditions . . . . .	48
4.1.b	Deputy Initial Conditions . . . . .	48
4.1.c	Numerical Integration of Unperturbed and J2-perturbed Propagation . . . . .	48
4.1.d	Relative Position in RTN for Unperturbed and J2-perturbed Propagation . . . . .	51
4.1.e	Osculating and Mean Relative Orbital Elements . . . . .	52
4.1.f	Removing J2 Drift . . . . .	53
4.1.g	Simulation without J2 Drift . . . . .	54
4.1.h	Linearized Analytical STM for J2 Effects . . . . .	55
<b>5</b>	<b>Problem Set 5</b>	<b>57</b>
5.1	Control Objectives . . . . .	57
5.1.a	Formation Operational Modes . . . . .	57
5.1.b	Definition of Operational Modes . . . . .	57
5.1.c	Control Requirements . . . . .	58
5.1.d	Reconfiguration Requirements . . . . .	58

5.1.e	Control Actuators . . . . .	58
5.1.f	Dynamics Models . . . . .	59
5.2	Formation Reconfiguration . . . . .	62
5.2.a	Delta-v Lower Bounds . . . . .	62
5.2.b	Least-squares with maneuver placement . . . . .	62
5.2.c	Double-impulse maneuver scheme . . . . .	65
5.2.d	Comparison of approaches . . . . .	67
5.3	Formation Keeping . . . . .	67
5.3.a	Results and Discussion . . . . .	68
<b>6</b>	<b>Problem Set 6</b>	<b>70</b>
6.1	Problem 1: Continuous Control Law . . . . .	70
6.1.a	Formation Reconfiguration Initial Conditions . . . . .	70
6.1.b	Unconstrained Lyapunov Control Implementation . . . . .	70
6.1.c	Continuous Control Lower Bound . . . . .	72
6.1.d	Unconstrained Controller Results & Discussion . . . . .	72
6.2	Controllability of Relative Mean Longitude . . . . .	73
6.2.a	Theory . . . . .	73
6.2.b	Controller Results & Discussion . . . . .	74
6.3	Time-Constrained Lyapunov Control . . . . .	75
6.3.a	Theory . . . . .	75
6.3.b	Initial Results & Discussion . . . . .	76
6.4	Comparison and Limitations of Lyapunov Control Implementation . . . . .	76
<b>7</b>	<b>Problem Set 7</b>	<b>78</b>
7.1	Relative Orbit Control . . . . .	78
7.2	Navigation System Design . . . . .	78
7.2.a	State Representation . . . . .	78
7.2.b	State Prediction Dynamics Model . . . . .	79
7.2.c	Covariance Propagation . . . . .	80
7.2.d	Navigation Sensors . . . . .	80
7.2.e	Measurement Model . . . . .	80

7.2.f	Sensitivity Matrix . . . . .	80
7.2.g	Testing and Model Verification . . . . .	81
<b>8</b>	<b>Problem Set 8</b>	<b>82</b>
8.1	Navigation Filter . . . . .	82
8.1.a	Extended Kalman Filter . . . . .	82
8.1.b	Choice of state representation . . . . .	82
8.1.c	Implementation details . . . . .	82
8.1.d	Simulation and results . . . . .	83
<b>9</b>	<b>Problem Set 9</b>	<b>87</b>
9.1	Model Improvements . . . . .	87
9.2	Integration of Navigation and Control . . . . .	87
9.2.a	Additive noise . . . . .	87
9.2.b	Filtering the measurements . . . . .	89
9.3	Conclusions and Way Forward . . . . .	94
9.3.a	Summary . . . . .	94
9.3.b	Critical Assessment of Results . . . . .	94
9.3.c	Lessons Learned . . . . .	94
9.3.d	Potential Continuations . . . . .	95
<b>10</b>	<b>References</b>	<b>96</b>
<b>11</b>	<b>Appendix A: Code</b>	<b>98</b>

## List of Figures

1.1	TSX/TDX (a) global forest map and (b) terrain model of the Greenland Glacier Network [3]. . . . .	12
1.2	TerraSAR-X spacecraft features. [3] . . . . .	12
1.3	Helix satellite formation illustrating relative orbits (left) and cross-track baselines as a function of orbit position (right). [2] . . . . .	13
1.4	Three data acquisition modes: monostatic (left), bistatic (middle), and alternating bistatic (right). [2] . . . . .	14
1.5	Simulated TSX orbit paths starting on 15 June 2007 over 1000 orbits (66 days). . . . .	16
1.6	Absolute position and velocity errors between the analytical and numerical solution in the RTN frame over 100 orbits (6.6 days). . . . .	17
1.7	Orbital elements, specific angular momentum, and specific energy over 5 orbits for osculating J2 (blue) and unperturbed (orange) propagation. . . . .	19
1.8	Components of the line of apsides and specific angular momentum over 5 orbits for osculating J2 (blue) and unperturbed (orange) propagation. . . . .	19
1.9	Orbital elements, specific angular momentum, and specific energy over 5 orbits for osculating J2 (blue), unperturbed (orange), and mean classical (yellow) orbit propagation. . . . .	21
1.10	Line of apsides and specific angular momentum over 5 orbits for J2 (blue), unperturbed (red), and mean classical (yellow) orbit propagation. . . . .	21
1.11	Isolating seemingly unperturbed parameters of the mean classical orbit J2 propagation reveals small precession. . . . .	22
2.1	Numerically integrated relative RTN position of the deputy (TDX) with respect to the chief (TSX) using the non-linear equations of relative motion. . . . .	24
2.2	Numerically integrated relative RTN velocity using the non-linear equations of relative motion. . . . .	25
2.3	Overlaid numerically integrated (blue) and analytically determined (red) relative RTN position. . . . .	26
2.4	Overlaid numerically integrated (blue) and analytically determined (red) relative RTN velocity. . . . .	26
2.5	Position error in the RTN frame between the numerical and analytical solutions. . . . .	27
2.6	Velocity error in the RTN frame between the numerical and analytical solutions. . . . .	28
2.7	Position error between the numerical and analytical solutions with a 100m difference in initial semi-major axis. . . . .	28
2.8	Numerically integrated relative RTN position with a 100m difference in initial semi-major axis. . . . .	29
2.9	Numerically integrated relative RTN position before (blue) and after (red) the maneuver. . . . .	30

2.10 Numerically integrated relative RTN velocity before (blue) and after (red) the maneuver.	31
3.1 Numerically integrated relative RTN position from HCW equations over 50 orbits. . . . .	33
3.2 Numerically integrated relative RTN velocity from HCW equations over 50 orbits. . . . .	34
3.3 Along-track drift apparent in HCW solution over 50 orbits. . . . .	35
3.4 Relative RTN position from YA solution over 15 orbits. . . . .	37
3.5 Relative RTN velocity from YA solution over 15 orbits. . . . .	37
3.6 Relative radial and along-track position from YA solution. . . . .	38
3.7 Relative RTN position from YA solution (blue) and geometric linear mapping (orange). .	40
3.8 Relative RTN velocity from YA solution (blue) and geometric linear mapping (orange). .	41
3.9 Relative RTN position from YA solution (blue), geometric linear mapping (orange), and numerical integration (yellow). . . . .	43
3.10 Relative RTN velocity from YA solution (blue), geometric linear mapping (orange), and numerical integration (yellow). . . . .	43
3.11 Relative RTN position and velocity error from YA solution (blue) and geometric linear mapping (orange). . . . .	44
3.12 Relative RTN position from YA solution (blue), geometric linear mapping (orange), and numerical integration (yellow) for non-energy matched chief and deputy. . . . .	45
3.13 Relative RTN position from YA solution (blue), geometric linear mapping (orange), and numerical integration (yellow) for large initial relative separation. . . . .	46
3.14 Analytically solved relative RTN position from YA solution (blue), geometric linear mapping (red), and numerical integration (yellow) for non-energy matched chief and deputy. .	47
4.1 Unperturbed osculating (blue) and mean (orange) absolute orbital elements of the chief over 15 orbits. . . . .	49
4.2 Unperturbed osculating (blue) and mean (orange) absolute orbital elements of the deputy over 15 orbits. . . . .	49
4.3 Unperturbed osculating (blue) and mean (orange) relative orbital elements. . . . .	50
4.4 Perturbed osculating (blue) and mean (orange) absolute orbital elements of the chief over 15 orbits. . . . .	50
4.5 Perturbed osculating (blue) and mean (orange) absolute orbital elements of the deputy over 15 orbits. . . . .	51
4.6 Perturbed osculating (blue) and mean (orange) relative orbital elements. . . . .	51
4.7 Relative position in RTN for unperturbed (blue) and J2 perturbed (orange) relative orbital elements. . . . .	52
4.8 State space plots of unperturbed osculating (blue) and mean (orange) relative orbital elements. . . . .	53

4.9	State-space for perturbed osculating (blue) and mean (orange) relative orbital elements. . . . .	53
4.10	Relative orbital elements state space with J2 drift in inclination removed. . . . .	55
4.11	State space for the original initial conditions as propagated by the STM. . . . .	56
4.12	State space for the no-drift initial conditions as propagated by the STM. . . . .	56
5.1	State space representation for C1 preliminary DEM formation over 100 orbits. . . . .	60
5.2	Relative position in the RTN frame for C1 preliminary DEM formation. . . . .	60
5.3	State space representation for preliminary DEM formation over 100 orbits numerically integrated with FODE. . . . .	61
5.4	Least-squares solution ROE state space and control error for the reconfiguration. . . . .	64
5.5	In-plane control actions and $\Delta v$ over the reconfiguration for the least-squares solution. . . . .	64
5.6	Double-impulse solution ROE state space and control error for the reconfiguration. . . . .	66
5.7	In-plane control actions and $\Delta v$ over the reconfiguration for the double-impulse solution. . . . .	66
5.8	Double-impulse solution ROE state space and control error for formation keeping. . . . .	68
5.9	In-plane control actions and $\Delta v$ over the formation keeping for the double-impulse solution. . . . .	69
6.1	In-plane control actions and $\Delta v$ over the reconfiguration for the unconstrained Lyapunov controller. . . . .	72
6.2	ROE state space and control error for the reconfiguration using unconstrained Lyapunov continuous control. . . . .	73
6.3	Control actions and $\Delta v$ for the reconfiguration using unconstrained Lyapunov continuous control while tracking the relative mean longitude. . . . .	74
6.4	ROE state space and control error for the reconfiguration using unconstrained Lyapunov continuous control while tracking the relative mean longitude. . . . .	75
7.1	State space comparison of numerical and STM propagation over 100 orbits. . . . .	81
8.1	Ground truth and estimated ROE state over 5 orbits. . . . .	83
8.2	State estimation error with 3 standard deviations centered about 0. . . . .	84
8.3	Convergence of the state estimation error within 0.3 orbits shown with 3 standard deviations. . . . .	84
8.4	Pre-fit and post-fit residuals across 5 orbits. . . . .	86
9.1	In-plane control actions and $\Delta v$ over the formation keeping with noisy measurements. . . . .	88
9.2	ROE state space and control error for formation keeping with noisy measurements. . . . .	88
9.3	In-plane control actions and $\Delta v$ over the formation keeping with filtered measurements. . . . .	89
9.4	ROE state space and control error for formation keeping with filtered measurements. . . . .	90
9.5	State estimation error with 3 standard deviations centered around 0. . . . .	91

9.6	Convergence of the state estimation error within 1/3 of an orbit shown with 3 standard deviations. . . . .	92
9.7	Pre-fit and post-fit residuals across the final 10 orbits. . . . .	92
9.8	Navigation error mapped into the orbital frame aligned with radial (top), along-track (middle), and cross-track (bottom) directions. . . . .	93

## List of Tables

1.1	Comparison of DTED-2 and HRTE-3 specifications [2] . . . . .	11
1.2	Initial classical orbit elements of the chief satellite TSX. . . . .	15
2.1	Initial classical orbital parameters of TSX and TDX in Helix formation. . . . .	23
3.1	Differences in initial classical orbit elements between the deputy and the chief. . . . .	32
3.2	Initial orbital elements of the chief for eccentric orbit simulation. . . . .	35
4.1	Initial osculating orbital parameters of deputy satellite TDX. . . . .	48
5.1	Formation parameters for key mission phases [8] . . . . .	57
5.2	Initial orbital elements for preliminary mission phases. All units in meters. . . . .	58
5.3	Least-squares maneuver scheduling. . . . .	63
5.4	Reconfiguration accuracy of least-squares solution. . . . .	64
5.5	Closed-form solution maneuver scheduling. . . . .	65
5.6	Reconfiguration accuracy of double-impulse solution. . . . .	66
6.1	Initial osculating orbital parameters of chief satellite TSX for mission phase C1. . . . .	70
6.2	Comparison of $\Delta v$ expended and ROE error between the continuous controllers. . . . .	76
8.1	EKF time and measurement update rules. . . . .	82
8.2	Mean and standard deviation statistics of the pre-fit and post-fit residuals. . . . .	85
9.1	Control tracking error statistics in the ROE state. . . . .	91
9.2	Control steady-state RTN error. . . . .	91
9.3	Mean and standard deviation statistics of the pre-fit and post-fit residuals over the entire simulation. . . . .	93
9.4	Navigation ROE error excluding the convergence phase of the EKF. . . . .	93

## 0 Scope

This report describes the mission specifications and development of formation flying algorithms for the final project of AA279D Dynamics, Navigation and Control of Distributed Space Systems.

## 1 Problem Set 1

### 1.1 Mission Overview

#### 1.1.a Reference Mission

This project is based on TanDEM-X, a dual formation-flying satellite mission that performs Earth observation using interferometric Synthetic Aperture Radar (SAR) to create a high-precision 3-dimensional model of the Earth. The TanDEM-X satellite was launched three years after the launch of its twin TerraSAR-X, joining it in low-Earth orbit. Both satellites are currently operated by the German Aerospace Center (DLR). Data is managed and distributed by the European Space Agency (ESA), and the satellites were built by Airbus Defense and Space [1].

#### 1.1.b Mission Objectives

The primary goal of the mission is to create high-resolution Digital Elevation Models (DEM) of the Earth's surface to the High-Resolution Terrain Elevation Level 3 (HRTE-3) specification as defined by the National Geospatial Agency. Images produced by the SAR instruments such as those in Figure 1.1 aid monitoring of land and coastal processes including forests, vegetation, glacial melt, and ocean currents. Prior to TanDEM-X, DEMs have traditionally lacked the full global coverage and precision required for modern navigation, military operations, and scientific applications [2]. As shown in Table 1.1, the novel HRTI-3 DEM standard generated by TanDEM-X compared to the previous state-of-the-art (DTED-2) is significantly more accurate across the board, and provides spatial resolution that is sharper by more than a factor of 2. With the capability of collecting global data across the poles, this mission is critical for a range of science, government, military, and commercial applications.

Table 1.1: Comparison of DTED-2 and HRTE-3 specifications [2]

Requirement	Specification	DTED-2	HRTI-3
Relative Vertical Accuracy	90% linear point-to-point error over a $1^\circ \times 1^\circ$ cell	12 m (slope < 20%) 15 m (slope > 20%)	2 m (slope < 20%) 4 m (slope > 20%)
Absolute Vertical Accuracy	90% linear error	18 m	10 m
Relative Horizontal Accuracy	90% circular error	15 m	3 m
Horizontal Accuracy	90% circular error	23 m	10 m
Spatial Resolution	independent pixels	30 m (1 arc sec @ equator)	12 m (0.4 arc sec @ equator)

The secondary objective of TanDEM-X is to demonstrate novel SAR techniques in flight including digital beamforming, along-track interferometry with a varying baseline, and super-resolution. To perform these

techniques, this mission further demonstrates a new orbit concept allowing for safe formation flying at close proximity between the two spacecraft [1].

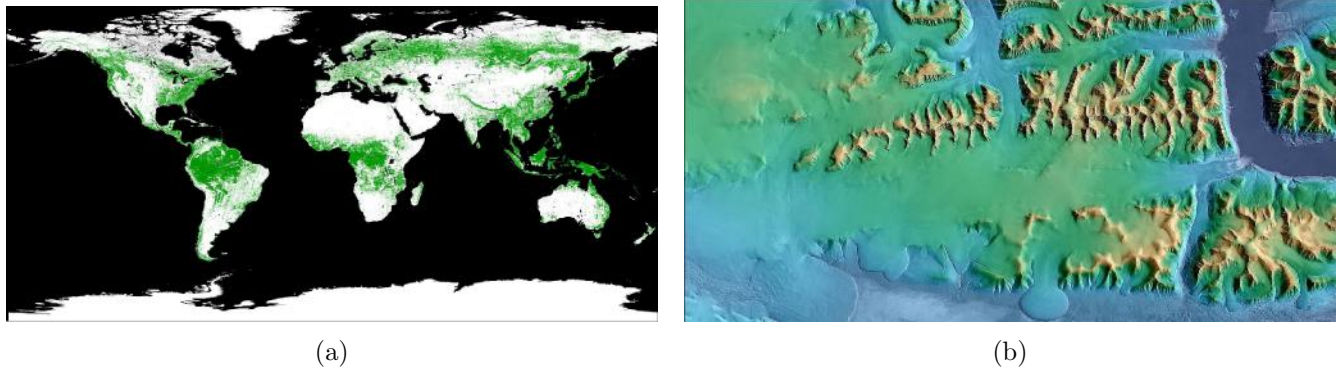


Figure 1.1: TSX/TDX (a) global forest map and (b) terrain model of the Greenland Glacier Network [3].

### 1.1.c Spacecraft Specification

The mission relies on formation flying involving the TanDEM-X (TDX) and TerraSAR-X (TSX) satellites. The two spacecraft are nearly identical, equipped with identical X-band SAR instruments to collect high-resolution Earth images as shown by Figure 1.2. The main difference is that TanDEM-X features an inter-satellite S-band receiver which it uses to receive status and GPS information from TerraSAR-X. It is also upgraded with an advanced cold-gas propulsion system for fine formation-keeping maneuvers [1] [2].

TerraSAR-X has a wet mass of 1230 kg (of which 78 kg are propellant) and the bus dimensions are 5m × 2.4 m. TanDEM-X shares the same dimensions but is heavier at 1340 kg wet mass (of which 120 kg are propellant). The SAR antennae have dimensions of 5 m × 0.8 m and the average spacecraft power is 800 W [1] [3].

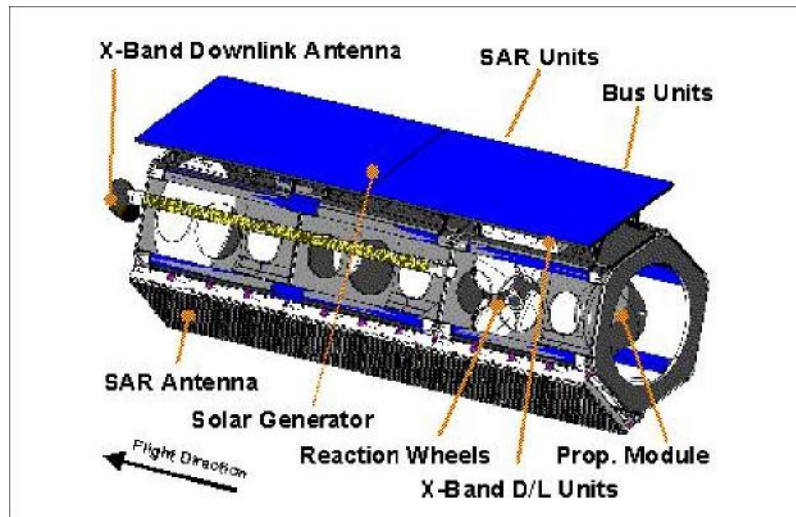


Figure 1.2: TerraSAR-X spacecraft features. [3]

### 1.1.d Launch and Orbit

TSX flies in a sun-synchronous dawn-dusk circular orbit at which it was launched. The orbit is described by a mean altitude of 514.8 km (between 505-533 km), an inclination of  $97.44^\circ$ , and a local equator crossing time of 18:00 on the ascending node with a nominal revisit period of 11 days (and 167 orbits in the repeat) [1] [3]. The satellite was launched on June 15, 2007 from Baikonur Cosmodrome, Kazakhstan. The mission was designed for 5 years with a goal of a 6.5-year design life, but as of January 2022, TSX is still performing scientific operations in space [1].

TDX was launched in June 21, 2010 also from Baikonur. Given the close formation required by the SAR mission, TDX has a practically identical orbit to TSX. To set up an effective baseline, TDX is separated in the right ascension of the ascending node (RAAN) with a small offset in eccentricity. A horizontal baseline between the two spacecraft is maintained between 200 and 3000 m, depending on mission requirements for DEM generation at different latitudes.

The novel relative orbit of the two spacecraft is called a Helix formation, which allows for relatively small distances between the satellites throughout the absolute orbits while minimizing risk of collision at the poles as depicted in Figure 1.3. This is achieved by combining out-of-plane displacement through various relative RAAN values (e.g.  $\Delta\Omega = \{300\text{m}, 400\text{m}, 500\text{m}\}$ ) and radial separation through various relative eccentricity (e.g  $\Delta e = \{300\text{m}, 500\text{m}\}$ ). In the Helix formation, there are no crossings between the two orbits, so arbitrary along-track shifts in the orbits can be performed to finely adjust the baseline [1]. The implication of this formation is that maximum radial separation is achieved at the poles and maximum normal separation at the equator.

TDX was designed with a mission life of 5 years, and as of January 2022 it is still providing SAR imagery after 12 years in orbit [1]. Fuel levels on both TDX and TSX are currently enough to continue their mission until 2026 [1].

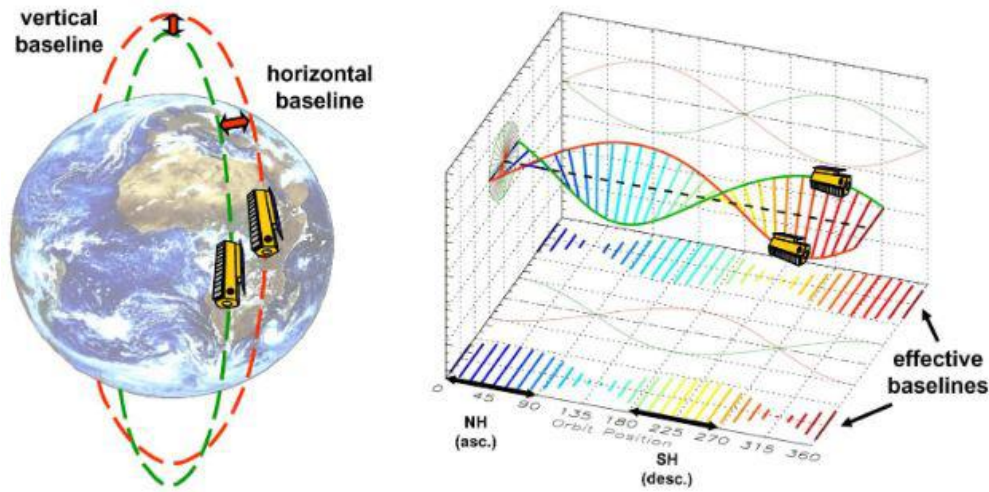


Figure 1.3: Helix satellite formation illustrating relative orbits (left) and cross-track baselines as a function of orbit position (right). [2]

### 1.1.e Synthetic Aperture Radar Payload

The scientific basis of this mission using SAR enables active remote sensing during the day, at night, and even through cloud coverage. The technology works by broadcasting a radar signal to the Earth and picking up the reflections. Comparing the reflected signal with the broadcast reveals the nature of the reflector, whether land, water, snow, ice, or otherwise [4]. In the case of TSX and TDX, interferometric SAR can be conducted in four configurations: bistatic, monostatic, alternating bistatic, and simultaneous transmit as described in [2]. A visualization of three of these modes is shown in Figure 1.4.

- *Bistatic*: This mode is used to generate the DEM. One of the satellites acts as a transmitter over a common radar footprint. Both satellites collect the reflected signals and comparison of the difference generates the DEM.
- *Monostatic*: This mode has the satellites acting independently, allowing operators to skip the difficult synchronization process. With a relatively long baseline ( $\sim 10$  km), this mode is meant as a backup in case synchronization is not feasible and generates a lower accuracy DEM.
- *Alternating bistatic*: This is similar to the bistatic mode, except that the transmitter is switched at every pulse. This mode is used to calibrate the bistatic SAR interferometer.
- *Simultaneous transmit*: In this mode, both spacecraft transmit at the same time, but the spacecraft maintain a close baseline. This mode allows for accurate synchronization and further calibration of the SAR instrument at the cost of lower range resolution for each individual image.

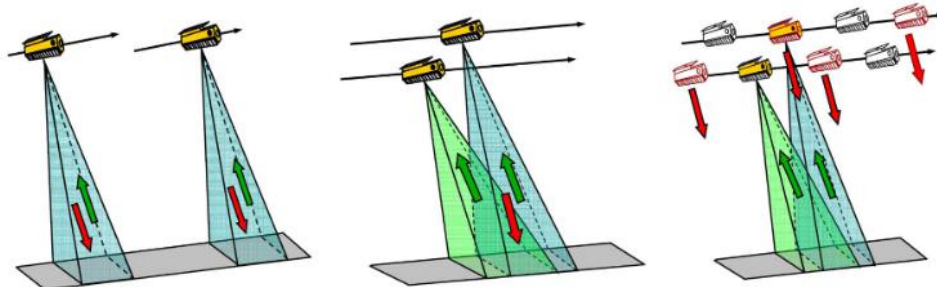


Figure 1.4: Three data acquisition modes: monostatic (left), bistatic (middle), and alternating bistatic (right). [2]

### 1.1.f Key Dynamics, Guidance, Navigation & Control Requirements

For SAR data collection, close-proximity formation-flying while maintaining relative separation is mission-critical. To conduct bistatic interferometry, the satellites must be maintained within a toroidal tube 250m in radius about a reference trajectory for the duration of the mission [1]. Separation in eccentricity and ascending node is also critical to keep the two satellites in Helix formation and to maximize safety. Radial and normal separation shall not be simultaneously zero to avoid collision.

Furthermore, certain SAR techniques require tight formation-keeping and localization. Station-keeping thrusters on TDX regularly fire to counteract drift associated with J2 perturbation arising from the oblateness of the Earth. At specific locations of interest, osculating along-track separations must be sufficiently precise to perform along-track interferometry.

Both spacecraft employ GPS for navigation, with TSX demonstrating an absolute navigational accuracy of 5 cm [1]. The relative baseline between the two, typically between 500 and 1500km, has a 1-mm accuracy requirement in order to achieve high-precision DEM [1]. Relative control accuracy requirements are 28m in cross-track and 200m in along-track directions, which TDX has significantly surpassed in flight with nominal accuracies of 5m in cross-track and 30m in along-track [1].

## 1.2 Orbit Simulation, Review of Astrodynamics

### 1.2.a Initial Orbital Elements

Given the close formation of the two spacecraft, the initial conditions are chosen to be the same orbit for the purposes of this exercise. The initial conditions are of TSX launched on June 15, 2007 into a sun-synchronous orbit with a mean altitude of 514.8 km and inclination of  $97.44^\circ$ . This orbit has a local equator crossing time of 18:00 on the ascending node and was launched on the summer solstice, corresponding to a right ascension of the ascending node of  $\Omega = 270^\circ$ . The nominal revisit period is 11 days (and 167 orbits in the repeat). The orbit is circular, corresponding to an eccentricity  $e = 0$ . This ideal eccentricity is slightly offset to be more realistic. The initial conditions are described in Table 1.2 using the classical Keplerian orbital elements semi-major axis  $a$ , inclination  $i$ , eccentricity  $e$ , argument of periapsis  $\omega$ , RAAN  $\Omega$ , and mean anomaly  $M$ .

$a$	$e$	$i$	$\Omega$	$\omega$	$M$
6892.927 km	$1 \times 10^{-4}$	$97.44^\circ$	$270^\circ$	$0^\circ$	$0^\circ$

Table 1.2: Initial classical orbit elements of the chief satellite TSX.

### 1.2.b Initial Position and Velocity

As this is an Earth-centered satellite mission, the inertial reference frame of choice will be Earth Centered Inertial (ECI). The initial Keplerian orbital elements are converted to position and velocity in the ECI frame by first expressing them in the perifocal frame and then performing three coordinate rotations (3-1-3 Euler sequence) about each axis by the right ascension of the ascending node, inclination, and argument of periapsis. In the perifocal frame, position and velocity are given by:

$${}^P\vec{r} = \frac{a(1 - e^2)}{1 + e \cos f} \begin{bmatrix} \cos f \\ \sin f \\ 0 \end{bmatrix} \quad (1)$$

$${}^P\vec{v} = \sqrt{\frac{\mu}{a(1 - e^2)}} \begin{bmatrix} -\sin f \\ e + \cos f \\ 0 \end{bmatrix} \quad (2)$$

When using these equations, mean anomaly which is a function of time must first be transformed to the true anomaly  $f$ . The transformation matrix from the perifocal to the ECI frame is given by the following, where  $R_k(\theta)$  represents the direction cosine matrix rotating about the  $k$ -axis by an angle  $\theta$ :

$$R_{PQW}^{ECI} = R_z(-\Omega)R_x(-i)R_z(-\omega) \quad (3)$$

From these equations, the initial position and velocity in the ECI frame is found to be:

$$\begin{aligned} {}^I\vec{r}_{0,ECI} &= [0 \quad -6892.2 \quad 0] \text{ km} \\ {}^I\vec{v}_{0,ECI} &= [-0.9848 \quad 0 \quad 7.541] \text{ km/s} \end{aligned}$$

### 1.2.c Numerical Simulations of Unperturbed and J2 Propagation

The orbit visualization in Figure 1.5 shows a nearly circular chief orbit under unperturbed and perturbed propagation. Introducing J2 perturbations causes a nodal precession of the orbit due to the non-spherical mass distribution of the Earth. The J2 acceleration is expressed in ECI by [5]:

$${}^{ECI}a_{J2} = \frac{3J_2\mu R_E^2}{2||\vec{r}||^5} \left[ \left( 5\frac{r_k^2}{||\vec{r}||^2} - 1 \right) (r_i \hat{I} + r_j \hat{J}) + \left( 5\frac{r_k^2}{||\vec{r}||^2} - 3 \right) r_k \hat{K} \right] \quad (4)$$

This was applied as a disturbing force  $\vec{d}$  to the 2-body differential equations of motion, which was subsequently solved by numerical integration using MATLAB *ode45*.

$$\vec{r} + \frac{\mu \vec{r}}{r^3} = \vec{d} \quad (5)$$

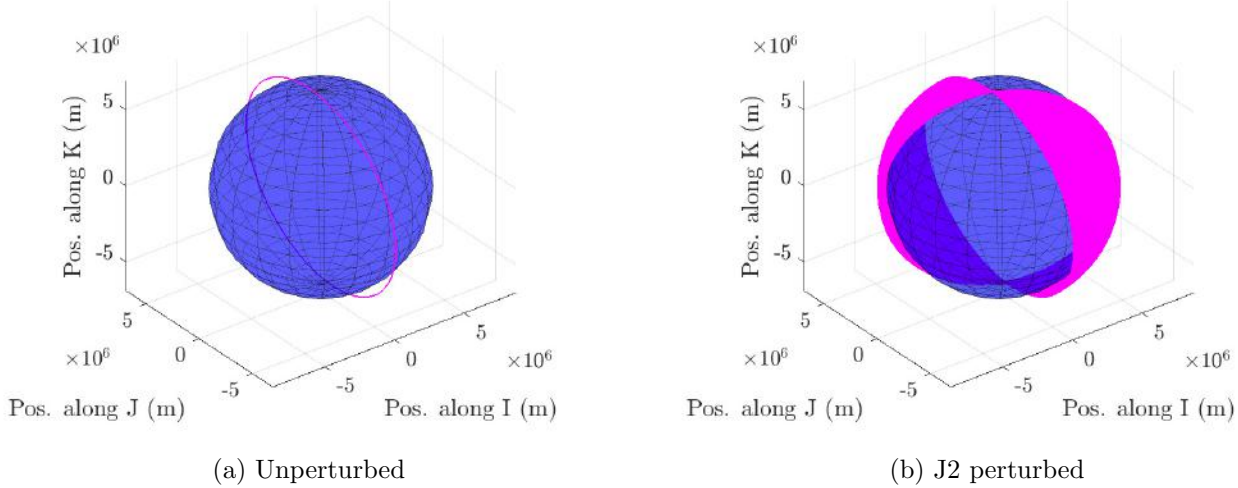


Figure 1.5: Simulated TSX orbit paths starting on 15 June 2007 over 1000 orbits (66 days).

### 1.2.d Numerical and Analytical Comparison of the Unperturbed Orbit

In the restricted two-body problem, the sole parameter varying with time is the mean anomaly  $M$ . Using the same time steps as the numerical integration, Keplerian propagation was determined analytically by incrementing the mean anomaly, transforming mean anomaly into true anomaly, and applying the conic section equations (Eqs. 1 and 2) to resolve the position and velocity in the perifocal frame. With our previously validated code to transform orbital elements to the ECI frame, position and velocity were transformed from perifocal to ECI.

The position vector can be expressed in the Radial, Along-Track, and Cross-Track (RTN) frame by combining the rotation matrix  $R_{PQW}^{ECI}$  from Eq. 3 with a subsequent rotation by the argument of latitude:

$$R_{ECI}^{RTN} = R_{PQW}^{ECI} R_z(-f) \quad (6)$$

$$\vec{r}_{RTN} = R_{ECI}^{RTN} \vec{r}_{ECI} \quad (7)$$

Because the RTN frame is a non-inertial reference frame, the Theorem of Coriolis must be applied to express the velocity in RTN in addition to the coordinate transformation:

$$ECI \vec{v}_{ECI} = R_{RTN}^{ECI} \left[ RTN \vec{v}_{RTN} + \vec{\omega}_{ECI}^{RTN} \times \vec{r}_{RTN} \right] \quad (8)$$

$$RTN \vec{v}_{RTN} = (R_{RTN}^{ECI})^T ECI \vec{v}_{ECI} - \vec{\omega}_{ECI}^{RTN} \times \vec{r}_{RTN} \quad (9)$$

where the angular velocity of the ECI frame with respect to the RTN frame as expressed in the ECI frame is simply the rate of change of the argument of latitude:

$$\vec{\omega}_{ECI}^{RTN} = [0, 0, \dot{f}]^T$$

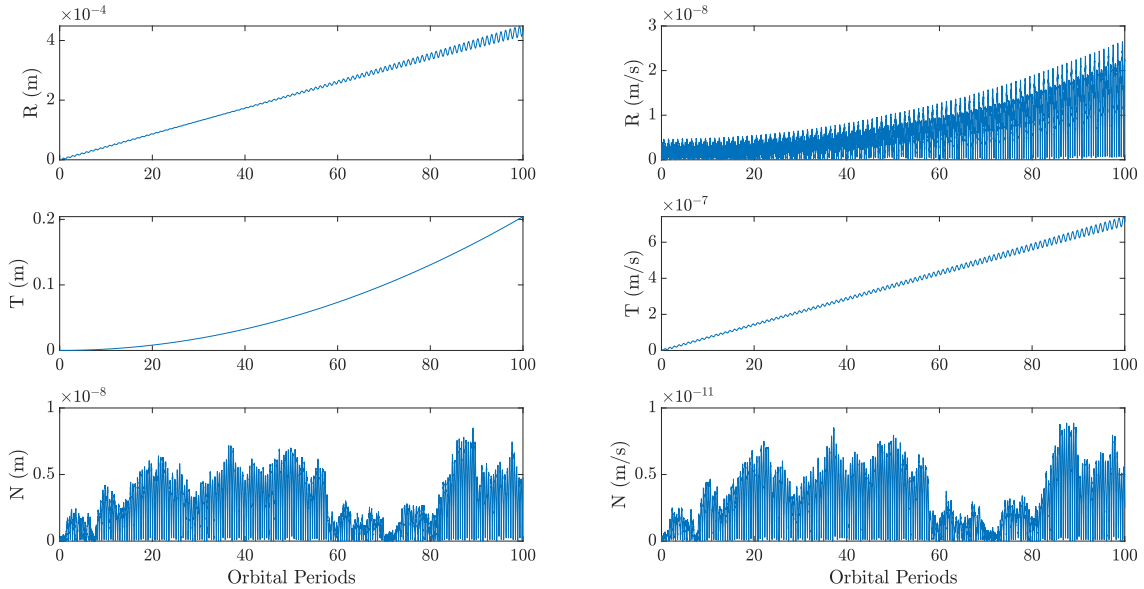


Figure 1.6: Absolute position and velocity errors between the analytical and numerical solution in the RTN frame over 100 orbits (6.6 days).

Absolute error difference between the numerical and analytical solutions is shown in Figure 1.6. Over 100 orbits, position error grows to a maximum on the order of 20 centimeters in the along-track direction and the velocity error grows to the order of micrometers per second. The cross-track position and velocity errors are somewhat better behaved while error in the radial and along-track directions continue to increase.

with time. These results were obtained using a tolerance of  $10^{-12}$  with the MATLAB *ode45* solver and a step size of 57 seconds, or one-hundredth of the orbital period. As expected, increasing either of these two parameters led to higher error.

### 1.2.e Numerical Simulation of Osculating Orbital Elements

The following procedure follows the steps described in Vallado [6]. The implementation begins by constructing three vectors which define typical orbits (specific angular momentum  $\vec{h}$ , line of nodes  $\hat{n}$ , and line of apsides  $\hat{e}$ ):

$${}^{ECI}\vec{h} = {}^{ECI}\vec{r} \times {}^{ECI}\vec{v} \quad (10)$$

$${}^{ECI}\hat{n} = \hat{K} \times {}^{ECI}\vec{h} \quad (11)$$

$${}^{ECI}\hat{e} = \frac{1}{\mu} \left[ \left( \left\| {}^{ECI}\vec{v} \right\|^2 - \frac{\mu}{\left\| {}^{ECI}\vec{r} \right\|} \right) {}^{ECI}\vec{r} - \left( {}^{ECI}\vec{r} \cdot {}^{ECI}\vec{v} \right) {}^{ECI}\vec{v} \right] \quad (12)$$

The orbit shape, assuming a non-parabolic shape, may be computed using the specific mechanical energy  $\epsilon$  and semi-major axis  $a$ :

$$\epsilon = \frac{\left\| {}^{ECI}\vec{v} \right\|^2}{2} - \frac{\mu}{\left\| {}^{ECI}\vec{r} \right\|} \quad (13)$$

$$a = -\frac{\mu}{2\epsilon} \quad (14)$$

The orientation of the orbit is obtained by:

$$i = \cos^{-1} \left( \frac{h_K}{\left\| {}^{ECI}\vec{h} \right\|} \right) \quad (15)$$

$$\Omega = \cos^{-1} \left( \frac{n_I}{\left\| {}^{ECI}\hat{n} \right\|} \right) \quad (16)$$

$$u = \cos^{-1} \left( \frac{{}^{ECI}\hat{n} \cdot {}^{ECI}\vec{r}}{\left\| {}^{ECI}\hat{n} \right\| \left\| {}^{ECI}\vec{r} \right\|} \right) \quad (17)$$

In addition, checks in the code are performed to ensure that these angles are evaluated in the correct quadrants within the range  $[0, 2\pi]$ .

The orbital elements, specific angular momentum, and specific energy are plotted for simulations including and excluding J2 effects in Figure 1.7. For unperturbed orbit propagation, all orbital elements are held constant except for the argument of latitude ( $u$ ) as the satellite propagates its orbit. Additionally, the line of apsides defined by the vector  $e$  is constant while the specific angular momentum changes slightly in the  $\hat{K}$  component as shown in Figure 1.8. Over a period of 5 orbits, this variance was calculated to be on the order of  $3 \text{ mm}^2/\text{s}$ , which is significantly smaller than the magnitude of specific angular momentum ( $10^{10} \text{ m}^2/\text{s}$ ). This discrepancy may be attributed to numerical integration errors.

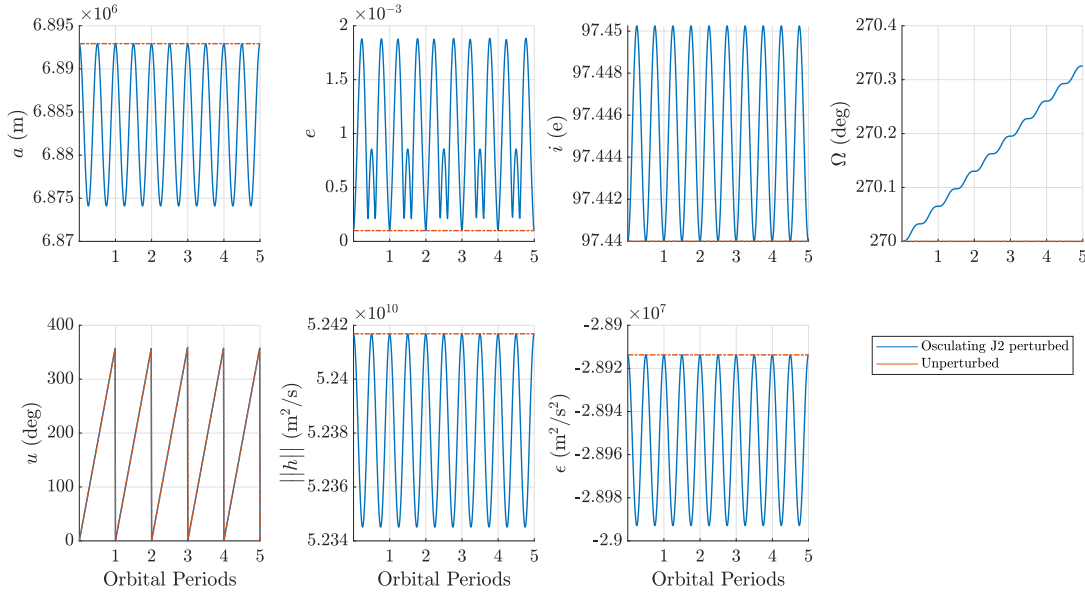


Figure 1.7: Orbital elements, specific angular momentum, and specific energy over 5 orbits for osculating J2 (blue) and unperturbed (orange) propagation.

Including J2 effects (both short and long period oscillations), we find that the orbital elements, specific mechanical energy, line of apsides and specific angular momentum all exhibit periodicity. The right ascension of the ascending node  $\Omega$  is clearly under secular effects as is expected for an inclined orbit due to precession. Likewise, we observe that the specific angular momentum demonstrates secular effects along the  $\hat{J}$  and  $\hat{K}$  directions, which is also to be expected due to the changes in RAAN.

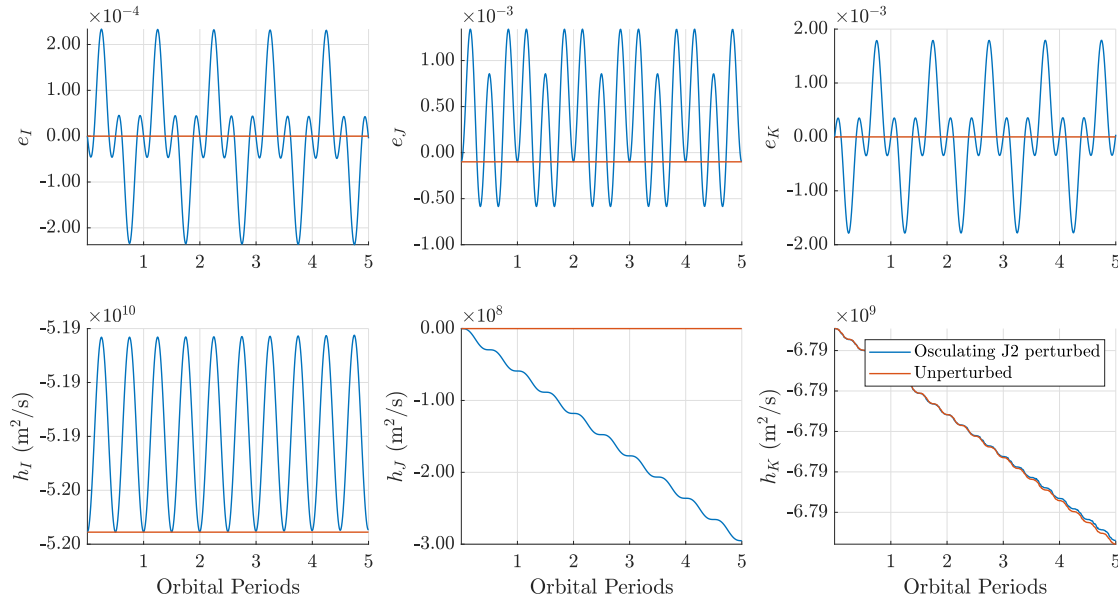


Figure 1.8: Components of the line of apsides and specific angular momentum over 5 orbits for osculating J2 (blue) and unperturbed (orange) propagation.

### 1.2.f Mean Classical Orbital Elements

The differential equations for the mean classical orbital elements reflect zero variations in  $a$ ,  $e$ , and  $i$  over time. The following linear differential equations are used in order to update the new state composed of orbital elements [7]:

$$\frac{d\Omega}{dt} = -\frac{3}{2}nJ_2 \left( \frac{R_E}{p} \right)^2 \cos(i) \quad (18)$$

$$\frac{du}{dt} = \frac{3}{4}nJ_2 \left( \frac{R_E}{a(1-(e_x^2+e_y^2))} \right)^2 \left( \sqrt{1-(e_x^2+e_y^2)}(3\cos^2 i - 1) + (5\cos^2 i - 1) \right) \quad (19)$$

$$\frac{de_x}{dt} = -\frac{3}{4}nJ_2 \left( \frac{R_E}{a(1-(e_x^2+e_y^2))} \right)^2 e_y(5\cos^2 i - 1) \quad (20)$$

$$\frac{de_y}{dt} = \frac{3}{4}nJ_2 \left( \frac{R_E}{a(1-(e_x^2+e_y^2))} \right)^2 e_x(5\cos^2 i - 1) \quad (21)$$

We follow a similar procedure as in the previous section to produce an evolution of the state vector across 5 orbits. Superimposing the resulting mean orbital elements, specific angular momentum, and specific energy with their osculating values in Figure 1.8 and Figure 1.10 shows they are generally in agreement.

Under averaging theory, we know the J2 perturbs the right ascension of the ascending node, the argument of periapsis and the mean anomaly. Since we are using the argument of latitude, the effects of the latter two get folded into this one. We see this clearly in Figure 1.9, where the only secular effects are observed in the right ascension of the ascending node. Although the argument of latitude appears to be unperturbed, taking a closer look at the region in Figure 1.11 shows that the values are slightly precessing. Note that this precession is due to  $J_2$ , and that under the averaging theory we ignore motion that is periodic. This is why, unlike in the propagation of the position and velocity state vector, we do not see rapid changes in the argument of latitude as the satellites traverses its orbit.

Additionally, given the equations above, we would not expect a perfectly circular orbit to have any effects on its eccentricity by  $J_2$ . Figure 1.11 reveals very slight variation in the eccentricity vector. This is likely a numerical error, as the initial eccentricity vector is not exactly computed to be 0.

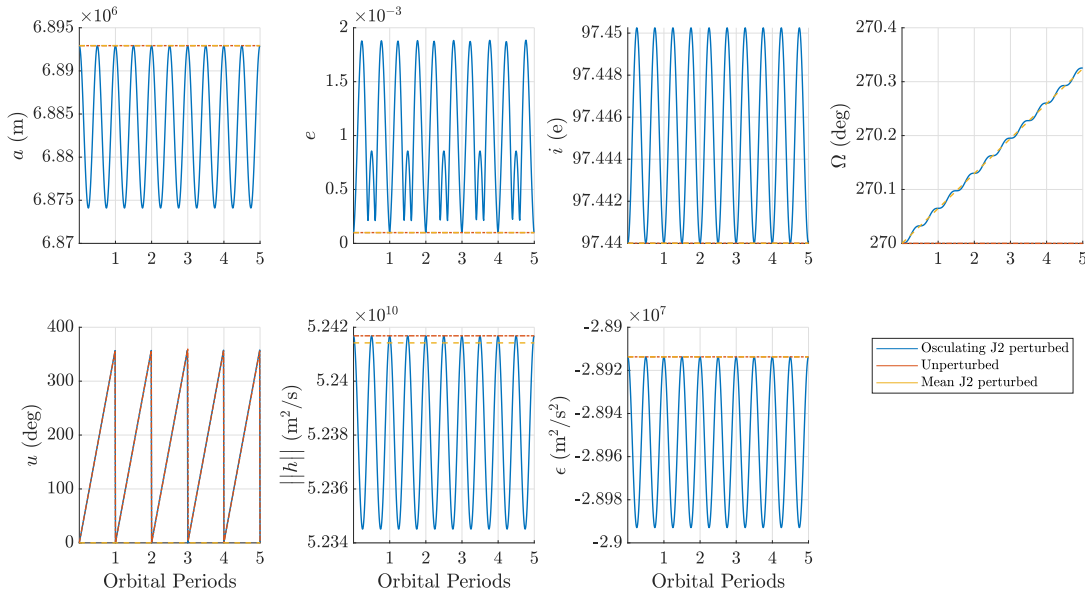


Figure 1.9: Orbital elements, specific angular momentum, and specific energy over 5 orbits for osculating J2 (blue), unperturbed (orange), and mean classical (yellow) orbit propagation.

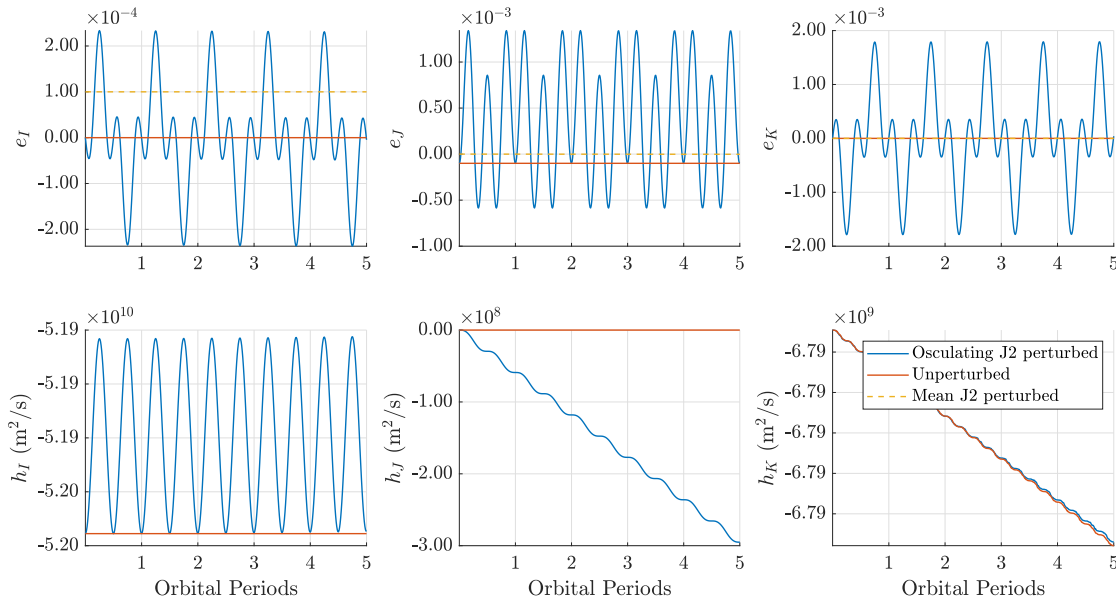


Figure 1.10: Line of apsides and specific angular momentum over 5 orbits for J2 (blue), unperturbed (red), and mean classical (yellow) orbit propagation.

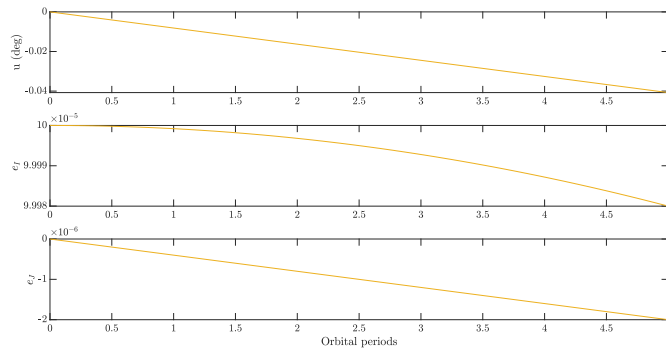


Figure 1.11: Isolating seemingly unperturbed parameters of the mean classical orbit J2 propagation reveals small precession.

### 1.2.g Reconciling Osculating and Mean Orbital Elements

Inconsistencies during initialization can be mitigated using Brouwer theory to transform between mean and osculating values. We see this issue when comparing the unperturbed and the mean orbital elements of RAAN and argument of latitude  $u$ . Applying Brouwer theory would allow us to better match the behaviour of the mean classical orbit case in Figure 1.9 with the behaviour seen in the J2 perturbed case.

## 2 Problem Set 2

### 2.1 Everything is Relative

#### 2.1.a Chief and Deputy Orbit Initialization

TSX is selected as the chief orbit with TDX as its deputy. In this case, TDX employs e/i vector separation in order to have a safe orbit that avoids crossing paths with TSX. We will be modeling the first phase of the mission (preliminary DEM generation), reported with the following difference in eccentricity  $a\delta e$ , difference in inclination  $a\delta i$ , and difference in phase angle [8]:

$$a\delta e = 260 \text{ m}, \quad a\delta i = 222 \text{ m}, \quad \theta - \phi = 200^\circ$$

These offsets are transformed to the orbital elements used in this project using polar coordinates [8]. The subscript 0 refers to the chief orbit and the subscript 1 refers to the deputy orbit.

$$\delta e = \begin{bmatrix} \delta e_x \\ \delta e_y \end{bmatrix} = \delta e \begin{bmatrix} \cos(\phi) \\ \sin(\phi) \end{bmatrix} \quad (22)$$

$$\delta i = \begin{bmatrix} \delta i_x \\ \delta i_y \end{bmatrix} = \delta i \begin{bmatrix} \cos(\theta) \\ \sin(\theta) \end{bmatrix} = \begin{bmatrix} i_1 - i_0 \\ (\Omega_1 - \Omega_0)\sin(i_0) \end{bmatrix} \quad (23)$$

Using these relations, the relative eccentricity and inclination of the chief and deputy may be determined. We design the phase angle  $\theta = +90^\circ$ , the argument of latitude in which the deputy crosses the orbital plane of the chief, in order to produce a safe relative orbit as will be shown. The initial conditions for this leader and follower setup are given in Table 2.1.

	$a$	$e$	$i$	$\Omega$	$\omega$	$M$
TSX	6892.927 km	$1 \times 10^{-4}$	97.44°	270°	0°	0°
TDX	6892.927 km	$9.4035 \times 10^{-5}$	97.44°	270.0019°	-22.1439°	22.1442°

Table 2.1: Initial classical orbital parameters of TSX and TDX in Helix formation.

#### 2.1.b Numerical Integration of Relative Equations of Motion

Relative motion between the chief and deputy spacecraft can be derived as a 10-dimensional system of differential equations describing the relative acceleration of the deputy in the rotating RTN frame as  $[\ddot{x}, \ddot{y}, \ddot{z}]$  and the acceleration of the chief as  $[\ddot{r}_0, \ddot{\theta}]$ . The system is represented by the state vector  $[\vec{r}, \vec{\rho}, r_0, \theta_0, \dot{r}_0, \dot{\theta}_0]$ .

$$\ddot{x} - 2\dot{\theta}_0\dot{y} - \ddot{\theta}_0y - \dot{\theta}_0^2x = -\frac{\mu(r_0 + x)}{[(r_0 + x)^2 + y^2 + z^2]^{\frac{3}{2}}} + \frac{\mu}{r_0^2} \quad (24)$$

$$\ddot{y} + 2\dot{\theta}_0\dot{x} + \ddot{\theta}_0x - \dot{\theta}_0^2y = -\frac{\mu y}{[(r_0 + x)^2 + y^2 + z^2]^{\frac{3}{2}}} \quad (25)$$

$$\ddot{z} = -\frac{\mu z}{[(r_0 + x)^2 + y^2 + z^2]^{\frac{3}{2}}} \quad (26)$$

$$\ddot{r}_0 = r_0 \dot{\theta}_0^2 - \frac{\mu}{r_0^2} \quad (27)$$

$$\ddot{\theta}_0 = -\frac{2\dot{r}_0 \dot{\theta}_0}{r_0} \quad (28)$$

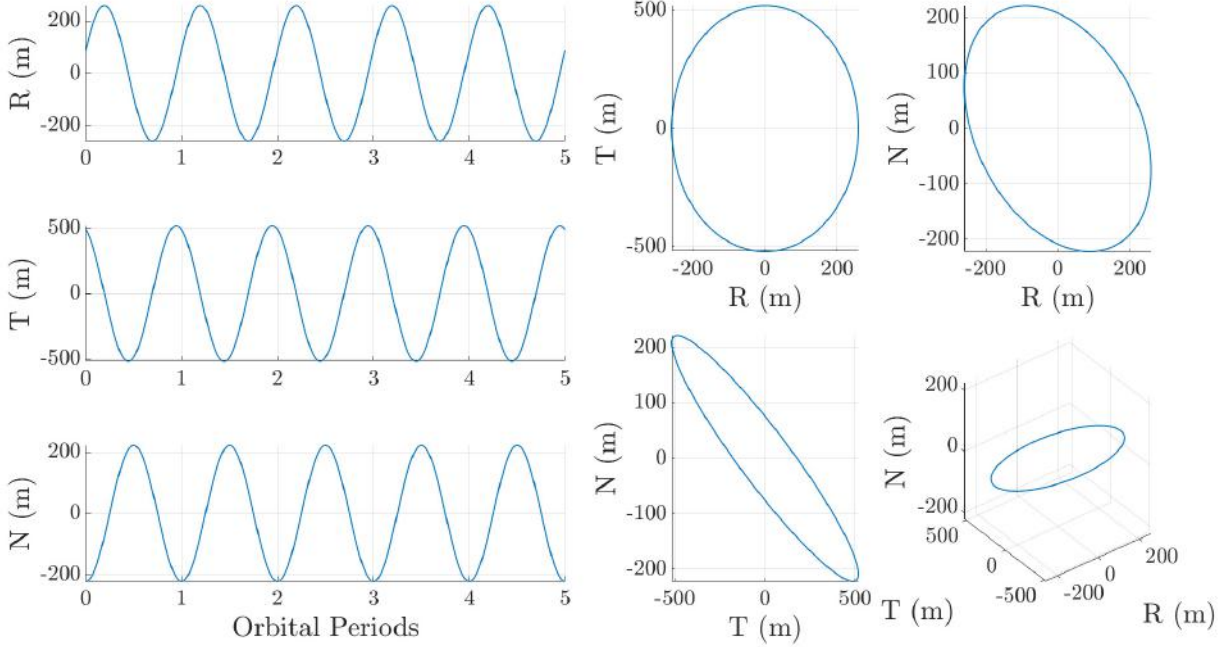


Figure 2.1: Numerically integrated relative RTN position of the deputy (TDX) with respect to the chief (TSX) using the non-linear equations of relative motion.

These differential equations are numerically integrated using *ode45*, and the results are shown in Figure 2.1 and 2.2. The corresponding initial conditions are found by finding the initial ECI position and velocities of the orbits from the orbital elements in part a. We then employ differences, coordinate transforms and the Theorem of Coriolis to find the correct initial conditions. The superscript 0 corresponds to the fact that these are initial conditions, while the subscript indicated the chief (0) or deputy (1). The rotation matrix and the corresponding rotation rates are taken with respect to the chief's orbit.

$$\theta_0 = u_0^0; \quad (29)$$

$$\dot{\theta}_0^0 = \sqrt{\frac{\mu}{a_0^3(1-e_0^2)^3}} \left( 1 + e_0 \cdot \cos(\theta_0) \right)^2 \quad (30)$$

$$ECI \vec{\omega}^{RTN} = [0, 0, \dot{\theta}_0^0] \quad (31)$$

$$R_{ECI}^{RTN} = R_z(-\Omega_0)R_x(-i_0)R_z(-u_0^0) \quad (32)$$

$$ECI \vec{r}^0 = ECI \vec{r}_1^0 - ECI \vec{r}_0^0 \quad (33)$$

$$ECI \dot{\vec{r}}^0 = ECI \vec{v}_1^0 - ECI \vec{v}_0^0 \quad (34)$$

$$RTN \vec{\rho}^0 = R_{ECI}^{RTN ECI} \vec{\rho}^0 \quad (35)$$

$$RTN \dot{\vec{\rho}}^0 = R_{ECI}^{RTN ECI} \dot{\vec{\rho}}^0 - ECI \vec{\omega}^{RTN} \times RTN \vec{\rho}^0 \quad (36)$$

$$RTN \vec{r}_0^0 = R_{ECI}^{RTN ECI} \vec{r}_0^0 \quad (37)$$

$$r_0^0 = \left\| RTN \vec{r}_0^0 \right\|_2 \quad (38)$$

$$\dot{r}_0^0 = \left\| R_{ECI}^{RTN ECI} \vec{v}_0^0 - ECI \vec{\omega}^{RTN} \times RTN \vec{r}_0^0 \right\|_2 \quad (39)$$

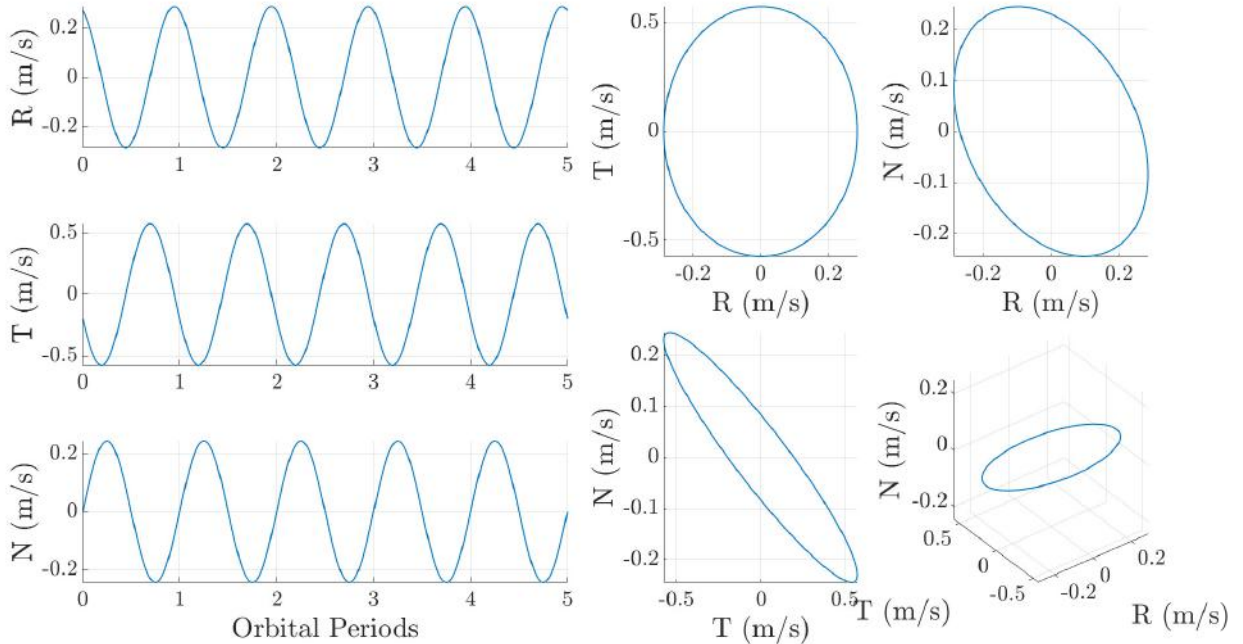


Figure 2.2: Numerically integrated relative RTN velocity using the non-linear equations of relative motion.

### 2.1.c Analytical Solution to Fundamental Orbital Differential Equations

We choose to analytically solve for the absolute position of the chief and deputy using the fundamental orbital differential equations in order to adequately compare with the nonlinear relative equations of motion. We can then take the difference between the vectors in ECI, and perform a transformation from ECI to RTN as was done in 1.2.d. The resulting relative positions and velocities of the deputy with respect to the chief in the RTN frame is shown in Figure 2.3 and 2.4. Due to the fact that the numerical and analytical simulations show extremely small error, the position and velocity plots appear indistinguishable as they are stacked on top of one another as will be discussed in the next section.

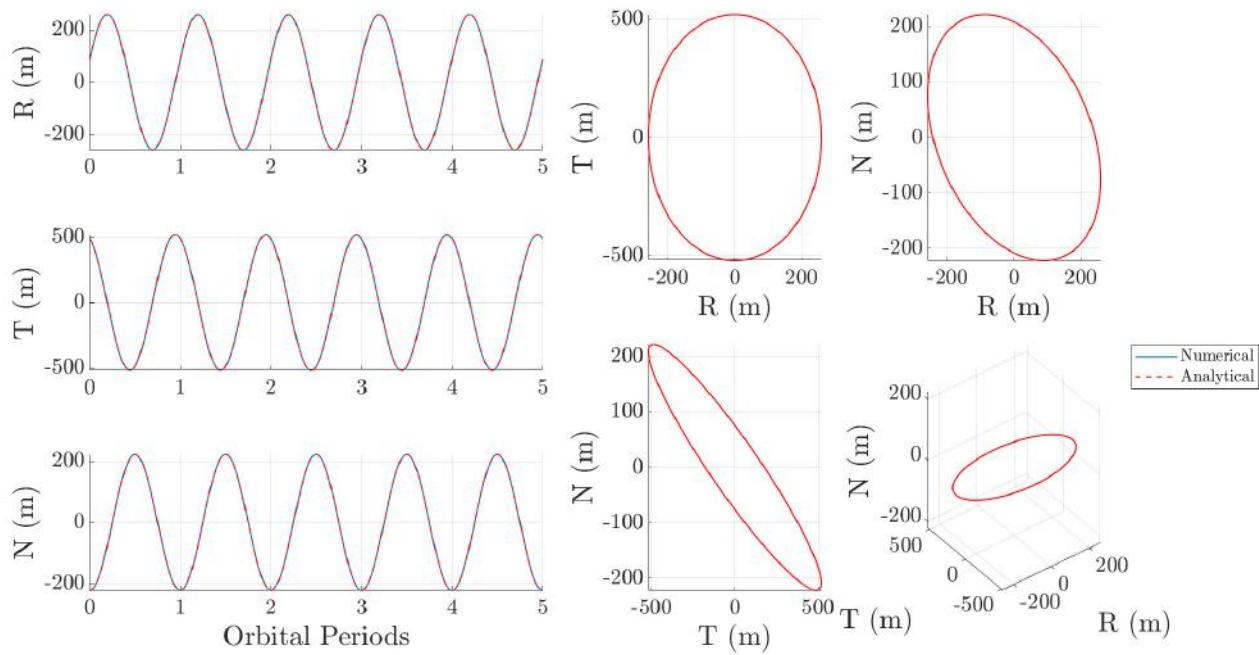


Figure 2.3: Overlaid numerically integrated (blue) and analytically determined (red) relative RTN position.

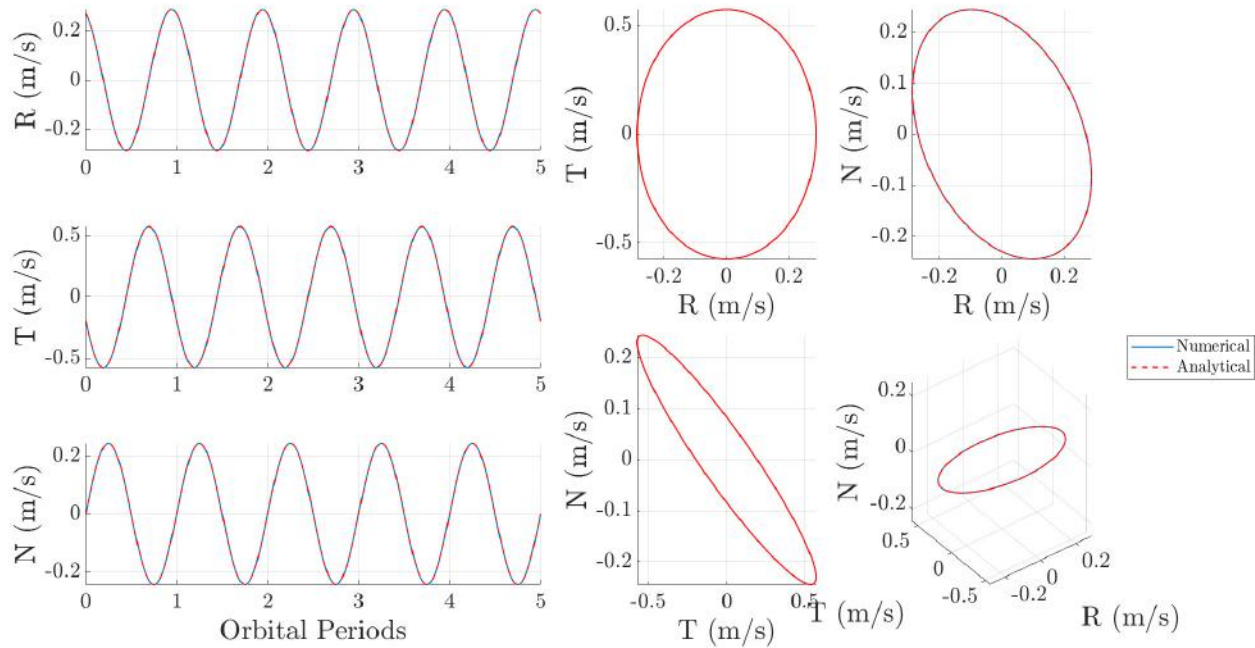


Figure 2.4: Overlaid numerically integrated (blue) and analytically determined (red) relative RTN velocity.

### 2.1.d Numerical and Analytical Comparison

The relative position as found by the analytical equations exhibits periodicity in each component in the RTN frame and aligns closely with that found by the nonlinear numerical integration. Numerical error between the two approaches produces the largest difference on the order of micrometers ( $10^{-6}$  meters) in the along-track direction as shown in Figure 2.5. The error in velocity is even smaller as be seen in Figure 2.6.

When a 100m difference in introduced in the semi-major axis, errors between the numerical and analytical methods are much larger and exhibit growth over time as shown in Figure 2.7. Position error in the along-track direction is shown to grow unbounded due to the along-track drift since energy-matching no longer holds. In Figure 2.8, it is observed that the along-track position is no longer bounded.

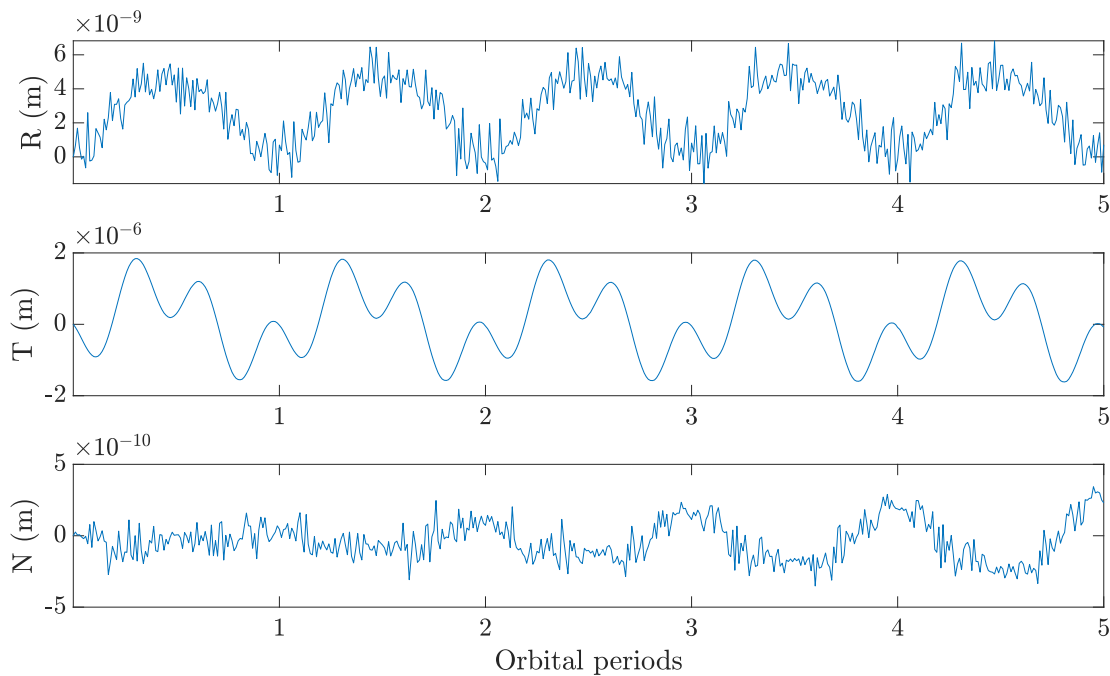


Figure 2.5: Position error in the RTN frame between the numerical and analytical solutions.

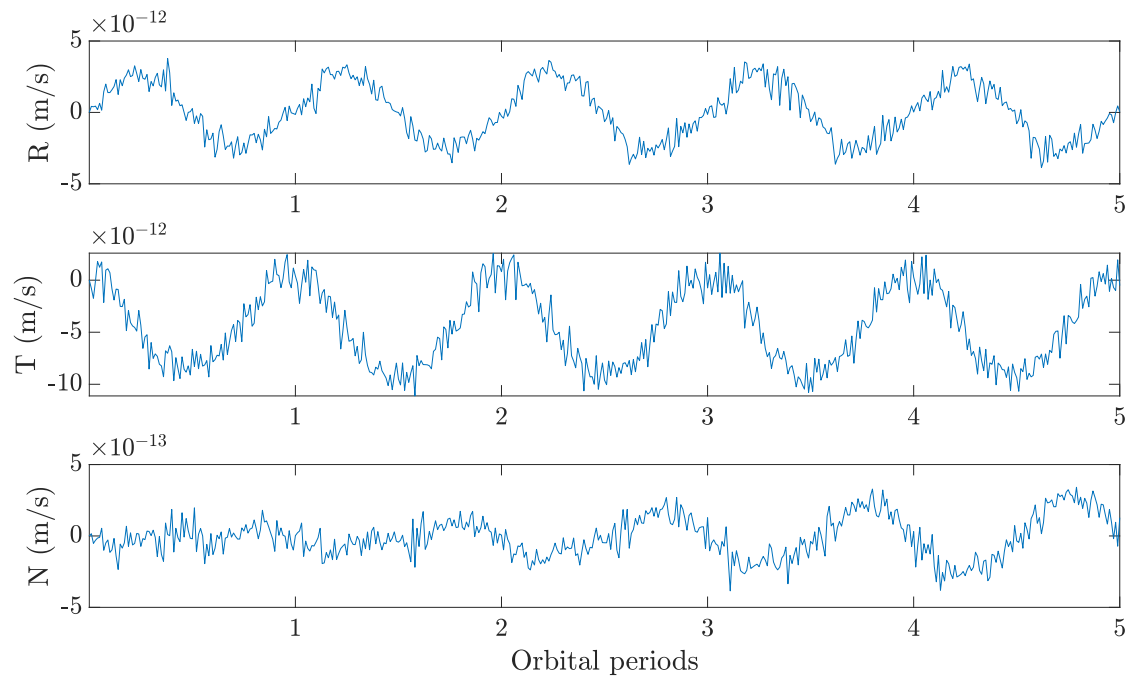


Figure 2.6: Velocity error in the RTN frame between the numerical and analytical solutions.

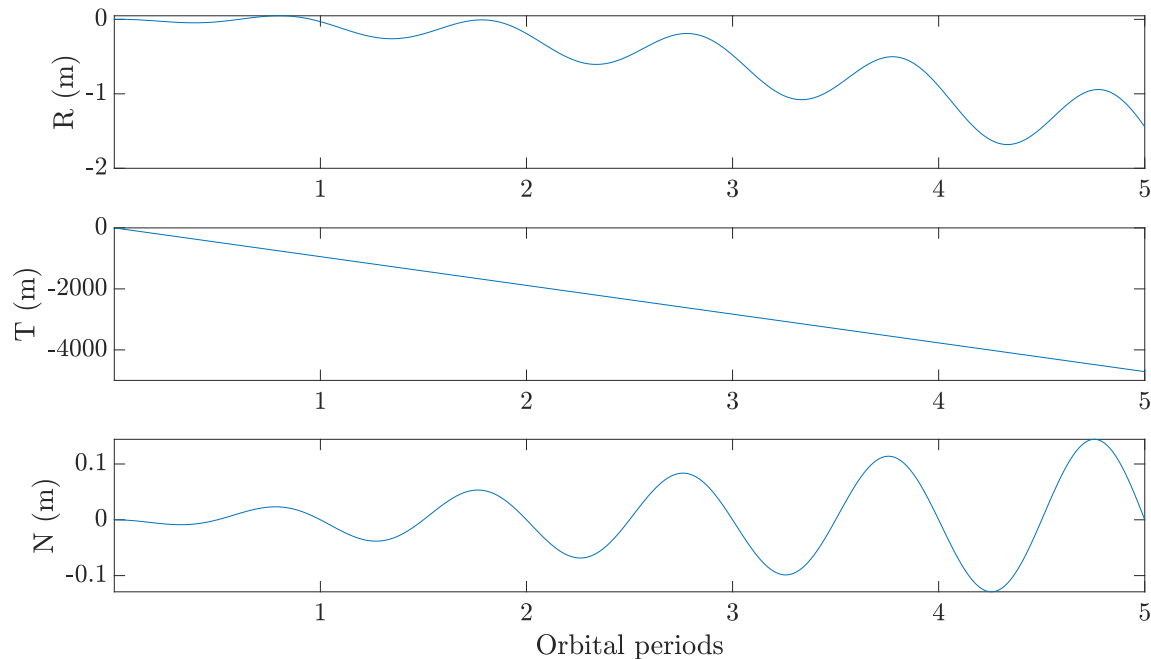


Figure 2.7: Position error between the numerical and analytical solutions with a 100m difference in initial semi-major axis.

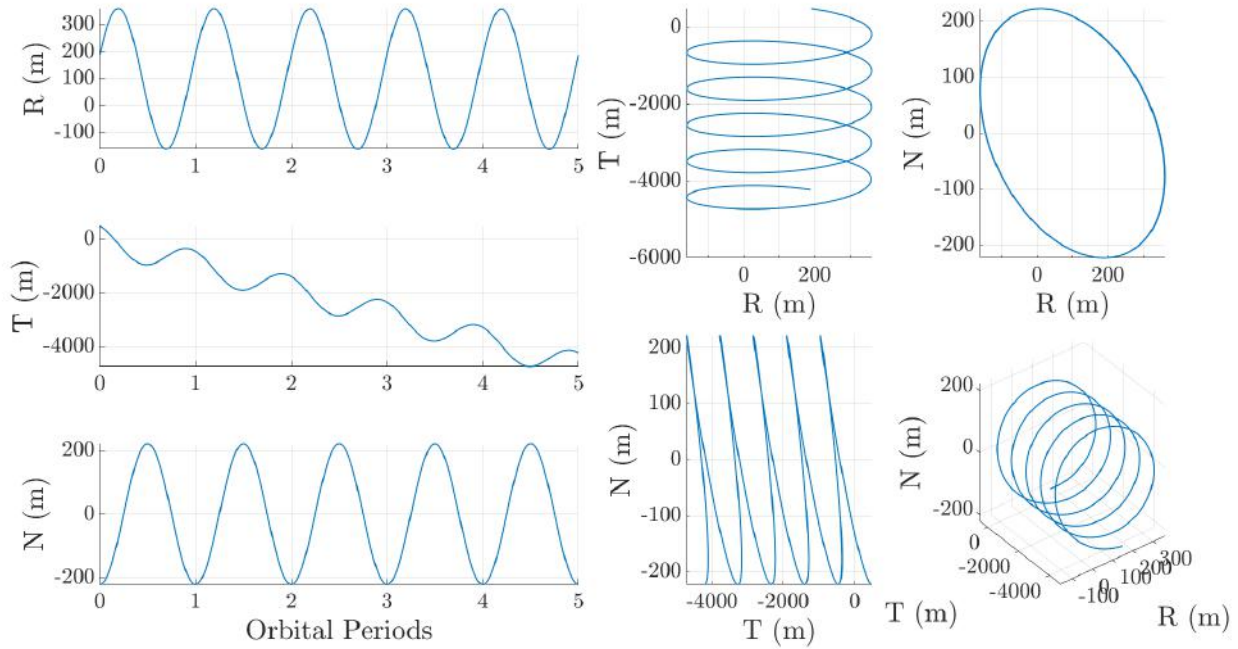


Figure 2.8: Numerically integrated relative RTN position with a 100m difference in initial semi-major axis.

### 2.1.e Drift Correction Maneuver

To correct for the drift, an impulsive maneuver is executed to lower the semi-major axis by 100m and re-establish periodicity between the chief and deputy. Due to the Oberth effect, the location at which a maneuver will have the largest effect on the specific mechanical energy (and therefore require the lowest fuel) is the point of largest velocity magnitude. This occurs at the periapsis as is seen in the vis-viva equation. For perfectly circular orbits, the location of the maneuver is not as relevant since the velocity magnitude is constant – the  $\Delta v$  required does not significantly vary from one location to another. However, to be as precise as possible, we will implement this maneuver at the periapsis of the deputy's orbit since its orbit is slightly eccentric.

The required  $\Delta v$  of the maneuver can be calculated using the Gauss Variational Equations, expressed in the velocity frame in the following equations. Note that the velocity frame is equivalent to the RTN frame at periapsis.

$$\frac{da}{dt} = \frac{2a^2 v}{\mu} a_v \quad (40)$$

$$\Delta a = \frac{2a^2 v_p}{\mu} \Delta v_T \rightarrow \Delta v_T = \Delta a \frac{\mu}{2a^2 v_p} \quad (41)$$

$$v_p = \sqrt{\mu \left( \frac{2}{r_p} - \frac{1}{a} \right)}, \quad r_p = a(1 - e) \quad (42)$$

Therefore, we will have an impulsive maneuver at periapsis in the along-track direction of:

$$\Delta v_T = -0.0552 \text{ m/s}$$

### 2.1.f Maneuver Simulation

As shown in Figure 2.9, the applied  $\Delta v_T$  maneuver (which was applied to change only the semi-major axis) corrects the along-track drift and restores periodic relative motion between the two spacecraft.

Since the orbit simulation begins at the periapsis, after 3 orbits the  $\Delta v_T$  is applied. This is observed as a discontinuity in the along-track velocity component at the beginning of the third orbit as shown in Figure 2.10.

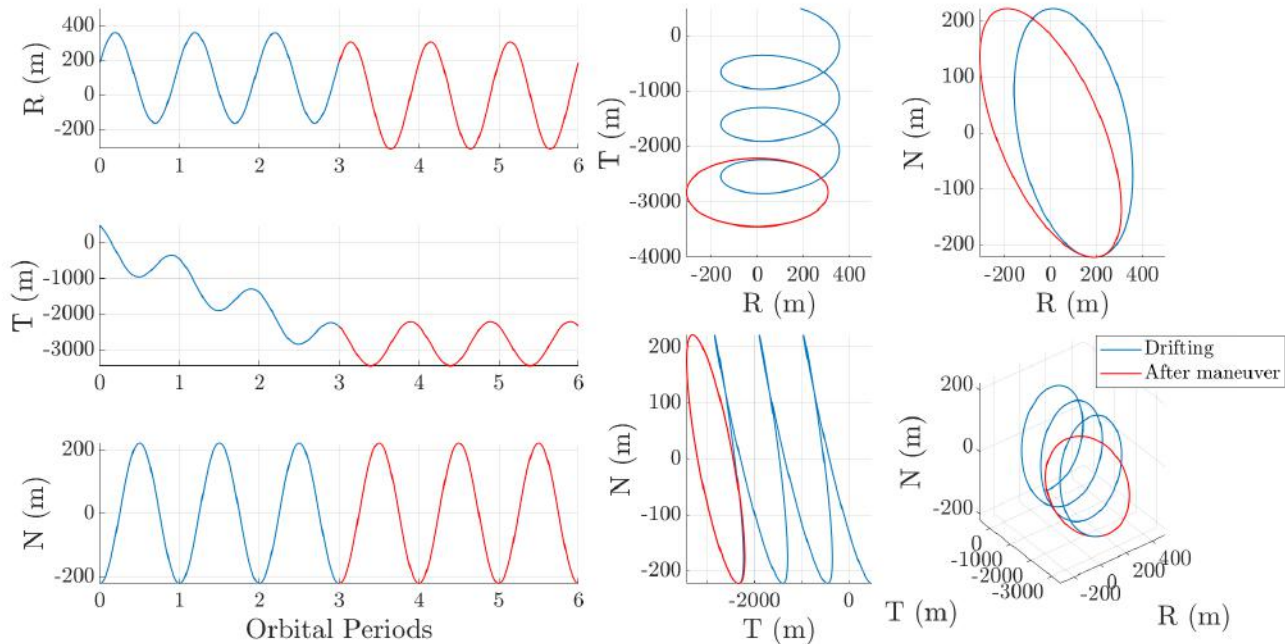


Figure 2.9: Numerically integrated relative RTN position before (blue) and after (red) the maneuver.

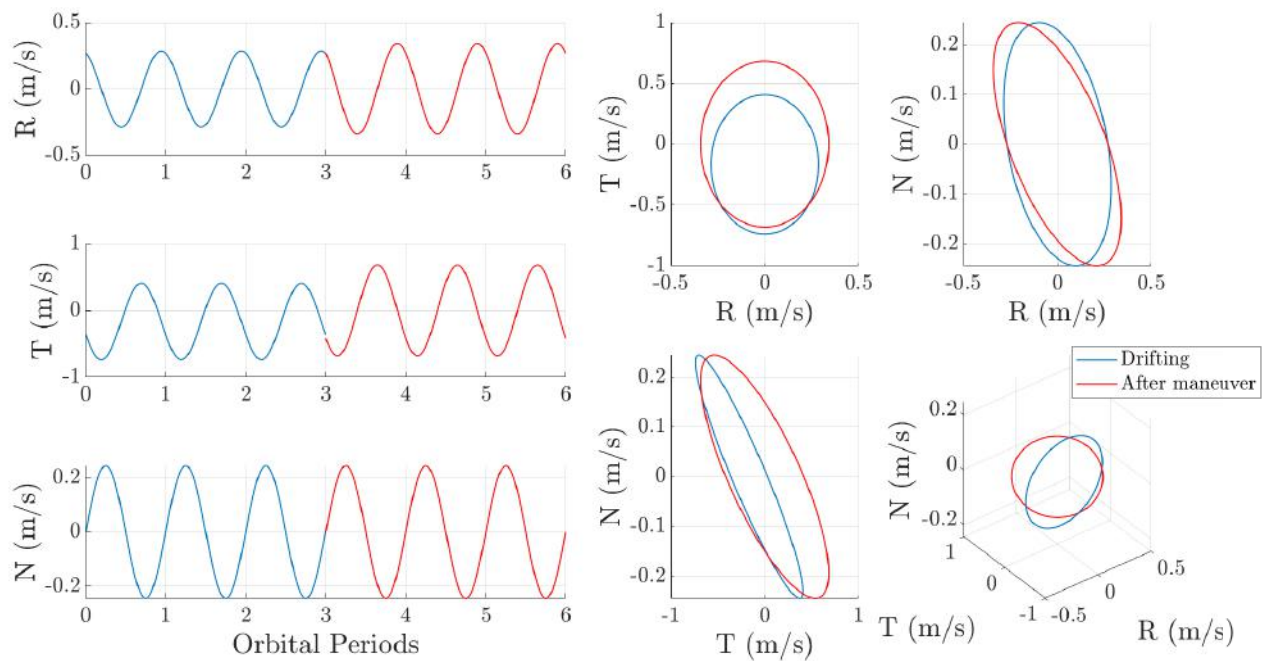


Figure 2.10: Numerically integrated relative RTN velocity before (blue) and after (red) the maneuver.

### 3 Problem Set 3

#### 3.1 Problem 1: We are Close in Near-Circular Orbits

##### 3.1.a Initial Conditions

The linearized equations of relative motion known as Hill-Clohessy-Wilshire (HCW) are valid for the previously defined orbit, satisfying the assumptions of small relative motion with respect to the orbit radius ( $\rho = 0.00008r_0$ ) and near-circular eccentricity ( $e_0 = 0.0001$ ,  $e_1 = 0.00009$ ). The same initial orbital elements in Table 2.1 satisfy these assumptions and will be used in the following analysis.

##### 3.1.b Initial Position and Velocity

By the same procedure to convert from orbital elements as described by Eqns. 1-3, the initial positions and velocity of the chief and deputy are calculated to be:

$$\begin{aligned} {}^I\vec{r}_{0,ECI} &= [0 \quad -6892.2 \quad 0] \text{ km} \\ {}^I\vec{v}_{0,ECI} &= [-984.8 \quad 0 \quad 7541.2] \text{ m/s} \\ {}^I\vec{r}_{1,ECI} &= [156.8 \quad -6892.3 \quad 513.3] \text{ km} \\ {}^I\vec{v}_{1,ECI} &= [-984.8 \quad 0.2696 \quad 7541.1] \text{ m/s} \end{aligned}$$

In the chief RTN frame, relative position may be determined by a coordinate transform, and relative velocity by a coordinate transform and application of the Theorem of Coriolis as given by Eqns. 33-38.

$$\begin{aligned} {}^{RTN}\vec{\rho}_{0,RTN} &= [88.914 \quad 488.656 \quad -221.981] \text{ m} \\ {}^{RTN}\vec{\dot{\rho}}_{0,RTN} &= [0.270 \quad -0.196 \quad 9.198 \times 10^{-6}] \text{ m/s} \end{aligned}$$

The absolute orbit elements corresponding to this motion in the inertial frame are given in Table 2.1. Differences in orbit elements between the chief and deputy are shown in Table 3.1.

$\Delta a$	$\Delta e$	$\Delta i$	$\Delta \Omega$	$\Delta \omega$	$\Delta M$
0	$-5.965 \times 10^{-6}$	0	$3.248 \times 10^{-5}$	-0.3865	0.3865

Table 3.1: Differences in initial classical orbit elements between the deputy and the chief.

##### 3.1.c Hill-Clohessy-Wilshire Integration Constants

The solution to the HCW equations in matrix-vector form are expressed by:

$$\begin{bmatrix} x \\ y \\ z \\ \dot{x} \\ \dot{y} \\ \dot{z} \end{bmatrix} = \begin{bmatrix} aI_{3 \times 3} & 0_{3 \times 3} \\ 0_{3 \times 3} & anI_{3 \times 3} \end{bmatrix} \begin{bmatrix} 1 & \sin(nt) & \cos(nt) & 0 & 0 & 0 \\ -\frac{3}{2}nt & 2\cos(nt) & -2\sin(nt) & 1 & 0 & 0 \\ 0 & 0 & 0 & 0 & \sin(nt) & \cos(nt) \\ 0 & \cos(nt) & -\sin(nt) & 0 & 0 & 0 \\ -\frac{3}{2} & -2\sin(nt) & -2\cos(nt) & 0 & 0 & 0 \\ 0 & 0 & 0 & 0 & \cos(nt) & -\sin(nt) \end{bmatrix} \begin{bmatrix} K_1 \\ K_2 \\ K_3 \\ K_4 \\ K_5 \\ K_6 \end{bmatrix} \quad (43)$$

where  $n$  is defined as  $n = \sqrt{\frac{\mu}{a_0^3}}$ . Given the initial state at time  $t_0 = 0$ , the six integration constants  $K_1$  to  $K_6$  are found to be

$$\begin{bmatrix} K_1 \\ K_2 \\ K_3 \\ K_4 \\ K_5 \\ K_6 \end{bmatrix} = \begin{bmatrix} -1.490 \times 10^{-8} \\ 3.545 \times 10^{-5} \\ 1.291 \times 10^{-5} \\ -1.447 \times 10^{-8} \\ 1.210 \times 10^{-9} \\ -3.220 \times 10^{-5} \end{bmatrix}$$

### 3.1.d HCW in Rectilinear Coordinates

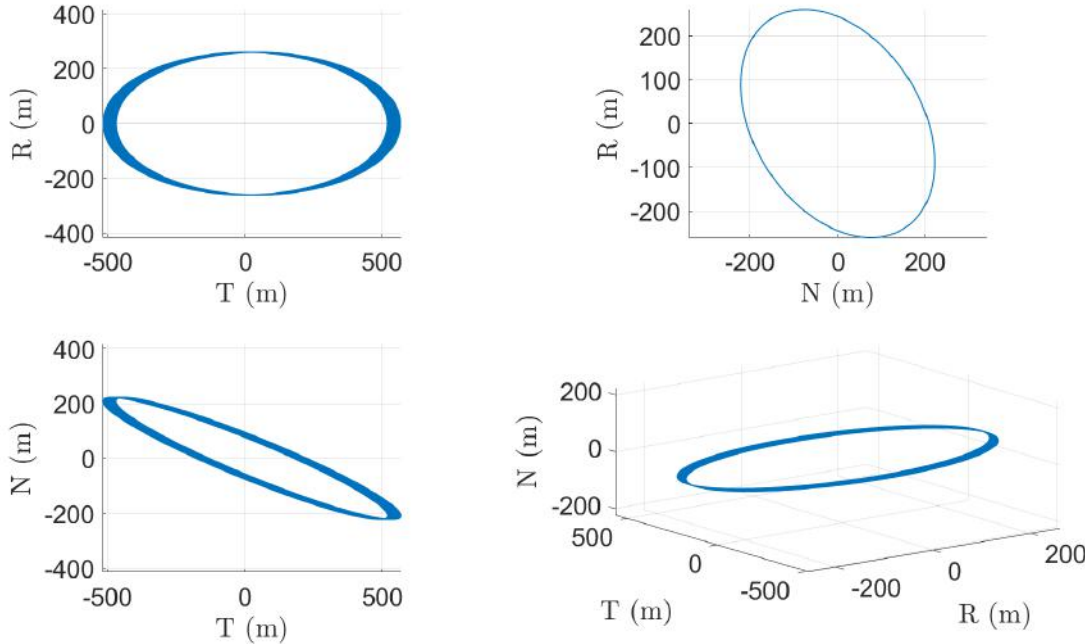


Figure 3.1: Numerically integrated relative RTN position from HCW equations over 50 orbits.

The homogeneous HCW equations are given by the following, assuming no disturbing or control forces:

$$\ddot{x} - 2n\dot{y} - 3n^2x = 0 \quad (44)$$

$$\ddot{y} + 2n\dot{x} = 0 \quad (45)$$

$$\ddot{z} + n^2z = 0 \quad (46)$$

Starting from the initial conditions and integrating these equations over 50 orbits, we observe that the relative motion between the chief and the deputy is periodic as shown in by the position plots in Figure 3.1 and the velocity plots in Figure 3.2. In each of the TR, NR, and TN planes, the motion of the deputy is elliptic.

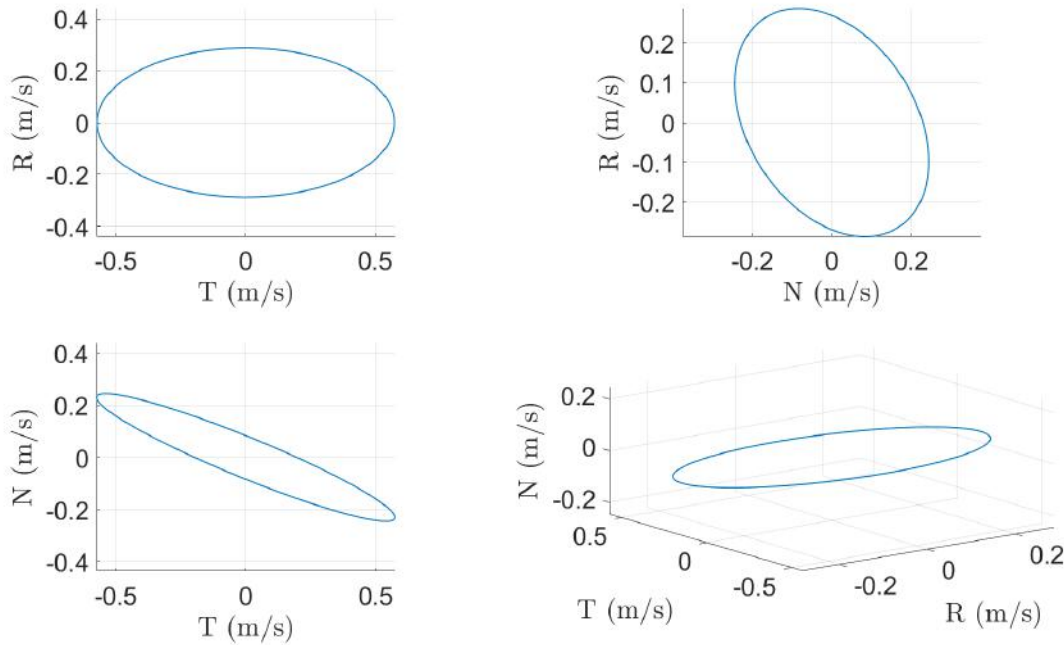


Figure 3.2: Numerically integrated relative RTN velocity from HCW equations over 50 orbits.

### 3.1.e HCW in Rectilinear Coordinates

With an initial difference in eccentricity and inclination but identical semi-major axes, the relative motion appears periodic as expected by the energy matching condition. The motion in the TR plane forms a 2-by-1 ellipse with semi-minor axis as a function of the integration constants given by  $a\sqrt{(K_2^2 + K_3^2)}$ . Upon inspection across 50 orbits, there is an along-track drift as shown in Figure 3.3. This behavior is expected from the solution to the HCW equations in which the position in y grows linearly with time. Though the energy matching condition is met, there is unbounded motion inherent in the HCW solution. This can be mitigated by setting the initial conditions such that  $\dot{y}(0) = 2nx(0)$ , driving the secular term to zero.

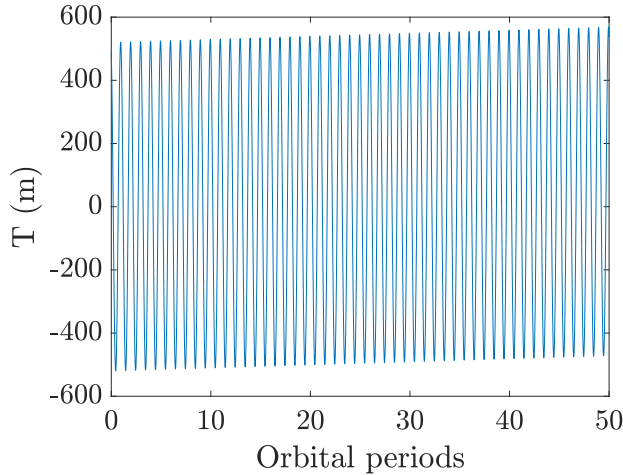


Figure 3.3: Along-track drift apparent in HCW solution over 50 orbits.

### 3.2 Problem 2: We are Close in Eccentric Orbits

#### 3.2.a Initial Conditions

For eccentric orbits, the Yamanaka-Ankersen solution employs true anomaly as the independent variable. First, an orbit with the original semi-major axis of 6892.927 km and a new eccentricity of 0.1 has a perigee below the Earth's surface. Therefore, for the purposes of this analysis, the periapsis radius is set to be equal to the original semi-major axis from Table 2.1 in order to calculate a physically feasible semi-major axis. The rest of the initial conditions remain unchanged and are given in Table 3.2.

$a$	$e$	$i$	$\Omega$	$\omega$	$f$
7658.808 km	0.1	97.44°	270°	0°	0°

Table 3.2: Initial orbital elements of the chief for eccentric orbit simulation.

We follow a similar procedure as in 3.1.b to obtain the initial relative position and velocities in RTN:

$$\begin{aligned} {}^{RTN}\vec{\rho}_{0,RTN} &= [88.914 \quad 508.136 \quad -199.803] \text{ m} \\ {}^{RTN}\vec{\dot{\rho}}_{0,RTN} &= [0.288 \quad -0.196 \quad 9.147 \times 10^{-6}] \text{ m/s} \end{aligned}$$

This new set of orbital elements are set to be valid under the Tschauner-Hempel (TH) equations, satisfying small relative motion compared to the radius of periapsis ( $\rho = 0.00008r_0$ ) and equal semi-major axes.

#### 3.2.b Yamanaka-Ankersen Integration Constants

The YA solution obtains the relative state at any time from a given initial state. In matrix-vector form, this can also be expressed using integration constants as given by:

$$\begin{bmatrix} x \\ y \\ z \\ \dot{x} \\ \dot{y} \\ \dot{z} \end{bmatrix} = \begin{bmatrix} a\eta^2 I_{3 \times 3} & 0_{3 \times 3} \\ 0_{3 \times 3} & \frac{an}{\eta} I_{3 \times 3} \end{bmatrix} \begin{bmatrix} \Psi_{x,1} & \Psi_{x,2} & \Psi_{x,3} & 0 & 0 & 0 \\ \Psi_{y,1} & \Psi_{y,2} & \Psi_{y,3} & \Psi_{y,4} & 0 & 0 \\ 0 & 0 & 0 & 0 & \Psi_{z,5} & \Psi_{z,6} \\ \Psi_{\dot{x},1} & \Psi_{\dot{x},2} & \Psi_{\dot{x},3} & 0 & 0 & 0 \\ \Psi_{\dot{y},1} & \Psi_{\dot{y},2} & \Psi_{\dot{y},3} & \Psi_{\dot{y},4} & 0 & 0 \\ 0 & 0 & 0 & 0 & \Psi_{\dot{z},5} & \Psi_{\dot{z},6} \end{bmatrix} \begin{bmatrix} K_1 \\ K_2 \\ K_3 \\ K_4 \\ K_5 \\ K_6 \end{bmatrix} \quad (47)$$

In this form, the non-dimensional coefficients are defined by the following:

$$\begin{aligned} \Psi_{x,1} &= \frac{1}{k} + \frac{3}{2}k'f & \Psi_{x,2} &= \sin f & \Psi_{x,3} &= \cos f \\ \Psi_{y,1} &= -\frac{3}{2}k\tau & \Psi_{y,2} &= (1 + \frac{1}{k}) \cos f & \Psi_{y,3} &= -(1 + \frac{1}{k}) \sin f & \Psi_{y,4} &= \frac{1}{k} \\ \Psi_{z,5} &= \frac{1}{k} \sin f & \Psi_{z,6} &= \frac{1}{k} \cos f \\ \Psi_{\dot{x},1} &= \frac{k'}{2} - \frac{3}{2}k^2(k-1)\tau & \Psi_{\dot{x},2} &= k^2 \cos f & \Psi_{\dot{x},3} &= -k^2 \sin f \\ \Psi_{\dot{y},1} &= -\frac{3}{2}(k+k^2k'\tau) & \Psi_{\dot{y},2} &= -(k^2+1) \sin f & \Psi_{\dot{y},3} &= -e - (k^2+1) \cos f & \Psi_{\dot{y},4} &= -k' \\ \Psi_{\dot{z},5} &= e + \cos f & \Psi_{\dot{z},6} &= -\sin f \end{aligned}$$

For readability, the auxiliary variables are given by:

$$\begin{aligned} k &= 1 + e \cos f & k' &= \frac{dk}{df} = -e \sin f \\ \eta &= \sqrt{1 - e^2} & \tau &= \int_{f_0}^f \frac{df}{k^2} = \frac{nt}{\eta^3} \end{aligned}$$

Given the defined initial relative position and velocity, the six integration constants  $K_1$  to  $K_6$  may be obtained using the preceding equations. It is observed that the constants  $K_1$  and  $K_2$  are orders of magnitude smaller than the others.

$$\begin{bmatrix} K_1 \\ K_2 \\ K_3 \\ K_4 \\ K_5 \\ K_6 \end{bmatrix} = \begin{bmatrix} -8.504 \times 10^{-9} \\ 3.277 \times 10^{-5} \\ 1.173 \times 10^{-5} \\ 4.901 \times 10^{-6} \\ 1.147 \times 10^{-9} \\ -2.899 \times 10^{-5} \end{bmatrix}$$

### 3.2.c Yamanaka-Ankersen Solution

To solve for the relative motion, we propagate time and calculate the mean anomaly from the time elapsed. From mean anomaly, the eccentric anomaly is obtained through the Newton-Raphson algorithm and used to compute true anomaly. The relative state can then be calculated at each time step from true anomaly by Equation 47. The propagated relative motion over 15 orbits is observed to be safe and periodic as shown in Figure 3.4 and Figure 3.5.

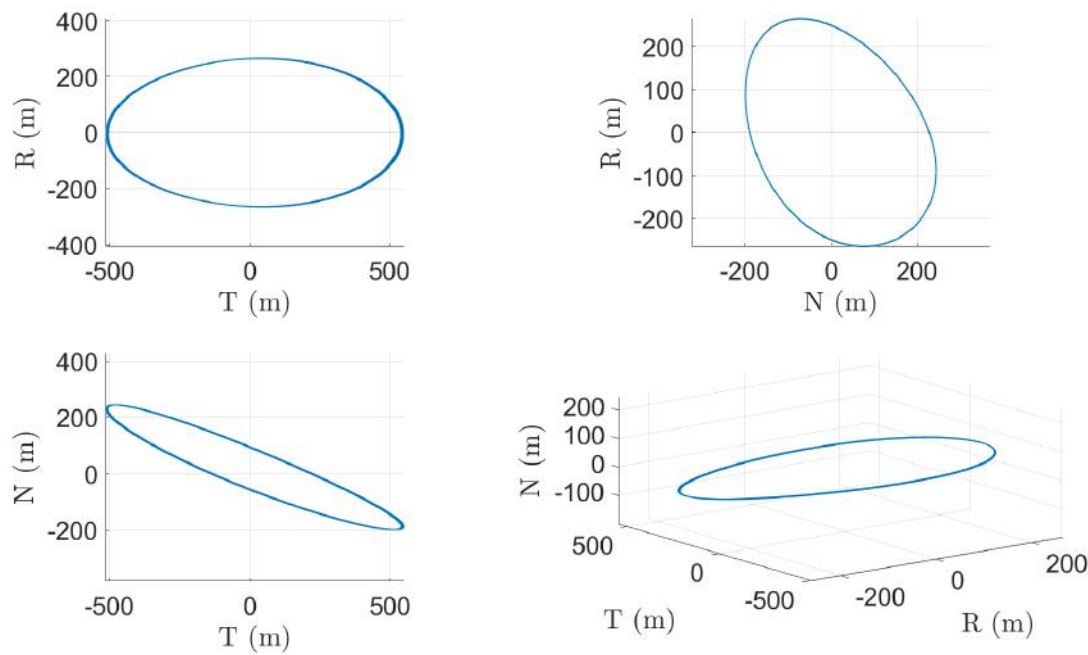


Figure 3.4: Relative RTN position from YA solution over 15 orbits.

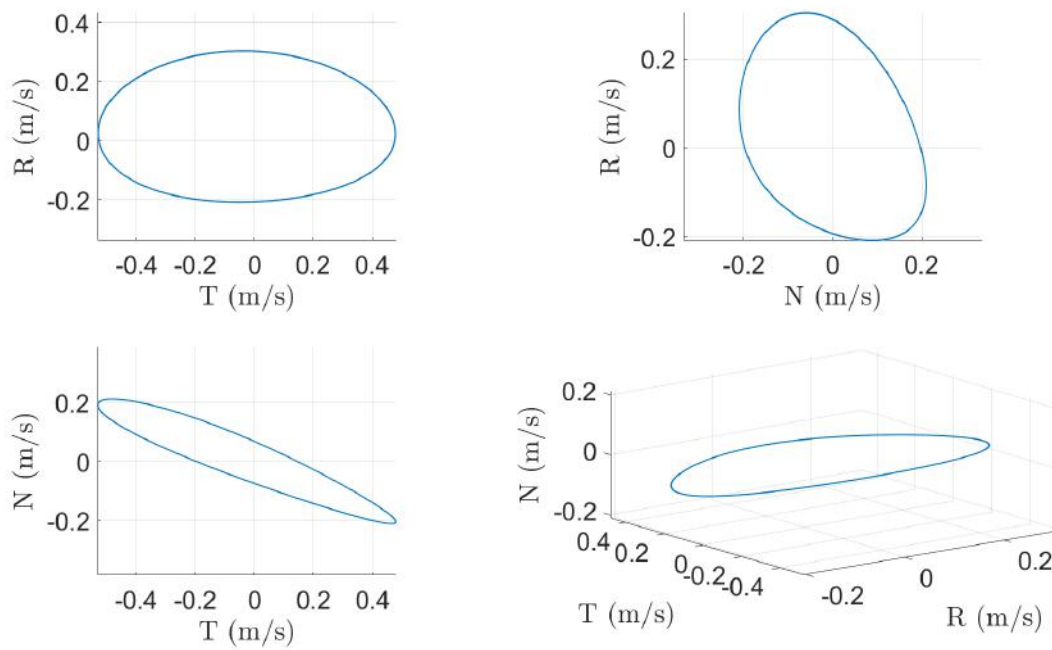


Figure 3.5: Relative RTN velocity from YA solution over 15 orbits.

### 3.2.d Discussion of YA Solution

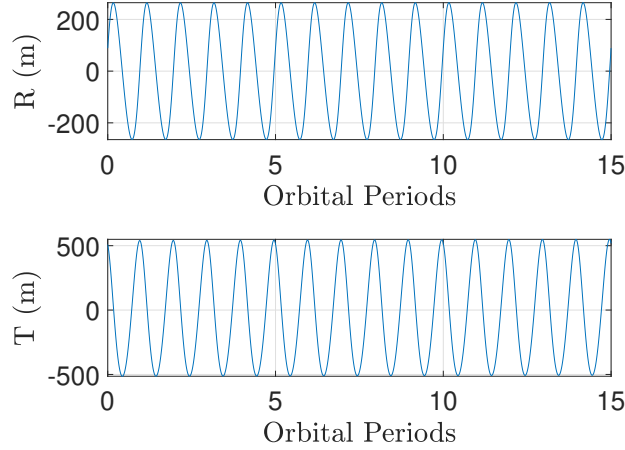


Figure 3.6: Relative radial and along-track position from YA solution.

Given the nature of the state transition matrix (STM) in Equation 47, we generally expect unbounded motion in  $x$  and  $y$ , and bounded periodic motion in  $z$ . As can be seen by the terms containing  $\tau$ , the  $\bar{x}$  and  $\bar{y}$  positions grow with time, resulting in an along-track drift and a growing amplitude in radial position over time. However, from Figure 3.4, we do not see any unbounded motion. Plots of  $x$  and  $y$  relative position over time in Figure 3.6 confirms the motion is periodic. The reason for this becomes clear when we consider the integration constants. Although unbounded motion may be expected by definition of the STM, the elements in the STM responsible for secular behavior are multiplied by  $K_1$ . From 3.2.b, the value of this integration constant is negligibly small (on the order of  $10^{-9}$ ), which leads to a unnoticeably unbounded motion over 15 orbits. We might expect this minute unbounded motion to appear after many orbits. To suppress instabilities in the YA solution, the motion may be bounded by choosing relative orbit parameters that allow  $K_1 = 0$ .

### 3.2.e Quasi-Nonsingular Relative Orbit Elements

The quasi-nonsingular relative orbit elements are defined by a linear combination of the absolute elements of the chief and deputy defined by [9]:

$$\begin{bmatrix} \delta a \\ \delta \lambda \\ \delta e_x \\ \delta e_y \\ \delta i_x \\ \delta i_y \end{bmatrix} = \begin{bmatrix} (a_1 - a_0)/a_0 \\ (u_1 - u_0) + (\Omega_1 - \Omega_0) \cos i_0 \\ e_{x1} - e_{x0} \\ e_{y1} - e_{y0} \\ i_1 - i_0 \\ (\Omega_1 - \Omega_0) \sin i_0 \end{bmatrix} \quad (48)$$

Normalized by the semi-major axis of the chief orbit  $a_0$ , the defined initial conditions are calculated to be:

$$a_0 \begin{bmatrix} \delta a \\ \delta \lambda \\ \delta e_x \\ \delta e_y \\ \delta i_x \\ \delta i_y \end{bmatrix} = \begin{bmatrix} 0 \\ 0 \\ -88.925 \\ -244.320 \\ 0 \\ 222 \end{bmatrix}$$

These relations may be used to map orbital elements to relative position in the RTN frame as described in the next section.

### 3.2.f Relative Orbital Elements Geometric Linear Mapping

For eccentric orbits, a geometric mapping relates the RTN relative position at time  $t$  to the quasi-nonsingular relative orbital elements at initial time  $t_0 = 0$  [10]. The mapping mirrors the YA solution, where the integration constants are replaced by the quasi-nonsingular orbit elements as given by:

$$\begin{bmatrix} x \\ y \\ z \\ \dot{x} \\ \dot{y} \\ \dot{z} \end{bmatrix} = \begin{bmatrix} a\eta^2 I_{3 \times 3} & 0_{3 \times 3} \\ 0_{3 \times 3} & \frac{an}{\eta} I_{3 \times 3} \end{bmatrix} \begin{bmatrix} b_{x,1} & b_{x,2} & b_{x,3} & b_{x,4} & 0 & b_{x,6} \\ b_{y,1} & b_{y,2} & b_{y,3} & b_{y,4} & 0 & b_{y,6} \\ 0 & 0 & 0 & 0 & b_{z,5} & b_{z,6} \\ b_{\dot{x},1} & b_{\dot{x},2} & b_{\dot{x},3} & b_{\dot{x},4} & 0 & b_{\dot{x},6} \\ b_{\dot{y},1} & b_{\dot{y},2} & b_{\dot{y},3} & b_{\dot{y},4} & 0 & b_{\dot{y},6} \\ 0 & 0 & 0 & 0 & b_{\dot{z},5} & b_{\dot{z},6} \end{bmatrix} \begin{bmatrix} \delta a \\ \delta \lambda \\ \delta e_x \\ \delta e_y \\ \delta i_x \\ \delta i_y \end{bmatrix} \quad (49)$$

The non-dimensional coefficients are defined by:

$$\begin{aligned} b_{x,1} &= \frac{1}{k} + \frac{3}{2} k' \frac{n}{\eta^3} t & b_{x,3} &= \frac{1}{\eta^3} \left[ e_x \left( \frac{k-1}{1+\eta} \right) - \cos u \right] \\ b_{x,2} &= -\frac{k'}{\eta^3} & b_{x,4} &= \frac{1}{\eta^3} \left[ c_y \left( \frac{k-1}{1+\eta} \right) - \sin u \right] \\ b_{x,6} &= \frac{k'}{\eta^3} \cot i & & \\ b_{y,1} &= -\frac{3}{2} k \frac{n}{\eta^3} t & b_{y,3} &= \frac{1}{\eta^2} \left[ \left( 1 + \frac{1}{k} \right) \sin u + \frac{e_y}{k} + \frac{k}{\eta} \left( \frac{e_y}{1+\eta} \right) \right] \\ b_{y,2} &= \frac{k}{\eta^3} & b_{y,4} &= -\frac{1}{\eta^2} \left[ \left( 1 + \frac{1}{k} \right) \cos u + \frac{e_x}{k} + \frac{k}{\eta} \left( \frac{e_x}{1+\eta} \right) \right] \\ b_{y,6} &= \left( \frac{1}{k} - \frac{k}{\eta^3} \right) \cot i & & \\ b_{z,5} &= \frac{1}{k} \sin u & b_{z,6} &= -\frac{1}{k} \cos u \\ b_{\dot{x},1} &= \frac{k'}{2} + \frac{3}{2} k^2 (1-k) \frac{n}{\eta^3} t & b_{\dot{i},3} &= \frac{k^2}{\eta^3} \left[ \eta \sin u + e_y \left( \frac{k-1}{1+\eta} \right) \right] \\ b_{\dot{x},2} &= \frac{k^2}{\eta^3} (k-1) & b_{\dot{x},4} &= -\frac{k^2}{\eta^3} \left[ \eta \cos u + e_x \left( \frac{k-1}{1+\eta} \right) \right] \\ b_{\dot{i},6} &= -\frac{k^2}{\eta^3} (k-1) \cot i & & \end{aligned}$$

$$\begin{aligned}
 b_{\dot{y},1} &= -\frac{3}{2}k \left(1 + kk' \frac{n}{\eta^3} t\right) & b_{\dot{y},3} &= \left(1 + \frac{k^2}{\eta^3}\right) \cos u + e_x \frac{k}{\eta^2} \left[1 + \frac{k}{\eta} \left(\frac{1-k}{1+\eta}\right)\right] \\
 b_{\dot{y},2} &= \frac{k^2}{\eta^3} k' & b_{\dot{y},4} &= \left(1 + \frac{k^2}{\eta^3}\right) \sin u + e_y \frac{k}{\eta^2} \left[1 + \frac{k}{\eta} \left(\frac{1-k}{1+\eta}\right)\right] \\
 b_{\dot{j},6} &= -\left(1 + \frac{k^2}{\eta^3}\right) k' \cot i
 \end{aligned}$$

By propagating the true anomaly as the independent variable, relative motion in the RTN frame may be obtained. The resulting position and velocity, normalized by the semi-major axis of the chief is plotted on top of the YA solution in Figure 3.7 and Figure 3.8. The solutions overlap closely as there are small errors between them.

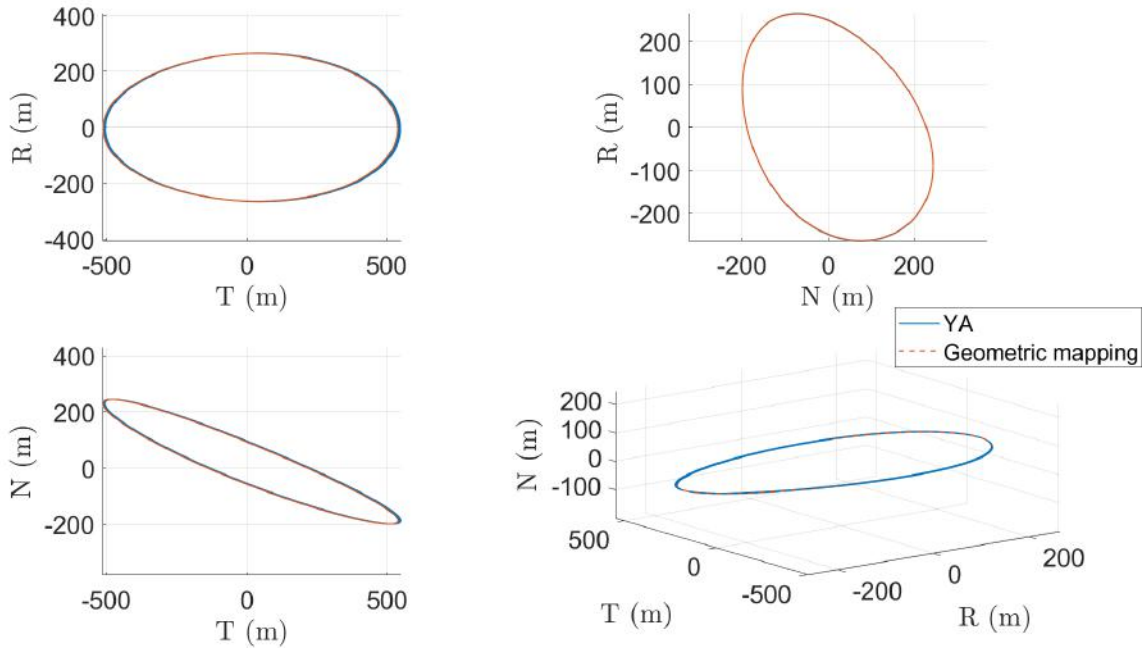


Figure 3.7: Relative RTN position from YA solution (blue) and geometric linear mapping (orange).

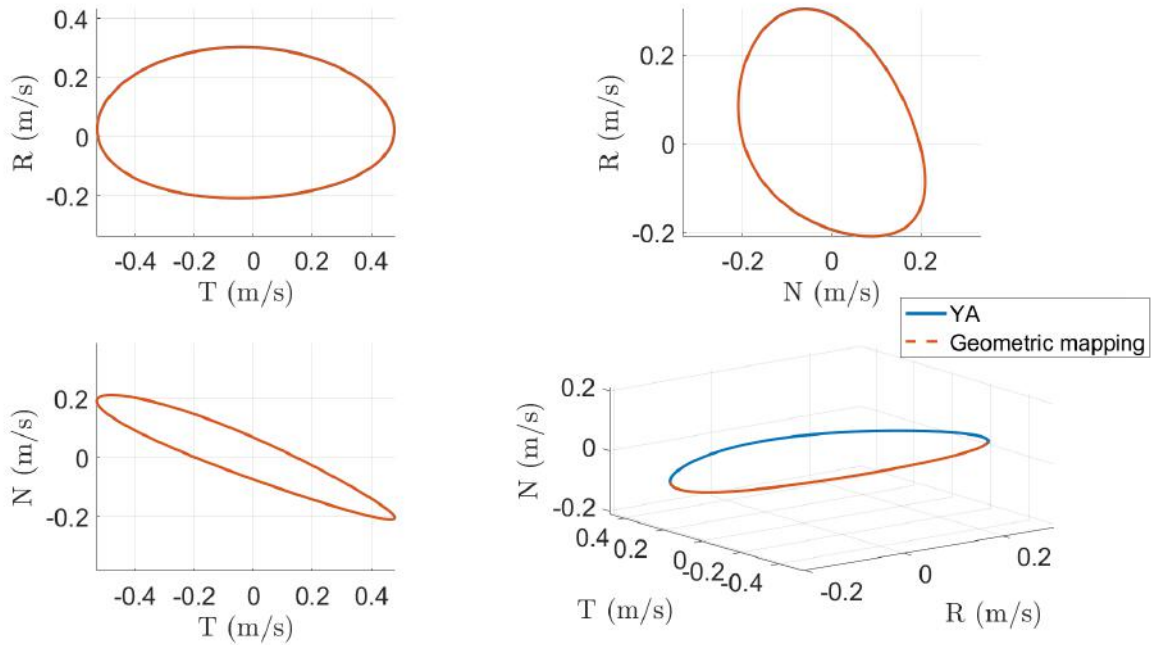


Figure 3.8: Relative RTN velocity from YA solution (blue) and geometric linear mapping (orange).

### 3.2.g Relationship between Relative Orbital Elements and YA Integration Constants

Although the geometric mapping updates position and velocity differently than the YA solution, the end result is quite similar. The initial ROEs and integration constants were computed to be:

$$\begin{bmatrix} \delta a \\ \delta \lambda \\ \delta e_x \\ \delta e_y \\ \delta i_x \\ \delta i_y \end{bmatrix} = \begin{bmatrix} 0 \\ 0 \\ -1.161 \times 10^{-5} \\ -3.190 \times 10^{-5} \\ 0 \\ 2.899 \times 10^{-5} \end{bmatrix}, \quad \begin{bmatrix} K_1 \\ K_2 \\ K_3 \\ K_4 \\ K_5 \\ K_6 \end{bmatrix} = \begin{bmatrix} -8.504 \times 10^{-9} \\ 3.277 \times 10^{-5} \\ 1.173 \times 10^{-5} \\ 4.901 \times 10^{-6} \\ 1.147 \times 10^{-9} \\ -2.899 \times 10^{-5} \end{bmatrix}$$

The initial ROEs and the YA integration constants are not equivalent, but we do notice that if we compare the values individually, there are several similarities. The first two integration constants  $K_1$  and  $K_2$  are close to matching  $\delta a$  and  $\delta e_y$ .  $K_3$  matches well with the  $\delta e_x$ , and  $K_4$  is nearly 0 like  $\delta \lambda$ . The last two integration constants  $K_5$  and  $K_6$  are similar in magnitude to the relative inclination vector. There are some differences in the values and the phases (numeric sign), but in general the orders of magnitude are quite similar.

An equivalence between the quasi-nonsingular ROEs and the YA integration constants is established by

the defined linear mapping [10]:

$$\begin{bmatrix} \delta a \\ \delta \lambda \\ \delta e_x \\ \delta e_y \\ \delta i_x \\ \delta i_y \end{bmatrix} = \begin{bmatrix} 1 & 0 & 0 & 0 & 0 & 0 \\ 0 & -e_x \left( \eta + \frac{1}{1+\eta} \right) & e_y \left( \eta + \frac{1}{1+\eta} \right) & 1 & 0 & 0 \\ 0 & e_x e_y & e_x^2 - 1 & -e_y & 0 & -e_y \cot i \\ 0 & e_y^2 - 1 & e_x e_y & e_x & 0 & e_x \cot i \\ 0 & 0 & 0 & 0 & 1 & 0 \\ 0 & 0 & 0 & 0 & 0 & -1 \end{bmatrix} \begin{bmatrix} K_1 \\ K_2 \\ K_3 \\ K_4 \\ K_5 \\ K_6 \end{bmatrix} \quad (50)$$

which evaluates to

$$\begin{bmatrix} \delta a \\ \delta \lambda \\ \delta e_x \\ \delta e_y \\ \delta i_x \\ \delta i_y \end{bmatrix} = \begin{bmatrix} -8.504 \times 10^{-9} \\ 3.277 \times 10^{-5} \\ 1.173 \times 10^{-5} \\ 4.901 \times 10^{-6} \\ 1.147 \times 10^{-9} \\ -2.899 \times 10^{-5} \end{bmatrix}$$

This mapping produces ROEs nearly indistinguishable from the YA integration constants except for small numerical variations on the order of  $10^{-5}$ .

### 3.2.h True Relative Propagation

To calculate the true relative position, we numerically integrate the non-linear relative equations of motion as described in 2.1.b. The result is plotted alongside the YA solution and the geometric mapping in Figure 3.9 and Figure 3.10, again demonstrating the numerical accuracy of the solutions with each other.

Figure 3.11 shows the errors compared to the true relative propagation from numerical integration. Error in the radial and along-track components using the YA solution to the TH equations in 3.2.c increases with the number of orbits, while the error using the geometric mapping appears to remain periodic and smaller by comparison. Higher accuracy observed in the geometric mapping model may be attributed to the use of relative orbital elements. Since ROEs describe angles rather than approximate Cartesian position as in the TH solution, higher-order errors in geometric mapping are smaller.

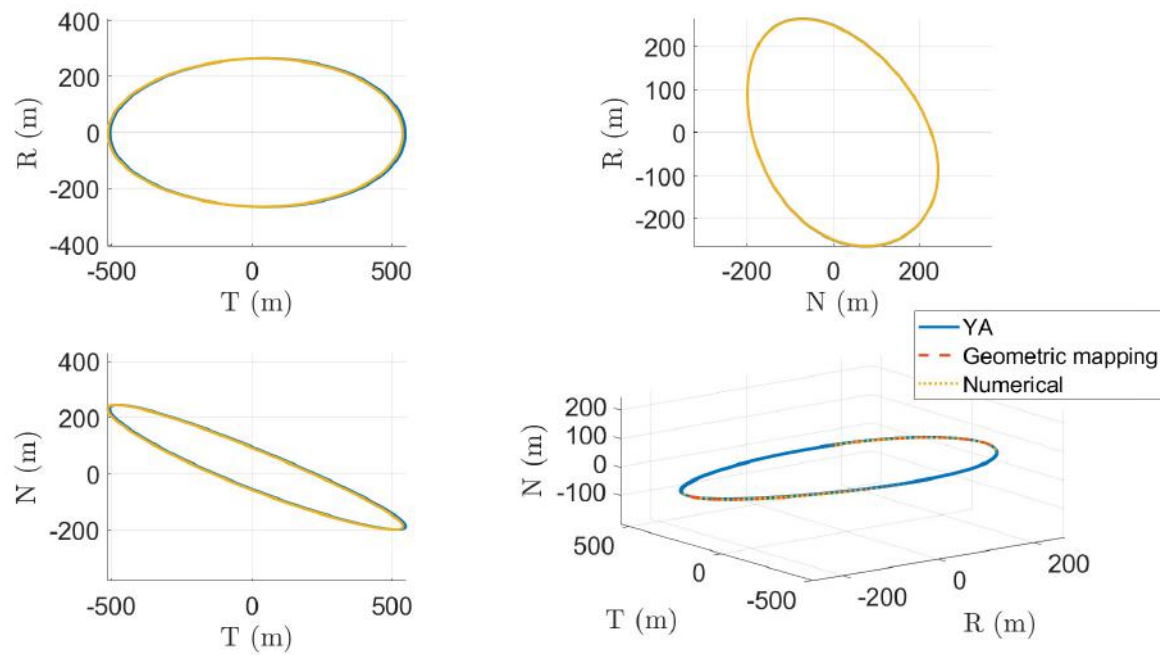


Figure 3.9: Relative RTN position from YA solution (blue), geometric linear mapping (orange), and numerical integration (yellow).

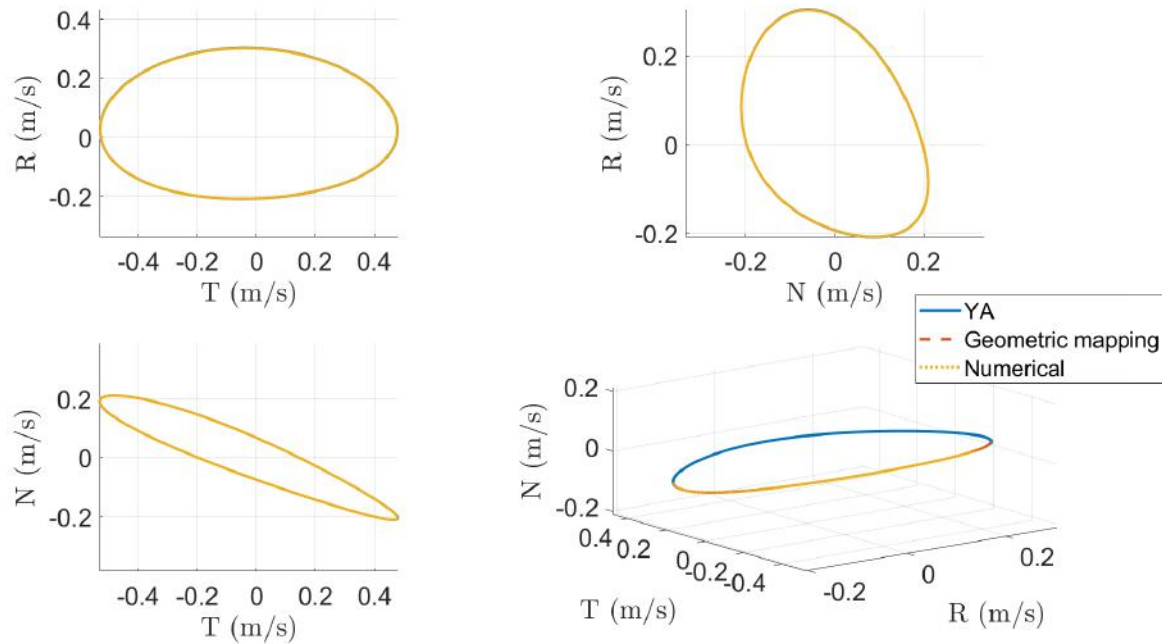


Figure 3.10: Relative RTN velocity from YA solution (blue), geometric linear mapping (orange), and numerical integration (yellow).

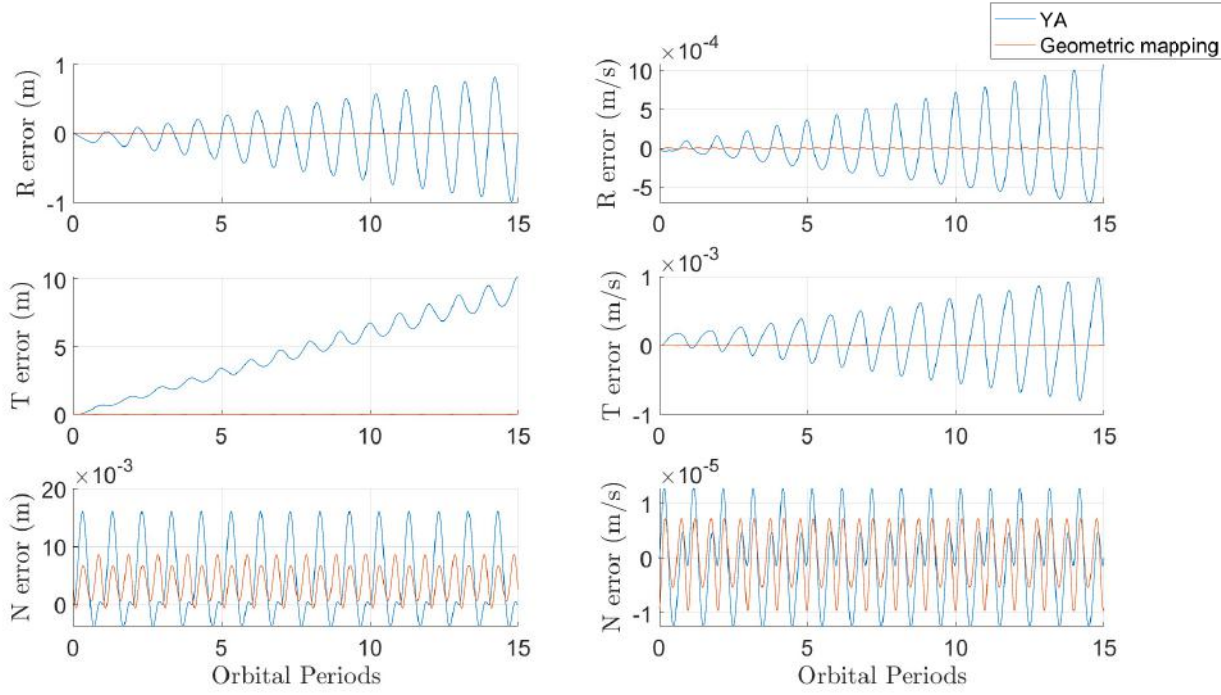


Figure 3.11: Relative RTN position and velocity error from YA solution (blue) and geometric linear mapping (orange).

### 3.2.i Difference in Semi-major Axis & Highly Eccentric Orbits

This analysis is repeated first by removing the energy matching condition. This means that the semi-major axis of the chief and deputy are no longer equal. As done in 2.1.d, an offset is introduced in the deputy semimajor axis of  $\delta a = 100$ m. Given this separation, we expect that the deputy will move slower than the chief, and so we should see a drift in the TR plane. Increasing the semi-major axis of the deputy leads to it falling behind, so the ellipse should trail to the left. The quasi-singular relative orbital parameters are:

$$a_0 \begin{bmatrix} \delta a \\ \delta \lambda \\ \delta e_x \\ \delta e_y \\ \delta i_x \\ \delta i_y \end{bmatrix} = \begin{bmatrix} 100 \\ 0 \\ -88.925 \\ -244.320 \\ 0 \\ 222 \end{bmatrix}$$

The leftward motion (growing relative distance) is confirmed in Figure 3.12.

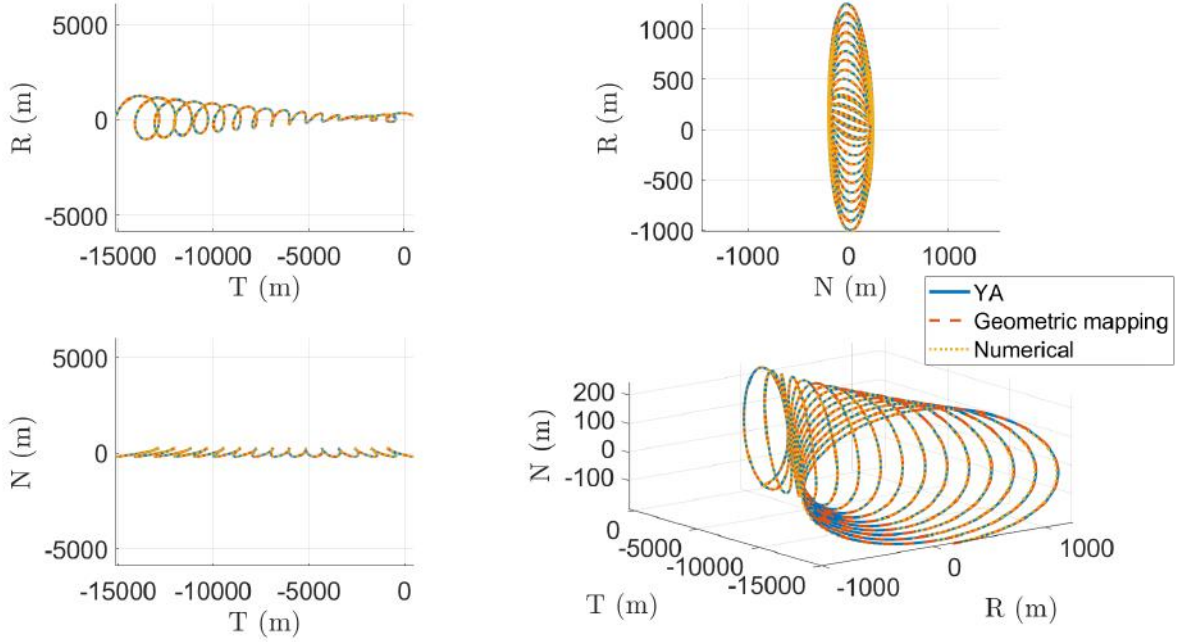


Figure 3.12: Relative RTN position from YA solution (blue), geometric linear mapping (orange), and numerical integration (yellow) for non-energy matched chief and deputy.

Next, we investigate the effects of large differences in semi-major axis by imposing  $\delta a = -10$  km. This allows us to both observe the effects of negative semi-major axis changes as well as the limit of the linear approximations of both YA and geometric mapping. As shown in Figure 3.13, both linear approximations diverge greatly from the nonlinear numerical integration over the course of 15 orbits. Thus, it can be concluded that neither the YA nor the geometric mapping solutions may be appropriate approximations for large initial relative separations.

$$a_0 \begin{bmatrix} \delta a \\ \delta \lambda \\ \delta e_x \\ \delta e_y \\ \delta i_x \\ \delta i_y \end{bmatrix} = \begin{bmatrix} -10000 \\ 0 \\ -88.925 \\ -244.320 \\ 0 \\ 222 \end{bmatrix}$$

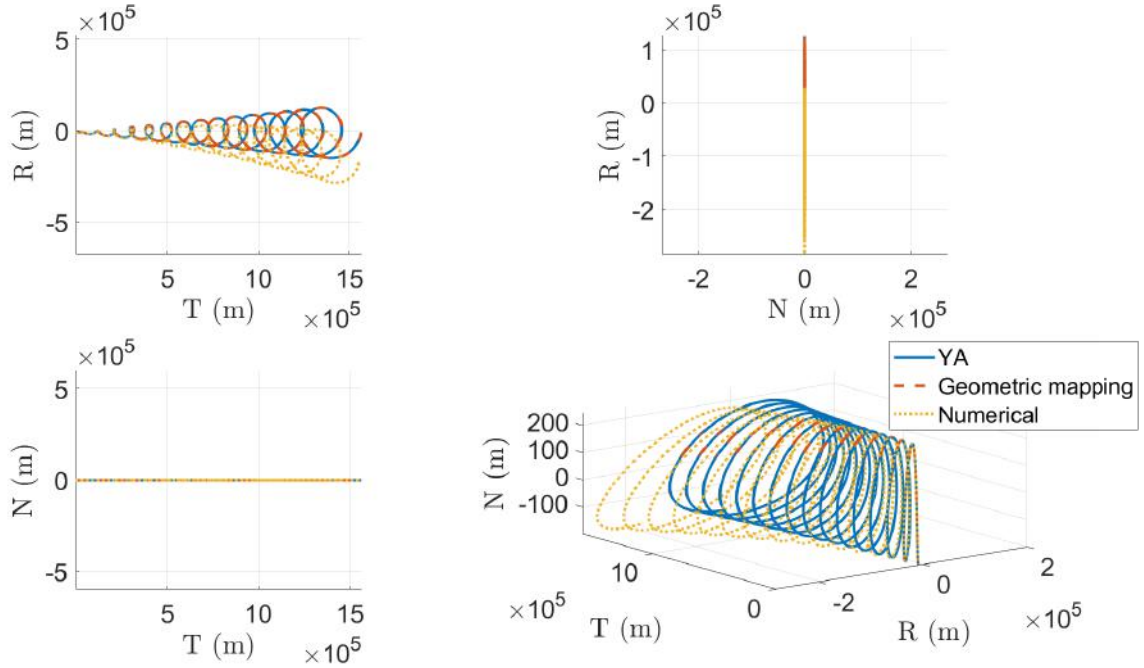


Figure 3.13: Relative RTN position from YA solution (blue), geometric linear mapping (orange), and numerical integration (yellow) for large initial relative separation.

Next, we look to investigate highly elliptic orbits. The relative semi-major axis is reset to 0, and here we select the chief orbit eccentricity to be  $e_0 = 0.6$ .

Though in theory we are only changing the eccentricity, the relative inclination vector also seems to change. This occurs because of the way the semi-major axis is calculated. The periapsis was taken to be equivalent to the semi-major axis in section 3.1 (the near-circular orbit case), and then the new semi-major axis was calculated from this and the desired eccentricity. Therefore, the relative inclination vector changes because it is normalized by the semi-major axis.

The results comparing the three relative motion solutions are shown in Figure 3.14. As expected, the shape of the relative position in RTN space deviates from the previous ellipse in the TR plane, but a safe relative orbit is still maintained by inspecting each of the orbit planes.

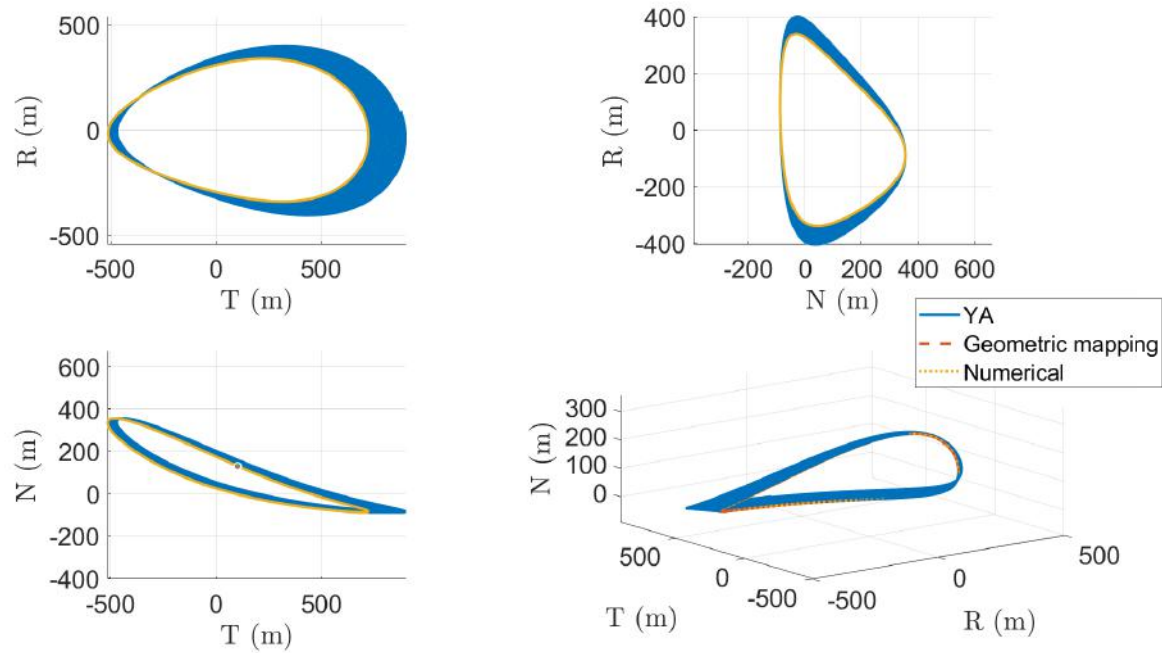


Figure 3.14: Analytically solved relative RTN position from YA solution (blue), geometric linear mapping (red), and numerical integration (yellow) for non-energy matched chief and deputy.

## 4 Problem Set 4

### 4.1 Problem 1: These are Relative Orbits!

#### 4.1.a Chief Osculating Initial Conditions

We select the same initial conditions for the chief as in Table 2.1.

#### 4.1.b Deputy Initial Conditions

As per the instructions, we set the quasi-non-singular relative orbital parameters to be (in terms of the chief semi-major axis):

$$a_c[\delta a, \delta\lambda, \delta e_x, \delta e_y, \delta i_x, \delta i_y] = [0, 100, 50, 100, 30, 200] \text{ m}$$

The singular orbital elements of TDX are therefore given in Table 4.1.

	$a$	$e$	$i$	$\Omega$	$\omega$	$M$
TDX	6892.927 km	$1.0823 \times 10^{-4}$	97.4400°	270.0017°	7.7033°	-7.7023°

Table 4.1: Initial osculating orbital parameters of deputy satellite TDX.

#### 4.1.c Numerical Integration of Unperturbed and J2-perturbed Propagation

Starting from the initial conditions, the orbits of the chief and deputy were each individually propagated by numerical integration as in 1.2.c and 1.2.d to obtain time-series histories of position and velocity. These quantities as measured in the Cartesian coordinate system and ECI frame were converted to the osculating singular orbital elements using the equations in 1.2.e. Since they are more numerically stable for circular orbits, we then convert the singular orbital elements to quasi-nonsingular ones for plotting.

To convert from osculating to mean orbital elements, we follow an iterative procedure as described in 3.4.1 of Alfriend [7]. We devise a Newton-Raphson algorithm that starts with a guess of the mean orbital elements, performs a transformation with equinoctial orbital elements (Appendix F in [7]) to calculate the osculating orbital elements from the mean quantities, and converts back to Keplerian orbital elements. The difference between the result and true osculating orbital elements is used to update the guess in the next iteration, and the process continues until convergence is met based on a tolerance of  $10^{-8}$  or after 100 maximum iterations. The initial guess of the mean orbital elements is set to be equal to the true osculating orbital elements.

#### Unperturbed Propagation

As the argument of latitude  $u$  is propagated unperturbed (from 0 to  $2\pi$ ), the osculating quasi-nonsingular absolute orbital elements of both the chief and deputy were computed to be practically constant with minor numerical errors. Periodicity in the motion is negligibly small. For both the chief in Figure 4.1 and deputy in Figure 4.2, the osculating and mean orbital elements align closely as expected in the absence of perturbations.

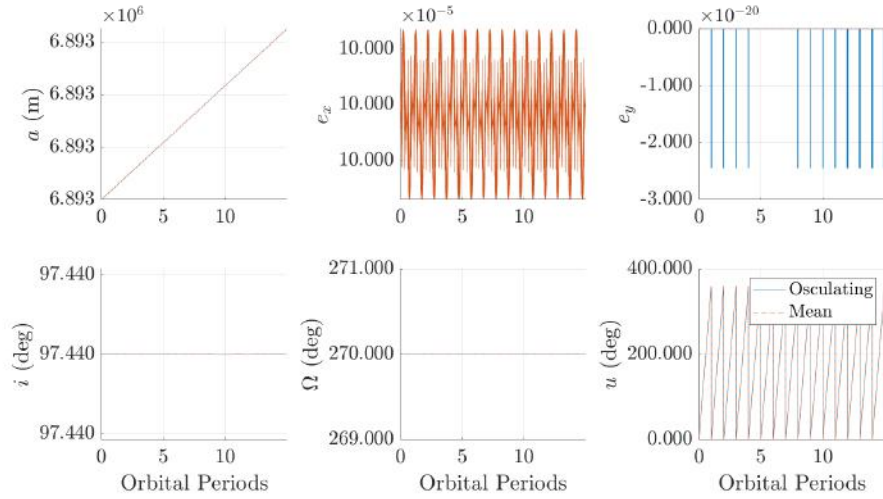


Figure 4.1: Unperturbed osculating (blue) and mean (orange) absolute orbital elements of the chief over 15 orbits.

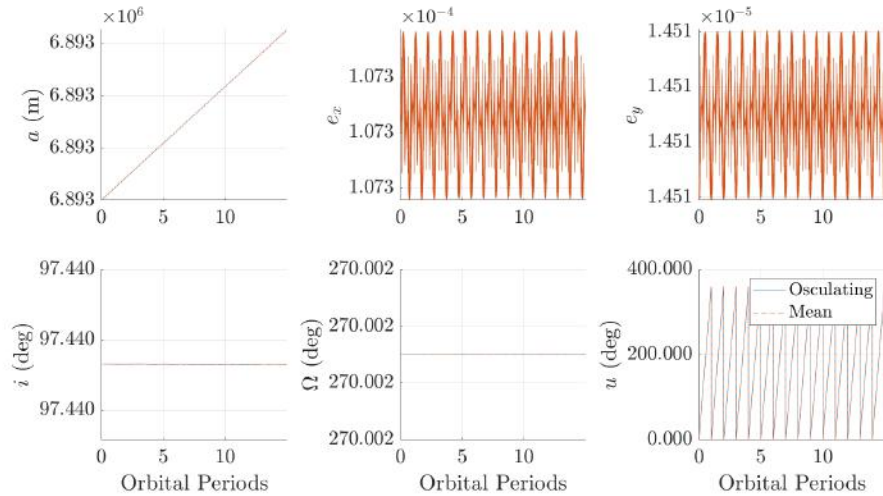


Figure 4.2: Unperturbed osculating (blue) and mean (orange) absolute orbital elements of the deputy over 15 orbits.

Plots of the relative orbital elements over time in Figure 4.3 reveal the negligibly small difference between the motion of the chief and deputy, as well as the alignment of the osculating and mean quantities in unperturbed propagation. As expected, there is some periodic motion of the mean argument of latitude that has a period equal to one orbit.

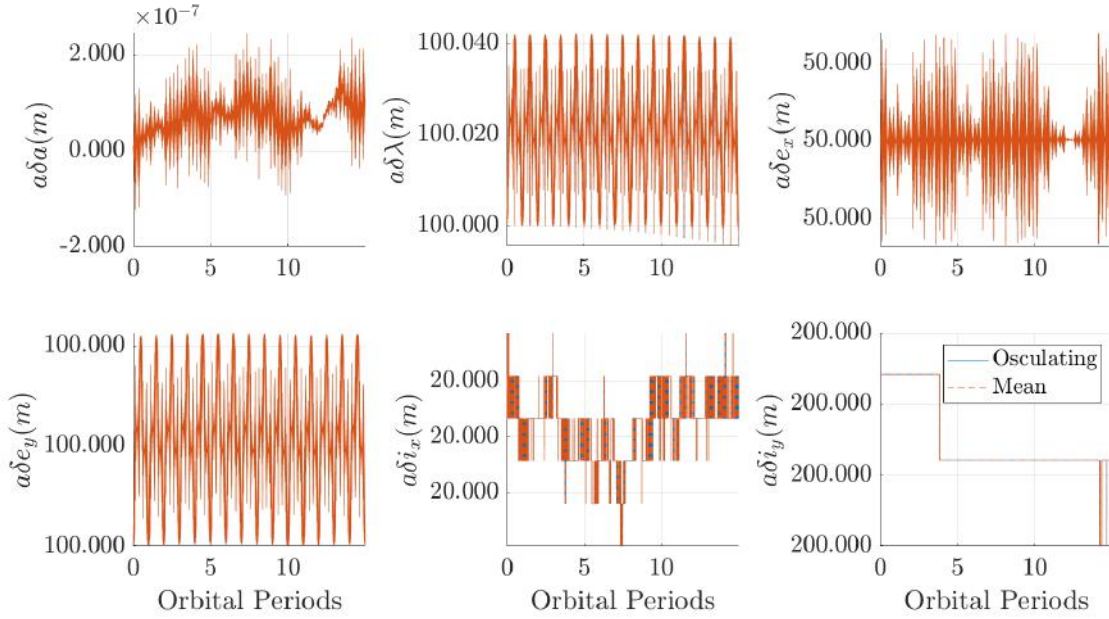


Figure 4.3: Unperturbed osculating (blue) and mean (orange) relative orbital elements.

## J2 Propagation

Considering the osculating orbital parameters plotted in Figure 4.4 and 4.5, the absolute orbital elements under J2 propagation exhibit notable periodicity in semi-major axis, eccentricity, inclination, and RAAN. In contrast to the unperturbed case, the magnitude of the periodicity is orders of magnitude larger. The mean orbital elements cut through the periodicity in semi-major axis, eccentricity, and inclination as they are defined. There is a clear drift in RAAN as expected under J2 effects captured in both osculating and mean quantities.

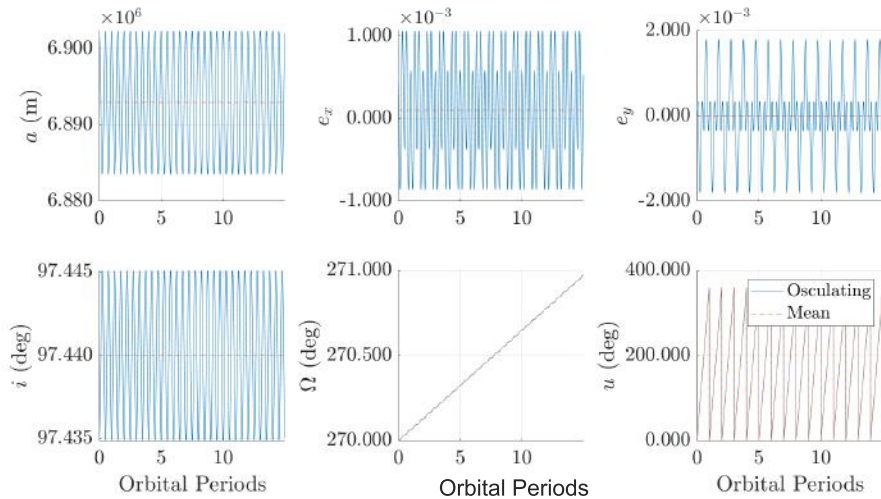


Figure 4.4: Perturbed osculating (blue) and mean (orange) absolute orbital elements of the chief over 15 orbits.

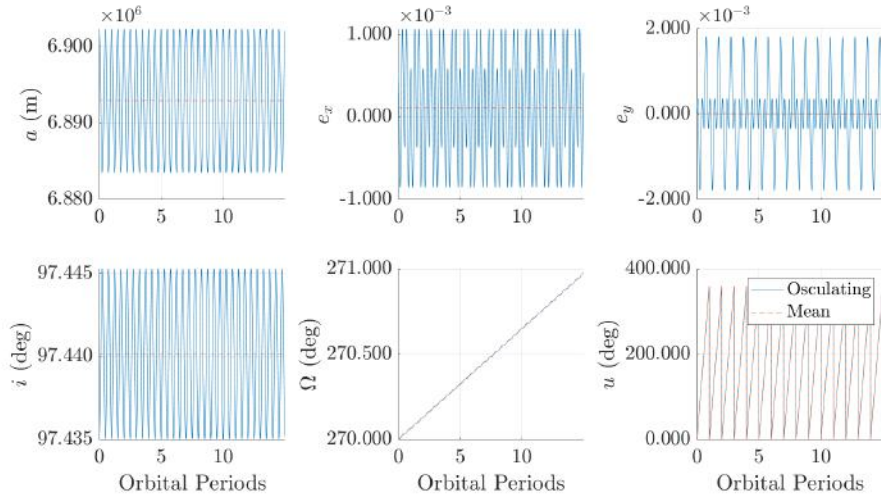


Figure 4.5: Perturbed osculating (blue) and mean (orange) absolute orbital elements of the deputy over 15 orbits.

Seen in Figure 4.6 are the relative orbital elements, which now all exhibit periodicity in the osculating case. We observe secular motion in the relative mean argument of latitude, eccentricity vector and inclination vector. Some of the periodic effects are removed by the mean orbital elements (particularly in the relative inclination), but most of the ROEs still display periodic motion in the mean quantities.

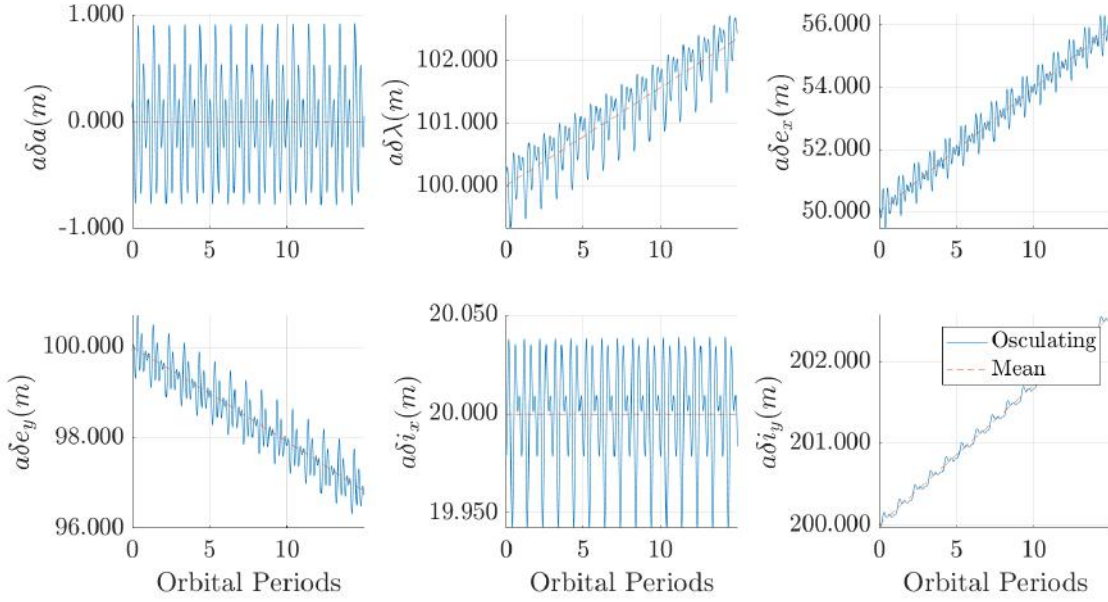


Figure 4.6: Perturbed osculating (blue) and mean (orange) relative orbital elements.

#### 4.1.d Relative Position in RTN for Unperturbed and J2-perturbed Propagation

For the unperturbed case, the RTN plots are shown as safe elliptical orbits (blue) in Figure 4.7. In the TR plane, the shape of the relative motion is a 2-by-1 ellipse as expected by theory. With the introduction of

J2 effects, we observe a drift only in the along-track direction corresponding to the precession of RAAN. J2 does not affect position in the radial or cross-track directions.

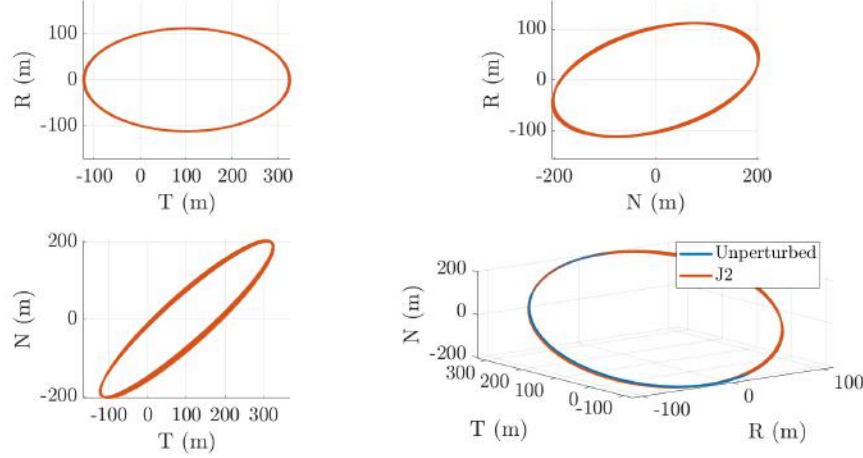


Figure 4.7: Relative position in RTN for unperturbed (blue) and J2 perturbed (orange) relative orbital elements.

#### 4.1.e Osculating and Mean Relative Orbital Elements

Next, we examine the unperturbed relative motion in state space plotted in Figure 4.8. For a near-circular orbit, the eccentricity vector plot typically forms a point at a distance  $\delta e$  from the origin with phase angle of eccentricity  $\phi$ . The inclination vector is a point at a horizontal distance  $\Delta i = 30$  m from the origin, matching the initial offset as defined in part b. Plotting the relative mean argument of latitude against relative semi-major axis yields a horizontal line at 0. This is also to be expected as the distance from this line to the x-axis is  $\delta a$ , which is zero by setting the energy matching condition.

In the J2-perturbed state space, the eccentricity vector plot maintains the same magnitude  $\delta e$  while the phase of relative eccentricity  $\phi$  changes over the propagation. Over a period of approximately 1000 orbits for sun-synchronous orbits, this produces a circle of radius  $\delta e$ . Figure 4.9 shows an arc formed by propagating over just 15 orbits. J2 drift is reflected in a changing  $\delta i_y$  while  $\delta i_x$  remains unaffected as can be seen by the formation of the vertical line in the inclination vector plot. Semi-major axis is not influenced by J2 effects and the plot remains on the x-axis as expected.

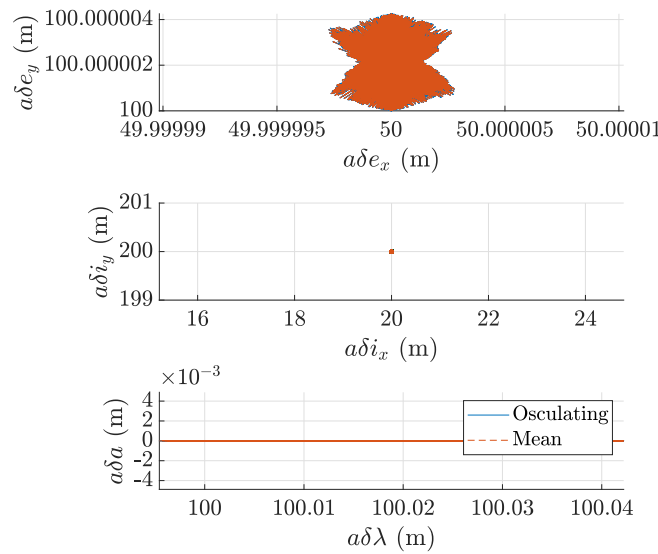


Figure 4.8: State space plots of unperturbed osculating (blue) and mean (orange) relative orbital elements..

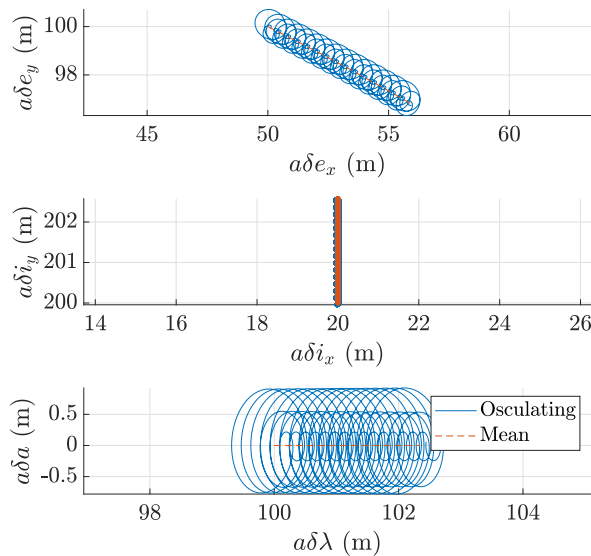


Figure 4.9: State-space for perturbed osculating (blue) and mean (orange) relative orbital elements.

#### 4.1.f Removing J2 Drift

A new set of initial conditions without J2 secular effects on the relative motion can be formed by eliminating differences in the relative inclination vectors. The following give the rate of change of the angle between the eccentricity vector and the  $\delta e_x$  axis, the inclination along  $\delta i_x$ , and the relative mean argument of latitude due to J2:

$$\frac{d\phi}{du} \Big|_{J2} = \frac{3}{2}\gamma(5\cos^2 i - 1) \quad (51)$$

$$\gamma = \frac{J_2}{2} \left( \frac{R_E}{a} \right)^2 \frac{1}{\eta^4} \quad (52)$$

$$\frac{d\delta i}{du} \Big|_{J2} = 3\gamma \sin^2(i)\delta i_x \quad (53)$$

$$\frac{d\delta\lambda}{du} \Big|_{J2} = -\frac{21}{2}(\gamma \sin(2i)\delta i_x + \frac{1}{7}\delta a) \quad (54)$$

It is immediately clear that we can easily eliminate drift in inclination and mean argument of latitude ( $\frac{d\delta i}{du} = \frac{d\delta\lambda}{du} = 0$ ) by designing zero relative inclination in  $x$  and zero relative semi-major axis ( $\delta i_x = \delta a = 0$ ). However, we can never create zero drift in eccentricity through modifying the relative orbital elements. The relative eccentricity will drift except for at a critical inclination of  $i_{crit} = \cos^{-1} \left( \sqrt{\frac{1}{5}} \right) = 63.43^\circ$ . Since the designed inclination of  $97.44^\circ$  is quite different from this, it is more practical to just remove the drift in the relative inclination and mean argument of latitude. From a mission design perspective, the benefits of a sun-synchronous orbit outweigh the need for active formation control for TanDEM-X, and so this inclination is acceptable.

Since energy matching already achieves  $\delta a = 0$ , a maneuver is needed to zero out the relative inclination along  $x$  that was initially set in 4.1.b:  $\Delta\delta i_x = -30$  m. From the definition of relative inclination in  $x$ , this may be attained by an inclination change of the deputy  $\Delta i_d = -30$  m. To find the location  $u_M$ , direction and magnitude of this maneuver, we turn to the GVE's. We follow a similar process as in 2.1.e to discretize the GVE's from Montenbruck et al. [11], and use the discrete equations to perform impulsive  $\Delta v$ . In general, an inclination change affects the orientation of the orbit, requiring an out-of-plane maneuver. Since the in-plane and out-of-plane elements are conveniently de-coupled, we only consider effects on the inclination and RAAN as given by

$$\Delta i = \frac{\cos u_M}{na} \Delta v_N \quad (55)$$

$$\Delta\Omega = \frac{\sin u_M}{na \sin i} \Delta v_N \quad (56)$$

In this case, it is optimal for the  $\delta v$  maneuver to have full effect on the inclination without changing the RAAN. The location of the maneuver is thus selected to be along the line of nodes. For simplicity, we choose to execute the plane change at the ascending node defined by  $u_M = 0^\circ$ . The magnitude of the maneuver is given by the appropriate GVE:

$$\Delta v_N = \frac{na}{\cos u_M} \Delta i_d = -0.0331 \text{ m/s}$$

#### 4.1.g Simulation without J2 Drift

The simulation is performed with identical initial conditions as before with the only change being zero inclination in the  $x$ -component. As observed by the resulting state space plots in Figure 4.10, the effect of J2 drift has disappeared as the inclination vector plot shows a point with constant  $\delta i_y = 200$  m.

The drift in eccentricity vector and equal semi-major axes remain unchanged from the previous set of initial conditions.

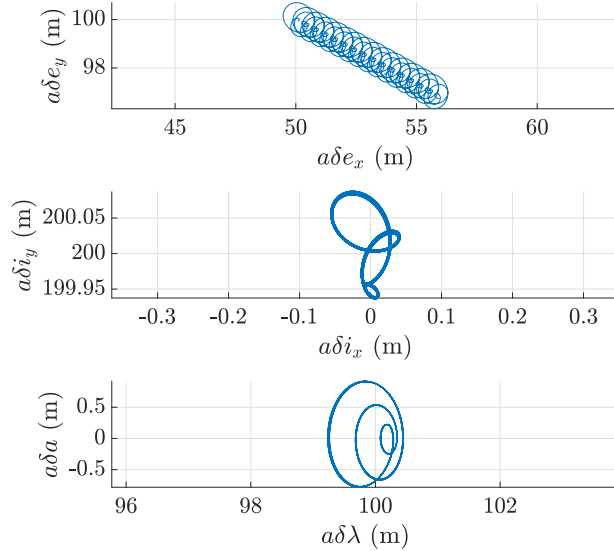


Figure 4.10: Relative orbital elements state space with J2 drift in inclination removed.

#### 4.1.h Linearized Analytical STM for J2 Effects

An STM for relative orbital elements including J2 perturbations as described in Koenig et al [12] was implemented. Derived from eccentricity and inclination vectors, this STM is valid for small separations and provides a direct mapping from the initial quasi-nonsingular relative orbital elements to the relative orbital elements at a certain time later. The STM was used to evolve the original initial conditions from 4.1.b and the no-drift initial conditions from 4.1.g.

The inclination vector and  $\delta\lambda$ - $\delta a$  state spaces produced by the J2 STM are consistent with the results of the numerical integration. For the original initial conditions, the J2 drift observed in  $\delta i_y$  in Figure 4.11 matches with the drift seen in Figure 4.9. With the no-drift initial conditions, the inclination vector state space is reduced to a single point in 4.12, corresponding to the same result in Figure 4.10. For both initial conditions, the relative semi-major axis is shown to be zero as before. In contrast to the numerically integrated solutions, it is observed that the eccentricity vector appears as a straight line instead of an arc, but this is to be expected in using a linearized STM.

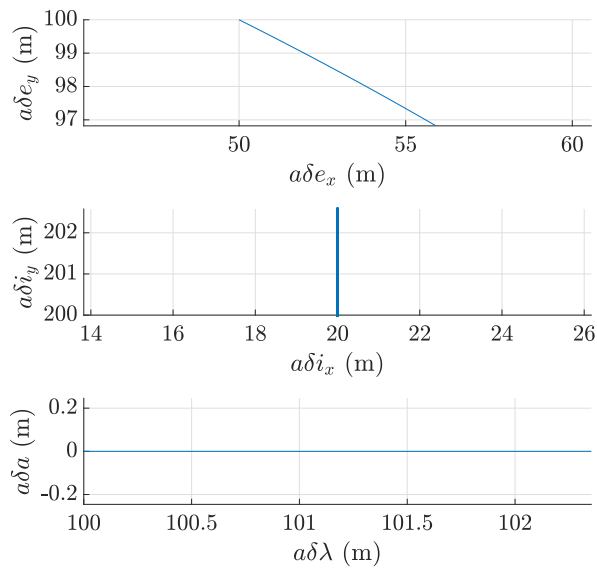


Figure 4.11: State space for the original initial conditions as propagated by the STM.

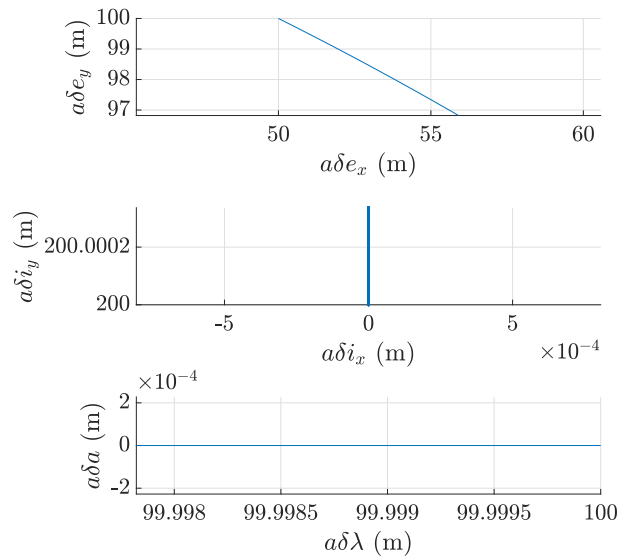


Figure 4.12: State space for the no-drift initial conditions as propagated by the STM.

## 5 Problem Set 5

### 5.1 Control Objectives

#### 5.1.a Formation Operational Modes

The relevant operational formations for this mission are established to achieve orbit maintenance and conduct SAR observation of the Earth. Various SAR formations are set by mission requirements for taking DEM measurements at different positions, defined by the height of ambiguity and latitude, in order to capture different geographic regions. These can be broadly characterized into five primary mission phases as summarized in Table 5.1 [8]. Mission phase E is characterized by a swap in the relative eccentricity vector, changing the formation phase by 180°. The final phase, separation of the satellites in RAAN, is for conducting super-resolution techniques and testing out new SAR modes.

Mission phase	$a\delta e$ [m]	$a\delta i$ [m]	$\theta - \varphi$	Days of mission	Notes
C1	260	222	200	103–179	Preliminary DEM generation with small baselines and large height of ambiguity
C2	297	260	210	180–300	(see above)
C3	297	371	210	301–399	(see above)
C4	350	350	180	399–465	High latitudes
D1	386	330	200	466–542	Final DEM generation with large baseline and small height of ambiguity
D2	440	385	210	543–663	(see above)
D3	440	550	210	664–762	(see above)
D4	500	500	180	763–828	High latitudes
E				829–839	Swap of relative eccentricity vector
F1	250	250	0	840–949	Crossing orbits, mountainous terrain
F2	250	600	0	950–982	(see above)
G1	250	1000	0	983–1015	Separation of satellites in right ascension of ascending node
G2	250	2000	0	1016–1048	(see above)
G3	250	4000	0	1049–1081	(see above)

Table 5.1: Formation parameters for key mission phases [8]

#### 5.1.b Definition of Operational Modes

To mitigate unwanted along-track drift and J2 effects on the relative inclination vector, nominal values of the relative semi-major axis  $\delta a$  and relative inclination component  $\delta i_x$  are set to be nearly zero. The nominal relative argument of latitude  $\delta \lambda$  is also initialized to zero and is limited by the maximum desired along-track separation between the satellites. Using the amplitude/phase definitions of eccentricity and inclination in Equation 22 and Equation 23, the quasi-nonsingular relative orbital elements are given in Table 5.2 for each of the mission phases.

Mission phase	$a\delta a$	$a\delta\lambda$	$a\delta e_x$	$a\delta e_y$	$a\delta i_x$	$a\delta i_y$
C1	0	0	-88.925	0	-244.320	222.000
C2	0	0	-148.500	0	-257.210	260.000

Table 5.2: Initial orbital elements for preliminary mission phases. All units in meters.

### 5.1.c Control Requirements

TSX and TDX will have identical orbit-keeping to the reference orbit and must stay within a 250m toroidal tube from the reference orbit [13]. The satellites are designed to execute orbit-keeping maneuvers simultaneously and with equal  $\Delta v$  to maintain relative formation [1].

While TSX is passive for relative formation-keeping, TDX is responsible for maneuvers to compensate for:

1. Variations in relative eccentricity due to J2 perturbations
2. Variations in relative argument of latitude due to differential drag and in-plane maneuver errors
3. Natural drift of the relative inclination vector

To maintain a “frozen” relative eccentricity vector, a daily along-track maneuver is required that is proportional to the eccentricity offset:

$$\left| \Delta v_T \right| = \frac{1}{2} v \left| \frac{d\Delta e}{dt} \cdot 1 day \right| = (3 \times 10^{-5}) a\delta e \quad (57)$$

For a preliminary eccentricity offset of  $a\delta e = 260$ m, a total along-track  $\Delta v$  of 0.78 cm/s split into two 0.39 cm/s maneuvers per day, each fired at half an orbital period apart, are required for orbit-keeping.

The mission is required to maintain an along-track control accuracy of 200m and a cross-track accuracy of 20m throughout. To limit the total number of maneuvers an offset between the relative eccentricity and inclination vectors of 30° is allowed [8].

Both satellites contain 74 kg of hydrazine fuel available for control maneuvers [14].

### 5.1.d Reconfiguration Requirements

Orbit reconfigurations are needed to change the baseline for SAR interferometry to capture different regions encompassing a global DEM. Reconfiguration maneuvers are executed by TDX and are to be performed safely given the close proximity between the satellites. As detailed in Table 5.1, reconfigurations between mission phases are to be completed in approximately one day or less.

### 5.1.e Control Actuators

Orbit-keeping is performed by both satellites using an identical propulsion system consisting of four 1-Newton hydrazine thrusters to execute out-of-plane maneuvers [15]. These thrusters are reported to produce a specific impulse of 220 sec [16].

In-plane formation-keeping maneuvers are conducted by the TDX satellite using two redundant pairs of nitrogen cold gas thrusters mounted parallel and anti-parallel to the flight direction. The cold gas thrusters provide low-thrust (40 mN) and high-specific impulse for fine control.

Given the relatively low  $\Delta v$  needed for reconfiguration and formation keeping, these can both be modeled using impulsive maneuvers.

### 5.1.f Dynamics Models

For the purposes of the assignment, two modes for preliminary DEM generation (phases C1 and C2) will be modeled. Orbit-keeping maneuvers and a reconfiguration maneuver from C1 to C2 will be implemented.

The dynamics models are split into one used to establish control and one to verify control performance.

#### Control determination dynamics

When trying to determine which control inputs to use, high-fidelity dynamics are not needed if we use orbital elements. This is because the orbital elements are slow-changing, and since control is determined “nearby”, a high-fidelity dynamics model will not provide a meaningful amount of additional information at extra computational cost. Therefore, a linear model such as an STM is preferred for computational efficiency. In this case, we choose to use the J2 STM with ROEs from section 4.1.h. Under this model, small separations are assumed for relative semi-major axis, eccentricity, and inclination, while arbitrarily large mean anomaly, argument of periapsis, and RAAN may be valid. The closed-form solution for the evolution of ROEs  $\delta\alpha$  is given by [12]:

$$\delta\alpha(t_i + \tau) = \Phi(\alpha_c(t_i), \gamma, \tau) \delta\alpha(t_i) \quad (58)$$

where the STM  $\Phi(\alpha_c(t_i), \gamma, \tau)$  is a function of the initial relative state, the set of parameters related to J2 perturbation  $\gamma$ , and time  $\tau$ .

With the initial relative separations defined for C1, the relative state at a given time can be obtained by pre-multiplying with the STM. The STM was used to propagate over 100 orbits, or equivalently  $\approx 160$  days, and plots of the state-space representation in Figure 5.1 display expected behavior under J2 effects. The eccentricity plot traces out an arc of a circle of radius  $\delta e$  and the inclination vector in the y-component exhibits a drift. The energy matching condition is verified by the relative semi-major axis–argument of latitude plot sitting on the x-axis.

The model is further verified by performing a linear mapping from the quasi-nonsingular orbital elements to relative position in the RTN frame [10]. In the TR and RN planes shown in Figure 5.2, we observe a safe ellipse with drifting in the along-track direction due to J2. The TR plane features a 2-by-1 ellipse as expected with semi-major axis  $2a\delta e$  and semi-minor axis  $a\delta e$ . The initial conditions were verified to be safe and reasonable for all mission phases.

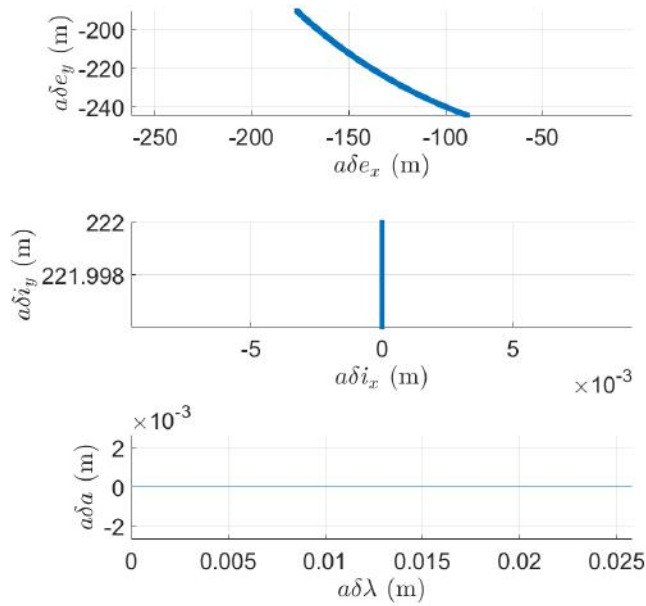


Figure 5.1: State space representation for C1 preliminary DEM formation over 100 orbits.

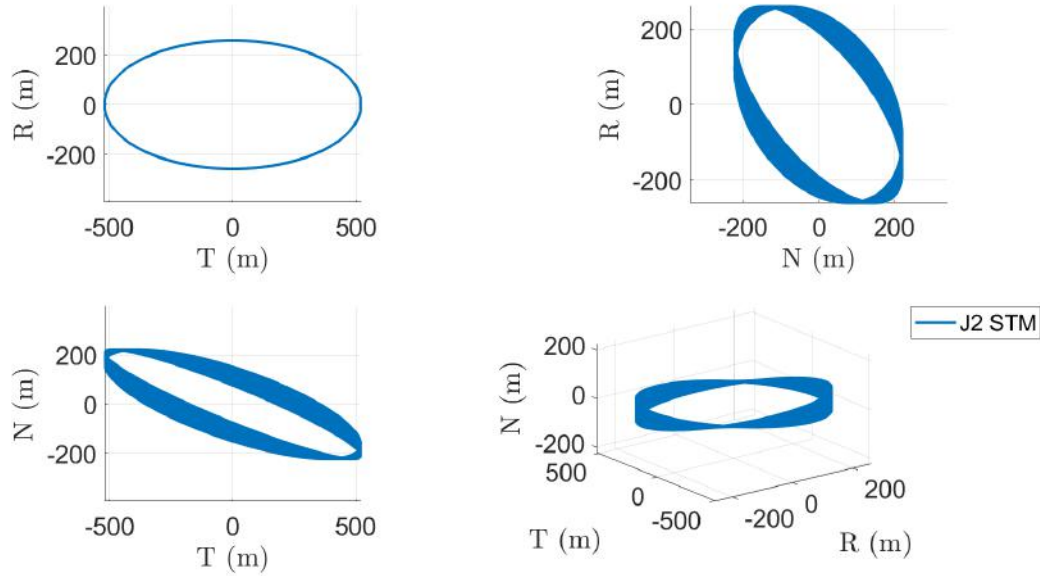


Figure 5.2: Relative position in the RTN frame for C1 preliminary DEM formation.

### Validation of control dynamics

For the purposes of validating orbit-keeping and control maneuvers at specific locations along the orbit, the absolute orbit of the chief and deputy will be propagated using the fundamental orbital differential equations with perturbations (Equation 5). This was built using *ode45* as done previously and verified

against the STM propagator without control input. The maneuvers will be pre-calculated using the J2 ROEs STM and applied as perturbations to the FODE. When applying these maneuvers, the  $\Delta v$ s are conveniently defined in the RTN frame and transformed into ECI using the theorem of Coriolis.

The relevant perturbations for satellites in low-Earth orbit include J2 geopotential and atmospheric drag. However, since the satellites are nearly identical in construction, they have nearly identical drag and ballistic properties, and thus variations in along-track separation is insignificant for control. Additionally, the baselines are small and attitude profiles of the spacecraft are quite similar, so we do not expect significant differences in drag to affect the relative orbit.

Third-body effects are considered minimal compared to drag and Earth's gravitational field, and thus the addition of these would not add significant fidelity to the model [11]. Moreover, since we are interested in the relative motion of the spacecraft and the baseline is small relative to the orbit, it is likely that the differences between these third-body effects on the two spacecraft would be negligible.

As the dominant effect in formation flying spacecraft in LEO, we choose to only model J2 perturbations. As a first run through in developing a control law, we wanted to ensure that we could maintain an orbit only under J2. For additional fidelity in future iterations, higher-order gravity could be added.

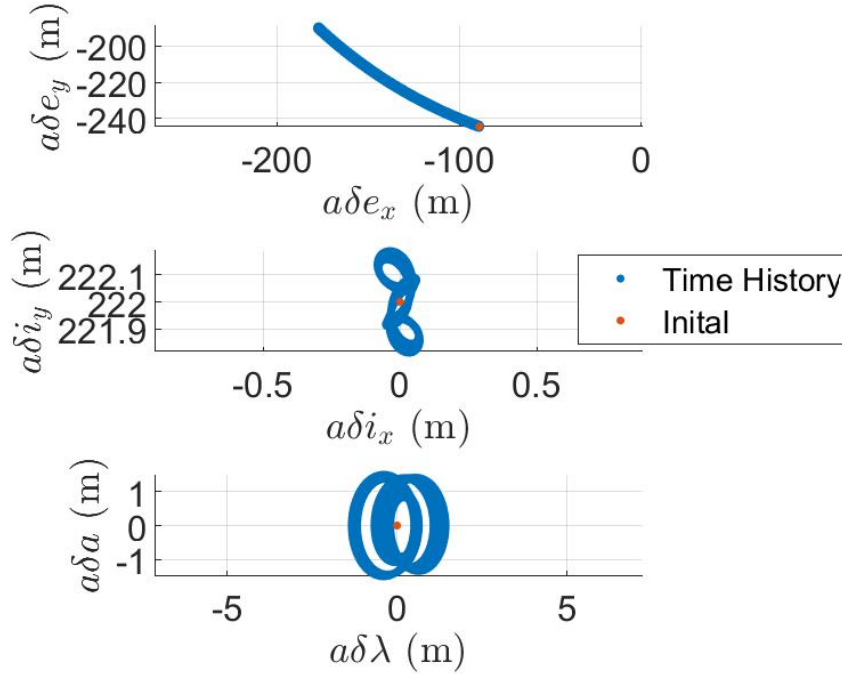


Figure 5.3: State space representation for preliminary DEM formation over 100 orbits numerically integrated with FODE.

The following sections describe the development of an impulsive control law for orbit-keeping and reconfiguration maneuvers. Actuators are implemented as impulsive as they can enable more fuel-efficient control strategies. For missions such as these in LEO, continuous thrust is typically avoided as their operation may conflict with science objectives and requires attitude maneuvering [9]. The impulsive control law was first established without model uncertainties in navigation or control in order to compare least-square

and double-impulsive methods in the ideal case.

## 5.2 Formation Reconfiguration

The first objective is to reconfigure the formation from mission stage C1 to C2. By the mission table, we are nominally allowed one day, and we want to consume as little fuel as possible to execute this reconfiguration. Two approaches are pursued to determine the maneuvers and their associated locations, which will be verified against the numerically integrated FODE. First, the Delta-V lower bounds are assessed to get a sense of proportionality. The reconfiguration corresponds to the following variations in quasi-nonsingular ROEs, where the goal is to change  $\delta e_x$ ,  $\delta e_y$ , and  $\delta i_y$ :

$$a\Delta\delta\vec{e} = [0, 0, -59.5748, -12.8895, 0, 38.0000] \text{ m}$$

### 5.2.a Delta-v Lower Bounds

The  $\Delta v$  lower bound is useful to establish guidelines for optimal control actions for a given reconfiguration. For arbitrary eccentricity, the minimum  $\Delta v$  required for the in-plane reconfiguration in eccentricity vector may be determined by [17]

$$\Delta v_{LB,ip} = na \frac{\Delta\delta e}{2\eta} \quad (59)$$

In this case, the in-plane lower bound is 0.0336 m/s. The out-of-plane  $\Delta v$  lower bound is given by [18]

$$\Delta v_{LB,oop} = \frac{an(1-e)}{\eta} \Delta\delta i \quad (60)$$

which comes out to 0.0419 m/s for this reconfiguration.

### 5.2.b Least-squares with maneuver placement

Two closed-form solutions are obtained using the least squares method to perform decoupled in-plane and out-of-plane maneuvers. The  $\Delta v$  needed for the reconfiguration is first pre-calculated by selecting optimal maneuver locations and solving the following linear system:

$$M_{[6 \times 3N]} \Delta v_{[3N \times 1]} = \Delta\delta\vec{e}_{[6 \times 1]}$$

where the  $\Delta\delta\vec{e}$  is the desired change in the ROEs, the  $M$  matrix contains the states and control inputs, and  $N$  is the number of maneuvers. Since the maneuver problem is decoupled, we define  $\Delta\delta\vec{e}_{ip}$  as the in-plane desired change and  $\Delta\delta\vec{e}_{oop}$  as the out-of-plane desired change for each problem separately. The  $M$  matrix is constructed as follows:

$$M = [\bar{\Phi}_{j,1}\Gamma_1, \bar{\Phi}_{j,2}\Gamma_2, \dots \bar{\Phi}_{j,N}\Gamma_N]$$

$$\bar{\Phi}_{j,1} = \begin{bmatrix} 1 & 0 & 0 & 0 & 0 & 0 \\ \frac{7\kappa EP + 3n}{2}\tau & 1 & 0 & 0 & -\kappa FS\tau & 0 \\ 0 & 0 & \cos(\dot{\omega}\tau) & -\sin(\dot{\omega}\tau) & 0 & 0 \\ 0 & 0 & 0 & 0 & 1 & 0 \\ \frac{7}{2}\kappa S\tau & 0 & 0 & 0 & 2\kappa T\tau & 1 \end{bmatrix}, \tau = \frac{\Delta u}{n + \kappa(\eta P + Q)}$$

$$\Gamma_1 = \frac{1}{na} \begin{bmatrix} 0 & 2 & 0 \\ -2 & 0 & 0 \\ \sin(u_k) & 2\cos(u_k) & 0 \\ -\cos(u_k) & 2\sin(u_k) & 0 \\ 0 & 0 & \cos(u_k) \\ 0 & 0 & \sin(u_k) \end{bmatrix}$$

To build the  $M$  matrix, we specify  $\Delta u$  (the change in the mean argument of latitude from the start of the maneuver sequence to the end of the sequence) and  $u_k$  (the location of the maneuver along the orbit). The optimal locations of the in-plane and out-of-plane maneuvers are equal to the phase of the desired reconfiguration [19]:

$$u_{ip} = \arctan\left(\frac{\Delta\delta e_y}{\Delta\delta e_x}\right) \quad (61)$$

$$u_{oop} = \arctan\left(\frac{\Delta\delta i_y}{\Delta\delta i_x}\right) \quad (62)$$

To execute the in-plane reconfiguration, we optimally use  $N=2$  burns spaced out by  $k\pi$  where  $k$  is chosen to be 1 [17]. The out-of-plane reconfiguration is achieved using a single burn.

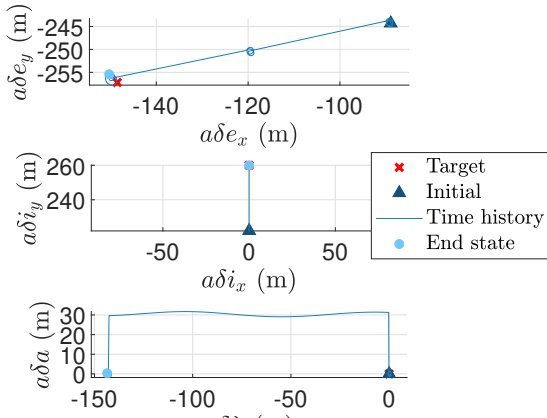
The optimal locations  $u_k$ ,  $\Delta u$ , and burns applied for the out-of-plane maneuver ( $\Delta v_1$ ) and in-plane maneuver sequence ( $\Delta v_2$  and  $\Delta v_3$ ) are given in Table 5.3. Note that the least-squares problem is solved twice: once for out-of-plane maneuvers and once for in-plane maneuvers.

Maneuver	$u_k$ (deg)	$\Delta u$ (deg)	$\Delta v_{RTN}$ (m/s)
$\Delta v_1$	90	90	[0, 0, +0.0419]
$\Delta v_2$	192.2	372.2	[-0.001, +0.0168, 0]
$\Delta v_3$	372.2	372.2	[+0.001, -0.0168, 0]

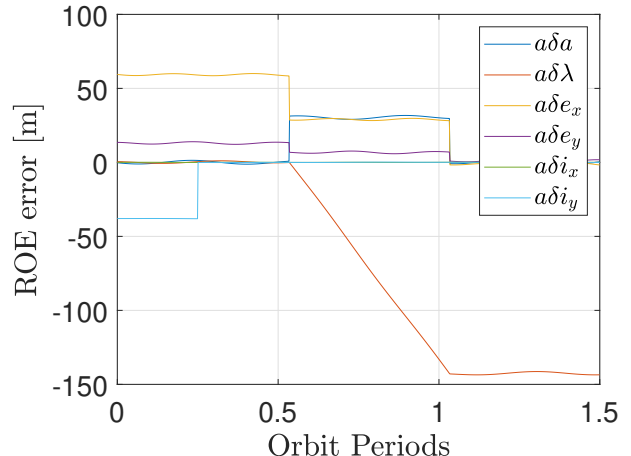
Table 5.3: Least-squares maneuver scheduling.

This sequence of maneuvers results in  $\Delta v = 0.0755$  m/s of total expended fuel for the combined out-of-plane and in-plane maneuvers.

The maneuvers are validated by numerically integrating the FODE and applying the maneuvers at the prescribed maneuver locations as the orbit is propagated. With a step size of 10 seconds and propagating over 1.5 orbits, the impulsive maneuver schedule given by the least squares solution brings the spacecraft towards the desired final target as shown in Figure 5.4a. The maneuvers result in a displacement of  $\delta\lambda$  because it is left uncontrolled in this case, producing the highest error in Figure 5.4b. It is noted that since the ROEs plotted are osculating quantities, the eccentricity vector begins to drift away from the target as the orbit is propagated past the completion of the maneuver. Table 5.4 shows the relative error between the desired target ROE and the ROE achieved in numerical propagation, where the largest error was observed in  $\delta e_x$ .



(a) State space



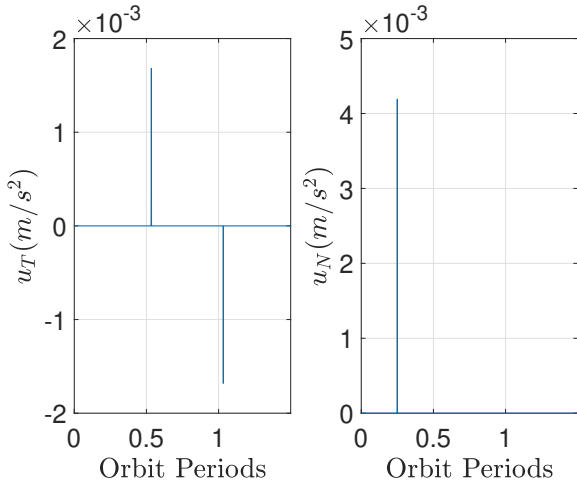
(b) Control error

Figure 5.4: Least-squares solution ROE state space and control error for the reconfiguration.

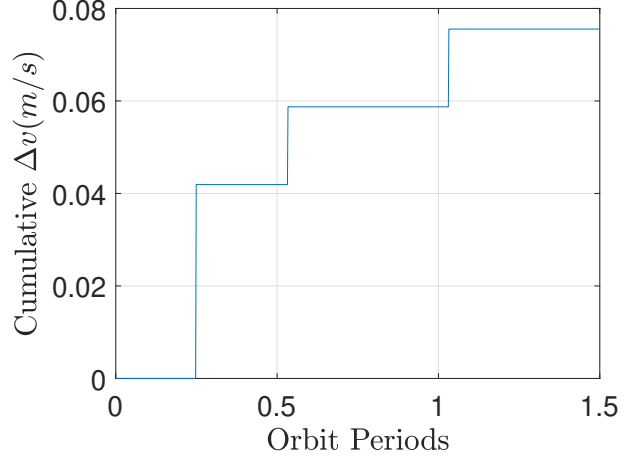
ROE	Desired ROE (m)	Achieved ROE (m)	Relative error
$\delta e_x$	-148.500	-150.256	1.18%
$\delta e_y$	-257.210	-255.434	0.69%
$\delta i_y$	260.000	259.945	0.02%

Table 5.4: Reconfiguration accuracy of least-squares solution.

The control actions in the along-track and cross-track directions are shown in Figure 5.5a. The least squares solution determined the magnitudes of the control actions to be  $\Delta v_{ip} = 0.0336$  m/s and  $\Delta v_{oop} = 0.0419$  m/s for a cumulative  $\Delta v$  of 0.0755 m/s as illustrated in Figure 5.5b. These both match the theoretical lower bounds calculated in the previous section, and thus indicate an optimal solution to the control problem.



(a) Control actions in T and N.

(b) Cumulative  $\Delta v$ .Figure 5.5: In-plane control actions and  $\Delta v$  over the reconfiguration for the least-squares solution.

### 5.2.c Double-impulse maneuver scheme

A closed-form relative orbit control strategy as introduced by D'Amico [9] is applied for the reconfiguration maneuver. Providing simple and deterministic feedback control, this strategy minimizes the number of pulses and decouples in-plane and out-of-plane maneuvers into single or double-impulse solutions. The in-plane double-impulse magnitudes and maneuver locations are related to the desired variations of ROEs after the maneuver, denoted by  $\delta a^{man}$  and  $\delta e^{man}$ , and the starting ROE state by the following:

$$\Delta v_{t,1} = \frac{na}{4} [(\delta a^{man} - \delta a) + ||\delta \vec{e}^{man} - \delta \vec{e}||] \quad (63)$$

$$\Delta v_{t,2} = \frac{na}{4} [(\delta a^{man} - \delta a) - ||\delta \vec{e}^{man} - \delta \vec{e}||] \quad (64)$$

$$u_{M,1} = \arctan \left( \frac{\delta e_y^{man} - \delta e_y}{\delta e_x^{man} - \delta e_x} \right) \quad (65)$$

$$u_{M,2} = \Delta u_M + u_{M,1} \quad (66)$$

The two burns are separated by a phase of  $\Delta u_M = \pi$  as this produces the minimum  $\Delta v$  cost derived from the GVE. Note that in this case, we are setting a set of desired ROEs that are exactly the same as the set of C2 except for  $\delta a^{man}$ , which is the desired value after the maneuver used to correct the variation in  $\delta \lambda$ . This is determined by accounting for the variation in  $\delta u$  due to dominant J2 effects during the maneuver cycle by [9]:

$$\delta u_{J2} = -12\gamma \sin(2i) \delta i_x n \Delta t \quad (67)$$

$$\delta a^{man} \approx -\frac{\pi}{2n\Delta t - \pi} \left[ 3\delta e^{max} + \delta a - \frac{4}{3\pi} (\delta u - \delta u^{nom} + \delta u_{J2}) \right] \quad (68)$$

The parameter to be tuned here is  $\Delta t$ , which is the time between the last burn in this maneuver and the first burn in the next maneuver. The assumption in this setup is that we will never be able to completely get rid of the  $\delta \lambda$  drift, and so  $\delta \lambda$  is allowed to drift but by known amounts to be corrected on a regular schedule. In this case, there is no obvious choice for the time until the next maneuver since we do not have any more planned maneuvers after that. For this simulation, we set  $\Delta t = 3T$ .

To reconfigure from phase C1 to C2, a single in-plane and a single out-of-plane maneuver are executed with the maneuver schedule and magnitudes given in Table 5.5.

Maneuver	$u_k$ (deg)	$\Delta v_{RTN}$ (m/s)
$\Delta v_1$	90	[0, 0, 0.0419]
$\Delta v_2$	191.8352	[0, +0.0146, 0]
$\Delta v_3$	371.8352	[0, -0.0192, 0]

Table 5.5: Closed-form solution maneuver scheduling.

The maneuvers in Figure 5.7 are reflected in shifts in the relative orbital elements in Figure 5.6, most notably in eccentricity and inclination. We see that  $\delta \lambda$  drifts to return to 0 separation across 1.5 orbits. When left to propagate for longer,  $\delta \lambda$  is observed to continue drifting beyond 0 separation as expected. Over longer orbit simulations, this behavior would be cycled after applying another maneuver as previously discussed.

Table 5.6 shows the relative error between the desired target ROE and the ROE achieved in numerical propagation.

ROE	Desired ROE (m)	Achieved ROE (m)	Relative error
$\delta e_x$	-148.500	-150.8192	1.56%
$\delta e_y$	-257.210	-255.0226	0.85%
$\delta i_y$	260.000	259.9553	0.02%

Table 5.6: Reconfiguration accuracy of double-impulse solution.

The closed-form solution determined the magnitudes to be  $\Delta v_{ip} = 0.0339$  m/s and  $\Delta v_{oop} = 0.0419$  m/s.

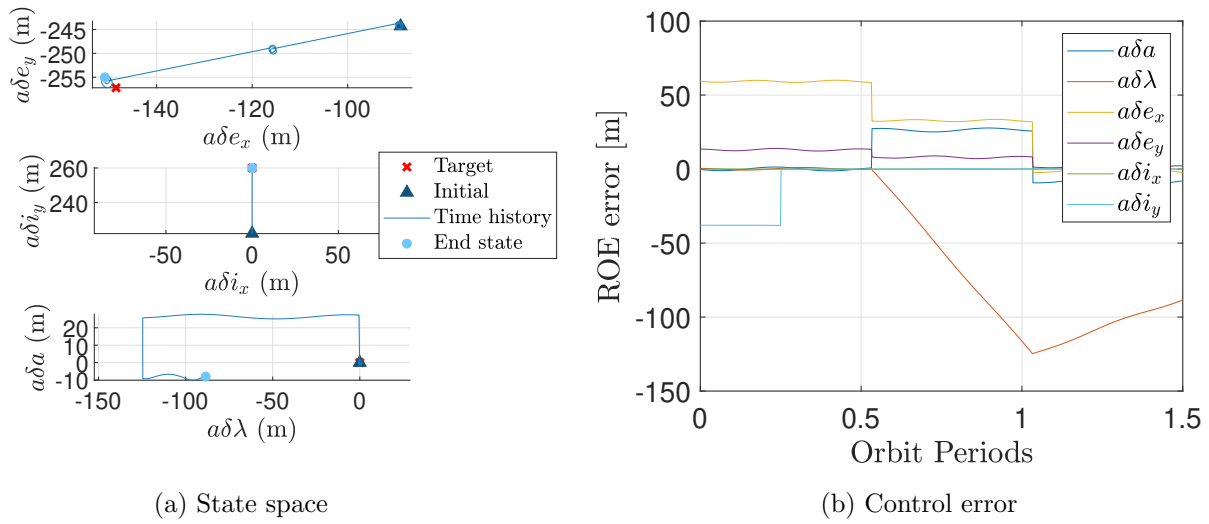


Figure 5.6: Double-impulse solution ROE state space and control error for the reconfiguration.

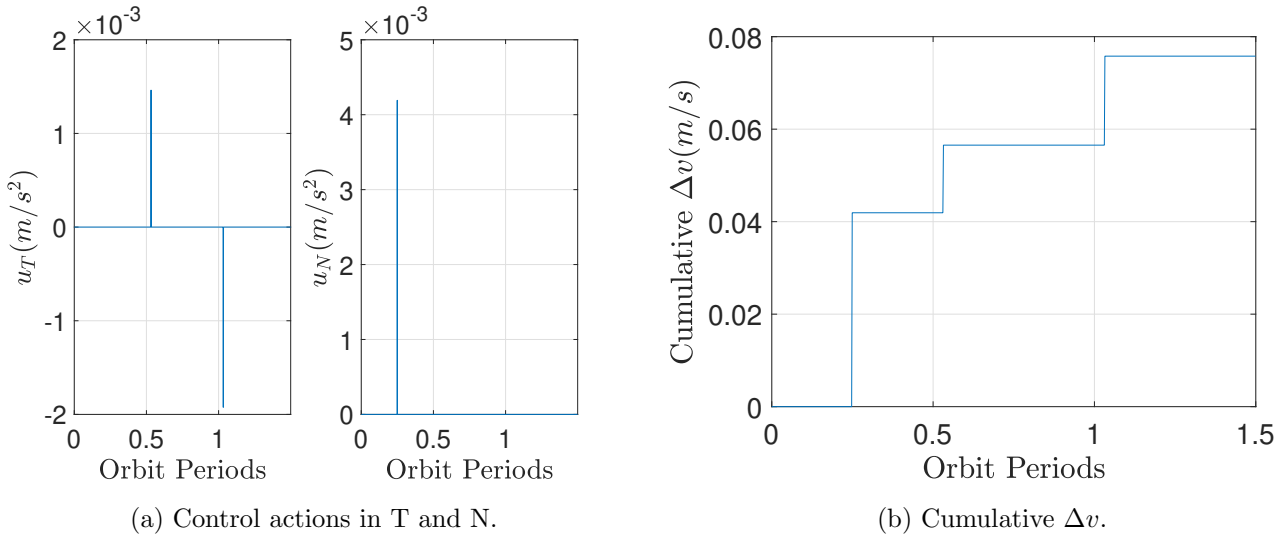


Figure 5.7: In-plane control actions and  $\Delta v$  over the reconfiguration for the double-impulse solution.

### 5.2.d Comparison of approaches

In general, one advantage of using the least squares approach is that it makes use of a linear STM to compute control actions. However, this method requires *a priori* knowledge of the times and locations of each maneuver, which may not be always be appropriate for some mission cases. Moreover, the iterative solver is an approximation that may not always converge.

The double-impulse closed-form strategy is deterministic and in general, utilizes a minimal number of burns. As with least squares, the maneuver locations and times must be predefined. The main drawback of this method is that the maneuvers induce a variation in  $\delta\lambda$ , which may grow to be excessively large for large reconfigurations.

Both the least squares and double-impulse closed-form implementations have roughly the same  $\Delta v$  magnitude as the lower bound predicted by [19]. Least squares performed with marginal improvements in relative ROE error of less than 1%. The total  $\Delta v$  expended using the double-impulse method amounted to 0.25 mm/s more than the optimal lower bound. The main advantage of double-impulse over the least squares solution is in its ability to regulate  $\delta\lambda$ . The price for this is a negligibly small difference for this propulsion system, and the correction in  $\delta\lambda$  is something we cannot achieve using the least-squares solution as-is.

## 5.3 Formation Keeping

The objective of formation keeping is to maintain the relative formation of the spacecraft. This is defined by the nominal ROEs of mission phase C1 and the maximum allowed deviations by mission requirements. The maneuvers are computed in the loop in this implementation. At each time step, the ROEs are assessed and if any violate its maximum limit, a maneuver is performed with magnitude and direction calculated using the closed-form solution. The maneuvers are stored within a buffer and run when appropriate using FODE. For all modeled configurations, the relative semi-major axis is set to zero. Since J2 does not produce any secular effects in the semi-major axis, it is not critical to enforce a control window on this parameter. We choose an inclination phase angle of  $\theta = 90^\circ$ , and therefore no drift in  $\delta\lambda$  or  $\delta i$  is expected. Therefore, a control window on eccentricity may be sufficient for formation-keeping. The following control window is selected for this phase based on TanDEM-X mission requirements:

$$\begin{aligned}\delta\psi_{max} &= 30^\circ \\ \delta e_{max} &= ||\delta\bar{e}^{nom} - \delta\bar{e}^{nom} \cos(\delta\psi_{max})|| = 34.8334 \text{ m}\end{aligned}$$

Once any of these bounds are reached, a maneuver will be executed. This requires formulating the desired ROEs after the maneuver. Though at this time we only expect to need to reconfigure for eccentricity, in case we would like to model higher-order gravity terms or drag in the future that could cause drifts in the inclination vector we also include how to perform out-of-plane formation keeping. For eccentricity and inclination, this is given by [9]:

$$\begin{aligned}\delta e^{man} &= \begin{bmatrix} \delta e_x^{nom} \cos(\delta\phi) - \delta e_y^{nom} \sin(\delta\phi) \\ \delta e_x^{nom} \sin(\delta\phi) + \delta e_y^{nom} \cos(\delta\phi) \end{bmatrix} \\ \delta i^{man} &= \begin{bmatrix} \delta i_x^{nom} \\ \delta i_y^{nom} - \text{sign}(\delta i_x)\delta i^{max} \end{bmatrix}\end{aligned}$$

where the following auxiliary quantities are defined as:

$$\delta\phi \approx \text{sign}(\phi') \arcsin(\delta e^{max}/\delta e^{nom})$$

$$\phi' = \frac{3}{2}\gamma(5\cos^2(i) - 1)$$

$$\gamma = \frac{J_2}{2} \left(\frac{R_E}{a}\right)^2 \frac{1}{\eta^4}$$

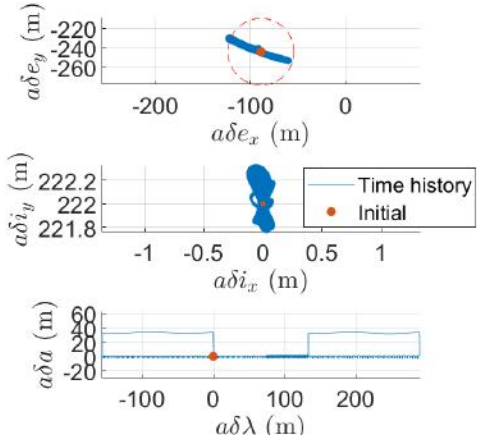
The variation in  $\delta\lambda$  is regulated through controlling  $\delta a^{man}$  as previously described in 5.2.c. In this case, given how spread out the maneuvers are, we use  $\delta t = 35T$ .

### 5.3.a Results and Discussion

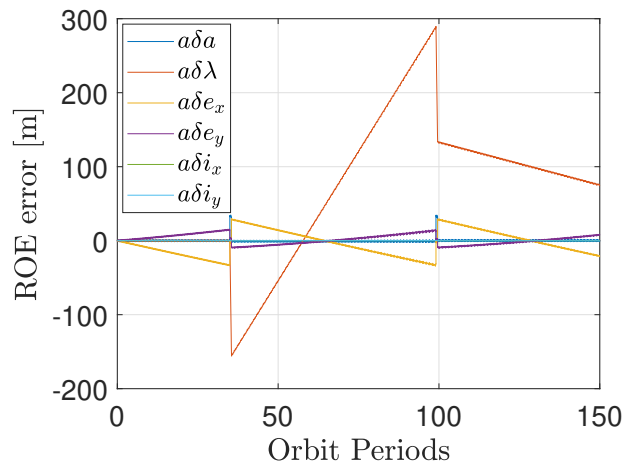
We follow the same approach as in 5.2.c to find the required  $\Delta v$  and locations for the three burns in this maneuver. These values are placed in a buffer and applied at the appropriate simulation time. With this solution, we found that over the course of 150 orbits, only two maneuvers (6 burns) are needed. This implies that the spacecraft drifts out of the eccentricity control bounds approximately once every 50 orbits.

The results of the formation keeping are shown in Figure 5.8a. We see that the eccentricity vector is maintained within the control window shown in dashed red circle. We also see in Figure 5.8b that  $\delta\lambda$  is being controlled as it goes back and forth using the natural motion to reduce the control effort.

Over the 150 orbits (roughly 10 days), we expend  $\Delta v_{ip} = 0.0738 \text{ m/s}$  on in-plane formation keeping and  $\Delta v_{oop} = 1.3132 \times 10^{-4} \text{ m/s}$  on out-of-plane formation keeping for a total of  $0.0739 \text{ m/s}$ .

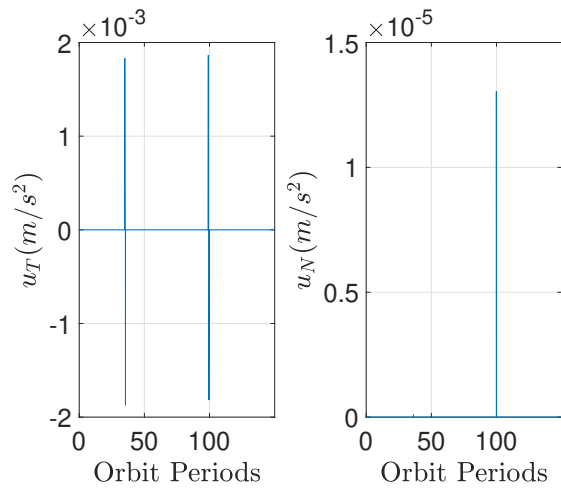


(a) State space

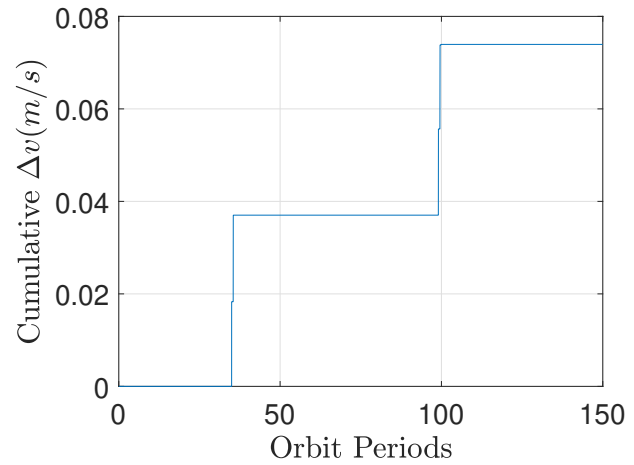


(b) Control error

Figure 5.8: Double-impulse solution ROE state space and control error for formation keeping.



(a) Control actions in T and N.

(b) Cumulative  $\Delta v$ .Figure 5.9: In-plane control actions and  $\Delta v$  over the formation keeping for the double-impulse solution.

## 6 Problem Set 6

### 6.1 Problem 1: Continuous Control Law

This section describes the implementation of a continuous control scheme to reconfigure the formation-flying spacecraft from C1 to C2 as given in Table 5.1. The reconfiguration corresponds to the following variations in quasi-nonsingular ROEs:

$$a\Delta\delta\vec{e} = [0, 0, -59.5748, -12.8895, 0, 38.0000] \text{ m}$$

#### 6.1.a Formation Reconfiguration Initial Conditions

We begin with the following initial conditions for the absolute chief orbit, with initial ROEs defined for mission phase C1.

	$a$	$e$	$i$	$\Omega$	$\omega$	$M$
TSX	6892.927 km	$1 \times 10^{-4}$	97.44°	270°	0°	0°

Table 6.1: Initial osculating orbital parameters of chief satellite TSX for mission phase C1.

The duration of the simulation is set to 15 orbits, or approximately 1 day at the orbit of the chief as allotted for the reconfiguration maneuver.

#### 6.1.b Unconstrained Lyapunov Control Implementation

Lyapunov control theory is applied using a linear relative dynamics model [20]. This implementation takes after a reduced model in which the state vector includes all quasi-nonsingular ROEs except  $\delta\lambda$ , given by

$$\delta\dot{\alpha} = A_c\delta\alpha + B_c u \quad (69)$$

$$\delta\alpha = [\delta a, \delta e_x, \delta e_y, \delta i_x, \delta i_y]^T \quad (70)$$

The 5-by-5 plant matrix  $A_c$  accounts for Keplerian dynamics and J2 perturbations, and  $B_c$  represents the control input matrix. It is not necessary to include drag in this model, as the spacecraft are nearly identical and the baselines are short. Therefore, differential drag is not expected to be significant.

$$A_c = \kappa \begin{bmatrix} 0 & 0 & 0 & 0 & 0 \\ \frac{7}{2}e_y Q & -(4e_c e_y G + C)Q & -(1 + 4e_y^2 G - D)Q & 5e_y S & 0 \\ -\frac{7}{2}e_x Q & (1 + 4e_x^2 G - D)Q & (4e_c e_y G - C)Q & 5e_x S & 0 \\ 0 & 0 & 0 & 0 & 0 \\ \frac{7}{2}S & -4e_c GS & -4e_y GS & 2T & 0 \end{bmatrix} \quad (71)$$

$$B_c = \frac{1}{a_c n_c} \begin{bmatrix} \frac{2}{\eta_c} (1 + e_c \cos f_c) & 0 \\ \eta_c \frac{(2 + e_c \cos f_c) \cos(\omega_c + f_c) + e_x}{1 + e_c \cos f_c} & \frac{\eta_c e_y}{\tan i_c} \frac{\sin(\omega_c + f_c)}{1 + e_c \cos f_c} \\ \eta_c \frac{(2 + e_c \cos f_c) \sin(\omega_c + f_c) + e_y}{1 + e_c \cos f_c} & \frac{-\eta_c e_x}{\tan i_c} \frac{\sin(\omega_c + f_c)}{1 + e_c \cos f_c} \\ 0 & \eta_c \frac{\cos(\omega_c + f_c)}{1 + e_c \cos f_c} \\ 0 & \eta_c \frac{\sin(\omega_c + f_c)}{1 + e_c \cos f_c} \end{bmatrix} \quad (72)$$

We additionally define the following auxiliary variables for  $A_c$ :

$$\begin{aligned}\gamma &= \frac{3}{4}J_2R_e^2\sqrt{\mu}, \quad \eta_c = \sqrt{1 - e_c^2}, \quad \kappa = \frac{\gamma}{a_c^{7/2}\eta_c^4}, \quad e_x = e_c = \cos\omega_c, \quad e_y = e_c \sin\omega_c \\ C &= \sin\omega_c, \quad D = \cos\omega_c, \quad G = \frac{1}{\eta_c}, \quad Q = 5\cos^2 i_c - 1, \quad S = \sin(2i_c), \quad T = \sin^2 i_c\end{aligned}$$

The set of control accelerations for the reconfiguration is defined in  $u$  as components in the RTN frame. The control law is

$$u = -B_c^+ [A_c \Delta\delta\alpha + P \Delta\delta\alpha] \quad (73)$$

$B_c^+$  indicates the Moore-Penrose pseudoinverse of matrix  $B$ . The controller is parameterized by  $N$  and  $k$ . Larger values of  $N$  correspond to a sharper control acceleration approaching an impulse. Thus, the higher this value, the higher the propulsion efficiency. The parameter  $k$  represents as an arbitrarily large scalar that adjusts the magnitude of the gain matrix [20]. The controller feedback gain  $P$  is a positive-definite matrix defined as

$$P = \frac{1}{k} \begin{bmatrix} \cos(\phi - \bar{\phi}_{ip})^N & 0 & 0 & 0 & 0 \\ 0 & \cos(\phi - \bar{\phi}_{ip})^N & 0 & 0 & 0 \\ 0 & 0 & \cos(\phi - \bar{\phi}_{ip})^N & 0 & 0 \\ 0 & 0 & 0 & \cos(\phi - \bar{\phi}_{oop})^N & 0 \\ 0 & 0 & 0 & 0 & \cos(\phi - \bar{\phi}_{oop})^N \end{bmatrix} \quad (74)$$

where the optimal mean argument of latitude for in-plane and out-of-plane maneuvers have closed form solutions for near-circular orbits [20].

$$\bar{\phi}_{ip} = \text{atan2}\left(\frac{\Delta\delta e_y}{\Delta\delta e_x}\right) \quad (75)$$

$$\bar{\phi}_{oop} = \text{atan2}\left(\frac{\Delta\delta i_y}{\Delta\delta i_x}\right) \quad (76)$$

At each time step, these optimal locations are updated based on the arithmetic differences  $\Delta\delta e$  and  $\Delta\delta i$  between the current state and the applied reference state. The plant and control input matrices are functions of the current orbital parameters. The tracking error  $\Delta\delta a$  is defined by the difference between the current and the applied reference state, i.e.  $\Delta\delta\alpha = \delta\alpha - \delta\alpha_a$ . These quantities inform the control law, which then is applied as input to the FODE numerical integrator as perturbing accelerations to propagate the orbit for the next time step. Lastly, the state is updated in terms of the mean orbital elements, smoothing over the periodicity in osculating elements for computing control actions. The numerical integrator was verified with results using the same initial conditions as performed in previous problem sets without control input, and was observed to exhibit J2 drift as expected.

At this stage, the system is modeled perfectly noise-free. However, as the model is further developed, uncertainty may be incorporated as zero-mean Gaussian noise in the control input  $u$  (noisy actuators) as well as in the state vector (noisy sensors).

### 6.1.c Continuous Control Lower Bound

To get a sense of how well the Lyapunov controller is performing, the theoretical  $\Delta v$  lower bound for the overall reconfiguration is calculated as in [17]:

$$\Delta v_{LB,ip} = a_c n_c \frac{\|\Delta \delta \mathbf{e}\|}{2\eta_c} = 0.0336 \text{ m/s} \quad (77)$$

$$\Delta v_{LB,oop} = a_c n_c \frac{1 - e_c}{\eta_c} \|\Delta \delta \mathbf{i}\| = 0.0419 \text{ m/s} \quad (78)$$

### 6.1.d Unconstrained Controller Results & Discussion

A value of  $N = 14$  is selected for the unconstrained Lyapunov controller as done in Steindorf [20]. The feedback gain parameter is set to  $k = 3000$ .

With the unconstrained Lyapunov controller, the control actions taken in the along-track (T) and cross-track (N) directions are executed at the regularly occurring optimal locations as shown in Figure 6.1a. The applied thrusts decrease in magnitude over time as the controller approaches its destination and the total  $\Delta v$  over the reconfiguration is approximately 0.0755 m/s as depicted in Figure 6.1b. The in-plane and out-of-plane  $\Delta v$  performed were computed to be 0.0337 m/s and 0.0418 m/s respectively, which are practically equivalent to the theoretical bound (with marginal numerical error). The total cumulative  $\Delta v$  is equal to the theoretical lower bound, demonstrating that the continuous controller implemented is optimal.

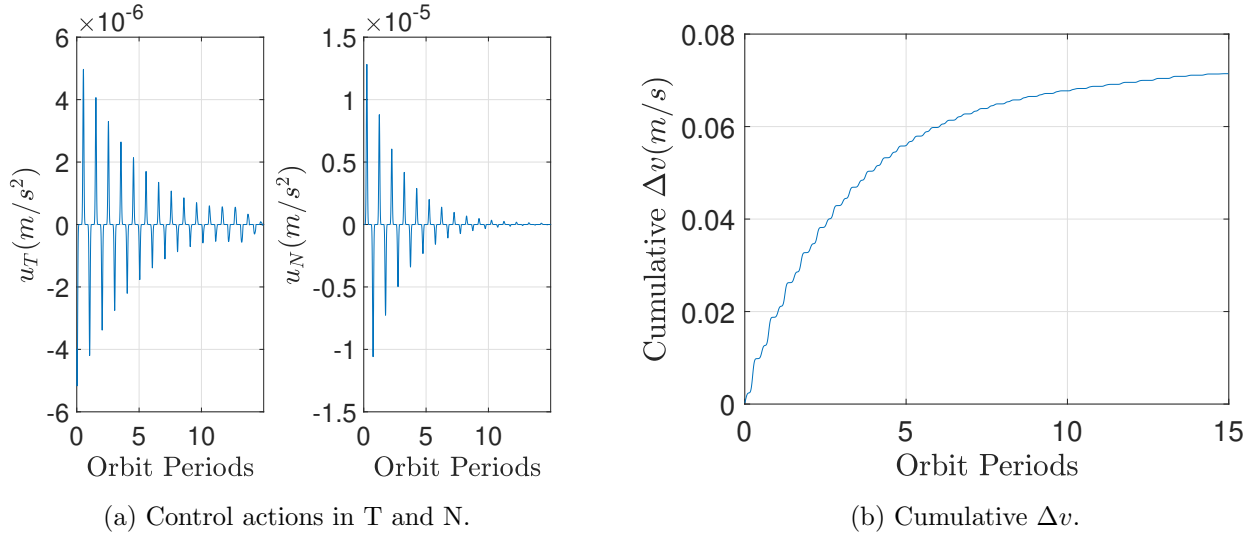


Figure 6.1: In-plane control actions and  $\Delta v$  over the reconfiguration for the unconstrained Lyapunov controller.

As shown in Figure 6.2a, the controller steers towards the final target in 15 orbits. Initially, the controller quickly departs for the desired target relative eccentricity and approaches fairly closely, but some observed

error remains in the y-component of relative eccentricity. The relative inclination vector reaches the target within 5.6 cm and 11.2 cm. Since the relative mean longitude is not controlled in this implementation, it drifts freely, producing the largest error as shown in Figure 6.2b, and ends up roughly 40 m apart from the initial state. This unconstrained Lyapunov controller thus requires additional enhancements to regulate the effects of the applied control actions on the relative mean longitude. The method for controlling  $\Delta\delta\lambda$  will be described in the next section.

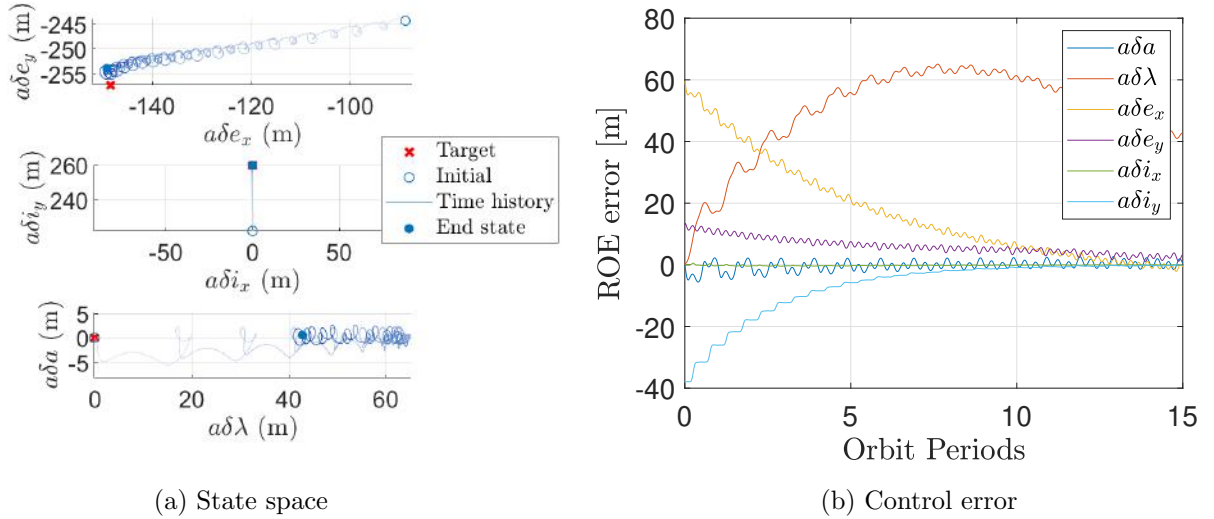


Figure 6.2: ROE state space and control error for the reconfiguration using unconstrained Lyapunov continuous control.

## 6.2 Controllability of Relative Mean Longitude

### 6.2.a Theory

As described in Steindorf [20], the controllability of the relative mean longitude is handled by variations in the relative semi-major axis. We begin by setting a reference state that we would like the deputy to follow. In the previous section this reference was simply the reference ROEs. In this case, we can vary the relative semi-major axis of this relative state to force the Lyapounov controller to bound its drift. We begin with the end, where we set this desired relative semi-major axis as:

$$\delta a_a = -\frac{2}{3} \frac{\delta \dot{\lambda}_a}{n_c} \quad (79)$$

The desired drift in the relative mean longitude is determined from:

$$\delta \dot{\lambda}_a = \begin{cases} -\min \left\{ \frac{|\Delta\delta\lambda|}{\tau}, \delta \dot{\lambda}_{ref} \right\} & \text{if } \Delta\delta\lambda \geq 0 \\ \min \left\{ \frac{|\Delta\delta\lambda|}{\tau}, \delta \dot{\lambda}_{ref} \right\} & \text{if } \Delta\delta\lambda < 0 \end{cases} \quad (80)$$

$$\delta \dot{\lambda}_{ref} = \frac{3}{2} n_c |\delta a_{ref}| \quad (81)$$

Note here that  $\tau$  is an arbitrarily large number, and that  $\delta \dot{\lambda}_{ref}$  serves as a limit for how large of a desired drift in the relative mean longitude we can have. This desired drift is set by how much of a drift we can

impart through:

$$|\delta a_{ref}| = \frac{|\Delta \delta a_{tan}|}{2} \quad (82)$$

$$\Delta \delta a_{tan} = \frac{2}{a_c n_c \eta_c} (1 + e_c \cos f_c) \cdot \Delta v_{tan} \quad (83)$$

$$\Delta v_{tan} = \frac{u_d \cdot T}{4} \prod_{q=N, N-2, \dots}^4 \frac{q-1}{q} \quad (84)$$

Another hyperparameter is found here in  $u_d$ , which represents the desired acceleration ( $m/s^2$ ). From this hyperparameter, as can be seen, we can walk backwards to get to our new desired relative semi-major axis.

### 6.2.b Controller Results & Discussion

For this section we used the following hyperparameters (note that we update  $u_d$  such that it is equal to the magnitude of the current control action):

$$k = 3000, \quad N = 14, \quad \tau = T/2 = 2,847.6493 \text{ s} \quad u_d = |u_t^{RTN}| \quad (85)$$

In Figure 6.4, we see that although there still is some uncontrolled motion in the relative mean longitude, it is now bounded, and the controller keeps it closer to 0 than before. The effect of tracking the relative mean longitude is clear in comparing Figure 6.2b with 6.4b. The cumulative  $\Delta v$  for this maneuver and the control error at the end of the reconfiguration are shown in Figure 6.3. This result is  $\sim 5.1\%$  below the  $\Delta v$  lower bound, so it is at least within reason. Again, this is likely smaller than the theoretical lower bound because the final desired ROEs were not actually reached.

$$\Delta v = 0.0716 \text{ m/s}$$

$$a_c \Delta \delta \alpha = [0.4402 \quad -16.2888 \quad -0.7682 \quad 3.2329 \quad -0.0490 \quad -0.0743] \text{ m}$$

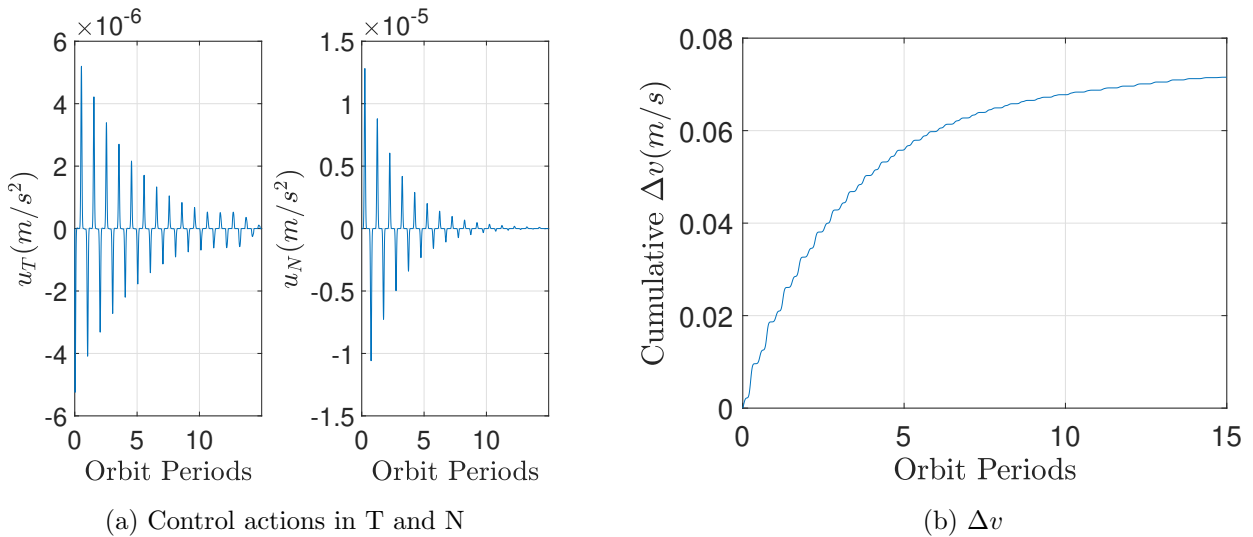


Figure 6.3: Control actions and  $\Delta v$  for the reconfiguration using unconstrained Lyapunov continuous control while tracking the relative mean longitude.

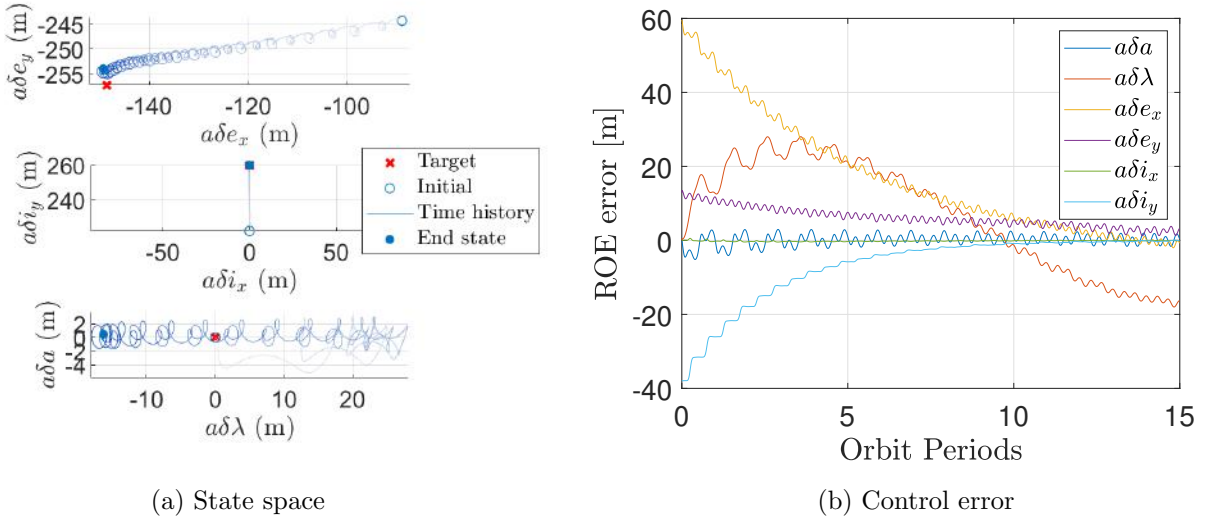


Figure 6.4: ROE state space and control error for the reconfiguration using unconstrained Lyapunov continuous control while tracking the relative mean longitude.

### 6.3 Time-Constrained Lyapunov Control

#### 6.3.a Theory

The TanDEM-X mission phase schedule requires the C1 to C2 reconfiguration to occur between days 179 and 180 of the mission. As such, there exists an optimal  $\Delta v$  maneuver to achieve this within the given time constraint. Lyapunov control with constraints is formulated using a reference governor to guide the controller to a goal state. The goal state is initialized as the final target state, the ROEs of mission phase C2. The reference governor is dynamic and changes with each time step to meet the defined constraints as given by

$$\delta\alpha_a = \delta\alpha_a + \delta\dot{\alpha}_a \cdot \delta t \quad (86)$$

$$\delta\dot{\alpha}_a = \xi[\Gamma - V] \cdot \rho \quad (87)$$

$$V = \frac{1}{2}\Delta\delta\alpha^T \cdot \Delta\delta\alpha \quad (88)$$

where  $V$  is the Lyapunov value and  $\xi$  is a hyperparameter. Since the time constraint is imposed on the problem without the need for a potential field, the gradient of the guiding potential field given as  $\rho$  is simply 1 in this case. The singular constraint for time,  $\Gamma_{time}$ , is a function of the in-plane and out-of plane components of control acceleration. This Lyapunov threshold is defined by

$$\Gamma_{time} = \frac{1}{2}\|\Delta\delta\alpha_{req}\|^2 = \frac{1}{2}\left(\frac{u_d}{\|\mathbf{B}_c^*\mathbf{P}\hat{\rho}_e\|}\right)^2 \quad (89)$$

$$\hat{\rho}_e = \frac{\Delta\delta\alpha}{\|\Delta\delta\alpha\|} \quad (90)$$

$$u_{d,ip} = \frac{2\Delta v_{ip}^{opt}}{T \cdot \# \text{ orbits}} \prod_{q=N,N-2}^4 \frac{q-1}{q} \quad (91)$$

$$u_{d,oop} = \frac{2\Delta v_{oop}^{opt}}{T \cdot \# \text{ orbits}} \prod_{q=N, N-2}^4 \frac{q-1}{q} \quad (92)$$

The required optimal  $\Delta v$  changes are influenced by the final target state through the variations  $\Delta \delta e$  and  $\Delta \delta i$ , which denote the complete reconfiguration from the initial ROEs of C1 to the final of C2. By setting the desired number of orbits for the reconfiguration maneuver to 15, or approximately one day, the control accelerations may be shaped to meet this requirement.

$$\Delta v_{ip}^{opt} = a_c n_c \cdot \frac{\|\Delta \delta \mathbf{e}\|}{2\eta_c} \quad (93)$$

$$\Delta v_{oop}^{opt} = a_c n_c \frac{1 - e_c}{\eta_c} \|\Delta \delta \mathbf{i}_c\| \quad (94)$$

### 6.3.b Initial Results & Discussion

We attempted to implement this constraint with the Lyapunov continuous controller, but the controller did not converge. In our case, the reference state grows exponentially likely due to a bug in the calculation of the applied reference  $\delta \alpha_a$ . It was observed that  $\Gamma_{time}$  becomes very large and is not well bounded by the Lyapunov function V (e.g.  $\Gamma_{time} \sim 10^4$  and  $V \sim 10^{-9}$ ). Unfortunately, we were not able to determine with certainty the root cause of this issue. Since the Lyapunov threshold is so large, the reference ROE significantly increases and renders the orbit unstable. Because of this, we are unable to plot anything, since we only get about 30 iterations before the controller becomes intractable.

## 6.4 Comparison and Limitations of Lyapunov Control Implementation

The two approaches taken result in somewhat similar ROE errors and  $\Delta v$ , but the  $\Delta \delta \lambda$  controller manages a lower final error in the relative mean longitude as designed. Results from the simulations have shown that by controlling  $\Delta \delta \lambda$ , we can improve upon the error in relative mean longitude by 62%.

	Unconstrained Lyapunov	$\Delta \delta \lambda$ controller
$\Delta v$ (m/s)	0.0714	0.0716
$\Delta \delta a$ (m)	0.5702	0.4402
$\Delta \delta \lambda$ (m)	42.8177	-16.2888
$\Delta \delta e_x$ (m)	-0.6876	-0.7682
$\Delta \delta e_y$ (m)	3.3074	3.239
$\Delta \delta i_x$ (m)	-0.0558	-0.0490
$\Delta \delta i_y$ (m)	-0.1121	-0.0743

Table 6.2: Comparison of  $\Delta v$  expended and ROE error between the continuous controllers.

The main advantages of Lyapunov continuous control are that it is among one of the few control schemes that works with nonlinear dynamics models, and by use of Lyapunov functions, stability may be guaranteed. However, there are no guarantees of efficiency in Lyapunov control. Furthermore, any numerical errors in computing the pseudoinverse of the control input matrix  $B_c$  can violate the conditions for Lyapunov stability. As we have seen through these implementations, this scheme requires selection of several hyperparameters, and optimization of these values may be computationally intensive.

Though the Lyapunov control method can be applied to high specific-impulse thrusters such as the ones for fine attitude control on TDX, continuous control has not yet demonstrated sufficiently high TRL for practical use in flight.

## 7 Problem Set 7

### 7.1 Relative Orbit Control

Impulsive orbit control approaches were debugged and tested for the reconfiguration maneuver from C1 to C2 as well as orbit-keeping during the C1 mission phase. Reconfiguration was achieved using two methods, by the least-squares solution and the closed-form double-impulse solution from [9]. The model description, approach, and comparison between them has been updated in subsection 5.2. Formation keeping was implemented using the closed-form double impulse solution from [9] and this is described in detail in subsection 5.3.

Given the size of the propulsion system, we propose to perform impulsive relative orbit control (both reconfigurations and formation keeping) as done in the real TDX mission using the closed-form double-impulse solutions from [9].

### 7.2 Navigation System Design

Due to its extensive flight heritage and high technology readiness level, the implemented filter was designed based on an Extended Kalman Filter (EKF).

#### 7.2.a State Representation

In the real TanDEM-X mission, the absolute orbits are independently known with good accuracy from GPS measurements, and from this the relative state can be estimated. The Kalman filter estimates a state composed of both dynamical and non-dynamical parameters, including [8]:

- instantaneous relative position and velocity
- differential drag and solar radiation pressure constants
- measured accelerations
- differential clock offsets
- differential ionospheric path delays
- carrier phase ambiguities on each frequency

As a starting implementation, the selected state representation is made up of instantaneous relative position described by the ROEs in order to employ the associated J2 STM. Variations of the receiver clock offset and the float biases are set to zero as done in [18] to maintain a simple base model. Force parameters including drag and other higher-order forces are not relevant as previously explained. The state is therefore defined by the quasi-nonsingular ROEs:

$$\vec{y} = [\delta a, \delta \lambda, \delta e_x, \delta e_y, \delta i_x, \delta i_y] \quad (95)$$

### 7.2.b State Prediction Dynamics Model

The Extended Kalman Filter (EKF) state prediction is performed using a linearized STM. The chosen STM operates on the ROE state and accounts for J2 which is desirable as the dominant perturbation. The STM is given as follows [12]:

$$\Phi_{qns}^{J2} = \begin{bmatrix} 1 & 0 & 0 & 0 & 0 & 0 \\ -\left(\frac{3}{2}n + \frac{7}{2}\kappa EP\right)\tau & 1 & \kappa e_{xi}FGP\tau & \kappa e_{yi}FGP\tau & -\kappa FS\tau & 0 \\ \frac{7}{2}\kappa e_{yf}Q\tau & 0 & \cos(\dot{\omega}\tau) - 4\kappa e_{xi}e_{yf}GQ\tau & -\sin(\dot{\omega}\tau) - 4\kappa e_{yi}e_{yf}GQ\tau & 5\kappa e_{yf}S\tau & 0 \\ -\frac{7}{2}\kappa e_{xf}Q\tau & 0 & \sin(\dot{\omega}\tau) + 4\kappa e_{xi}e_{xf}GQ\tau & \cos(\dot{\omega}\tau) + 4\kappa e_{yi}e_{xf}GQ\tau & -5\kappa e_{xf}S\tau & 0 \\ 0 & 0 & 0 & 0 & 1 & 0 \\ \frac{7}{2}\kappa S\tau & 0 & -4\kappa e_{xi}GS\tau & -4\kappa e_{yi}GS\tau & 2\kappa T\tau & 1 \end{bmatrix} \quad (96)$$

J2 perturbations are included in this definition as seen through the drift rate of the argument of periapsis, given by Brouwer as [12]

$$\dot{\omega} = \frac{3}{4} \frac{J_2 R_E^2 \sqrt{\mu}}{a^{7/2} \eta^4} (5 \cos^2(i) - 1) \quad (97)$$

The subscripts  $i$  and  $f$  indicate the initial and final quantities of the time interval of interest  $\tau$ .

$$\begin{aligned} e_{xi} &= e_c \cos \omega_i & e_{yi} &= e_c \sin \omega_i \\ e_{xf} &= e_c \cos \omega_f & e_{yf} &= e_c \sin \omega_f \\ \omega_f &= \omega_i + \dot{\omega}\tau \end{aligned}$$

The following auxiliary variables are also introduced for convenience:

$$\begin{aligned} \eta &= \sqrt{1 - e_c^2} & \kappa &= \frac{3}{4} \frac{J_2 R_E^2 \sqrt{\mu}}{a^{7/2} \eta^4} & E &= 1 + \eta & F &= 4 + 3\eta & G &= \frac{1}{\eta^2} \\ P &= 3 \cos^2(i) - 1 & Q &= \cos^2(i) - 1 & R &= \cos(i) & S &= \sin(2i) & T &= \sin^2(i) \\ U &= \sin(i) & V &= \tan(i/2) & W &= \cos^2(i/2) \end{aligned}$$

The control input matrix for the EKF is a function of the true anomaly of the chief, and is given by [19]

$$B_c = \frac{1}{a_c n_c} \begin{bmatrix} \frac{2}{\eta_c} e_c \sin f_c & \frac{2}{\eta_c} (1 + e_c \cos f_c) & 0 \\ -\frac{2\eta_c^2}{1 + e_c \cos f_c} & 0 & 0 \\ \eta_c \sin(\omega_c + f_c) & \eta_c \frac{(2 + e_c \cos f_c) \cos(\omega_c + f_c) + e_x}{1 + e_c \cos f_c} & \frac{\eta_c e_y}{\tan i_c} \frac{\sin(\omega_c + f_c)}{1 + e_c \cos f_c} \\ -\eta_c \cos(\omega_c + f_c) & \eta_c \frac{(2 + e_c \cos f_c) \sin(\omega_c + f_c) + e_y}{1 + e_c \cos f_c} & \frac{-\eta_c e_x}{\tan i_c} \frac{\sin(\omega_c + f_c)}{1 + e_c \cos f_c} \\ 0 & 0 & \eta_c \frac{\cos(\omega_c + f_c)}{1 + e_c \cos f_c} \\ 0 & 0 & \eta_c \frac{\sin(\omega_c + f_c)}{1 + e_c \cos f_c} \end{bmatrix} \quad (98)$$

### 7.2.c Covariance Propagation

The EKF covariance update is performed using the same linearized STM as with the state update.

### 7.2.d Navigation Sensors

The TDX and TSX spacecraft are each equipped with 3 GPS receiver units for navigation, two of which are single-frequency redundant MosaicGNSS receivers. The primary unit is a dual-frequency TOR/IGOR receiver that provides pseudorange and carrier phase measurements on the L1 and L2 frequencies. With this system, TSX has demonstrated an accuracy of 5 cm for absolute orbit determination [3]. Relative carrier phase measurements are as accurate as up to 1 mm, enabling precise relative orbit determination within 10 cm as required to produce DEM with the highest possible accuracy [8].

Star trackers and coarse earth and sun sensors are also onboard to provide attitude measurements. Spacecraft body rate measurements are obtained by a combination of laser gyros and magnetometers on TDX and an inertial measurement unit and magnetometer on TSX.

### 7.2.e Measurement Model

In this current implementation, the measurements are modeled as additive noise to the ground truth propagation (converted to ROEs). Ionospheric path delays to LEO are cited to produce GPS position error on the order of 10 meters, and therefore Gaussian noise with a standard deviation of 10 meters was implemented as done in [21].

For completeness, the full measurement state using GPS can be obtained by 12 GRow And Phase Ionosphere Correction (GRAPHIC) measurements taken by each of the chief and deputy spacecraft, along with 12 single difference carrier phase measurements [9]:

$$z = (\rho_{GR}^C, \rho_{GR}^D, \rho_{SDCP})$$

where the GRAPHIC measurement is defined as the average of the pseudorange and carrier phase:

$$\begin{aligned}\rho_{GR} &= \frac{\rho_{PR} + \rho_{CP}}{2} = \rho + c(\delta t - \delta t_{GPS}) + N + S_{GR} + \epsilon_{GR} \\ \rho_{PR} &= \rho + c(\delta t - \delta t_{GPS}) + I + S_{PR} + \epsilon_{PR} \\ \rho_{CP} &= \rho + c(\delta t - \delta t_{GPS}) - I + \lambda_1 N_{CP} + S_{CP} + \epsilon_{CP}\end{aligned}$$

Lastly, the single-difference carrier-phase model is given by:

$$\rho_{SDCP} = \Delta\rho_{CP} = \rho_{CP}^D - \rho_{CP}^T = \Delta\rho + c\Delta\delta t + 2\Delta N - I_0\Delta L + \Delta S_{CP} + \Delta\epsilon_{CP}$$

### 7.2.f Sensitivity Matrix

The measurement update is obtained through calculating partials with respect to the state using the sensitivity matrix. The current implementation utilizes the static sensor model as was implemented and verified by [18]:

$$H = I_{6 \times 6} \quad (99)$$

### 7.2.g Testing and Model Verification

The described models were tested and verified prior to implementation of the EKF. As done previously in Problem Set 4, the linear dynamics model obtained by J2 STM closely matches the nonlinear dynamics model by numerical integration over 100 orbits as seen in Figure 7.1.

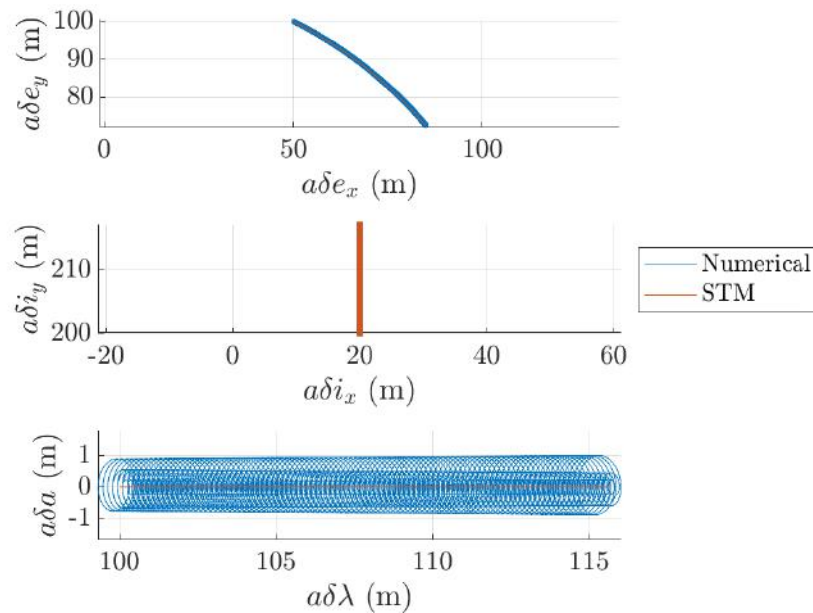


Figure 7.1: State space comparison of numerical and STM propagation over 100 orbits.

## 8 Problem Set 8

### 8.1 Navigation Filter

#### 8.1.a Extended Kalman Filter

For this mission, we chose to implement an EKF as the dynamics and measurement models are both non-linear. This filter is computationally efficient and has been widely deployed in space missions. Based on the previous state as reference, the EKF applies the linearized update rules given in Table 8.1 to estimate the current state  $x_k$  and associated covariance  $P_k$  [7].

Time Update	$\begin{aligned} x_k^- &= \Phi_{k-1}x_{k-1}^+ + w_{k-1} + B_{k-1}u_{k-1} \\ P_k^- &= \Phi_{k-1}P_{k-1}^+\Phi_{k-1}^T + Q_{k-1} \end{aligned}$
Measurement Update	$\begin{aligned} K_k &= P_k^- H_k^T (H_k P_k^- H_k^T + R_k)^{-1} \\ x_k^+ &= x_k^- + K_k(y_k - h_k(x_k^-)) \\ P_k^+ &= (I - K_k H_k)P_k^- (I - K_k H_k)^T + K_k R_k K_k^T \end{aligned}$

Table 8.1: EKF time and measurement update rules.

In this formulation,  $y_k$  is the measurement,  $u_k$  is the control input and  $w_k$  is additive white noise accumulated by uncertainty in the dynamics. The term  $Q_k$  is process noise and  $R_k$  is measurement noise associated with the sensors.  $h_k$  is the measurement model which can be nonlinear and  $H_k = \frac{\partial h}{\partial x}\Big|_{x_k^-}$ .

The potential disadvantage of using an EKF is that linearization may introduce bias and its performance and stability are not guaranteed, as it can become unreliable in some cases with large non-linearities. In the following sections, we show that the filter was found to perform quite well with acceptable estimation error.

#### 8.1.b Choice of state representation

As in 7.2, a simplified state comprised of the set of relative orbital elements is estimated. The measurement model is designated as the ground truth state with added zero-mean Gaussian noise. The Gaussian noise has a variance of  $\sigma = 10$  meters representing imprecision in the onboard sensors.

#### 8.1.c Implementation details

No additional noise or control inputs are considered in this model:

$$\begin{aligned} w_k &= 0 \\ u_k &= 0 \end{aligned}$$

Noise covariances were chosen based on the selected Gaussian noise applied to the ground truth. Process noise was defined to be orders of magnitude smaller than the state covariance as similarly done in [18],

indicating that there is greater trust in the dynamics model than in the measurements.

$$\begin{aligned} P_0 &= 10 \cdot I_{6 \times 6} \\ Q_k &= Q = P_0/1000 \\ R_k &= R = P_0 \end{aligned}$$

### 8.1.d Simulation and results

Beginning with the initial conditions defined in 6.1.a, the ground truth is propagated by numerical integration of the FODE as described in 7.2.b, and the state is estimated using the EKF. Figure 8.1 shows the ground truth state superimposed along with the estimated state. We see that the state estimated by the EKF quickly converges within approximately 2 orbits to be similar, but not quite identical, to the ground truth. The EKF appears to estimate  $\delta a$ ,  $\delta \lambda$ ,  $\delta e_x$ , and  $\delta e_y$  most closely while the error is larger in the inclination vector.

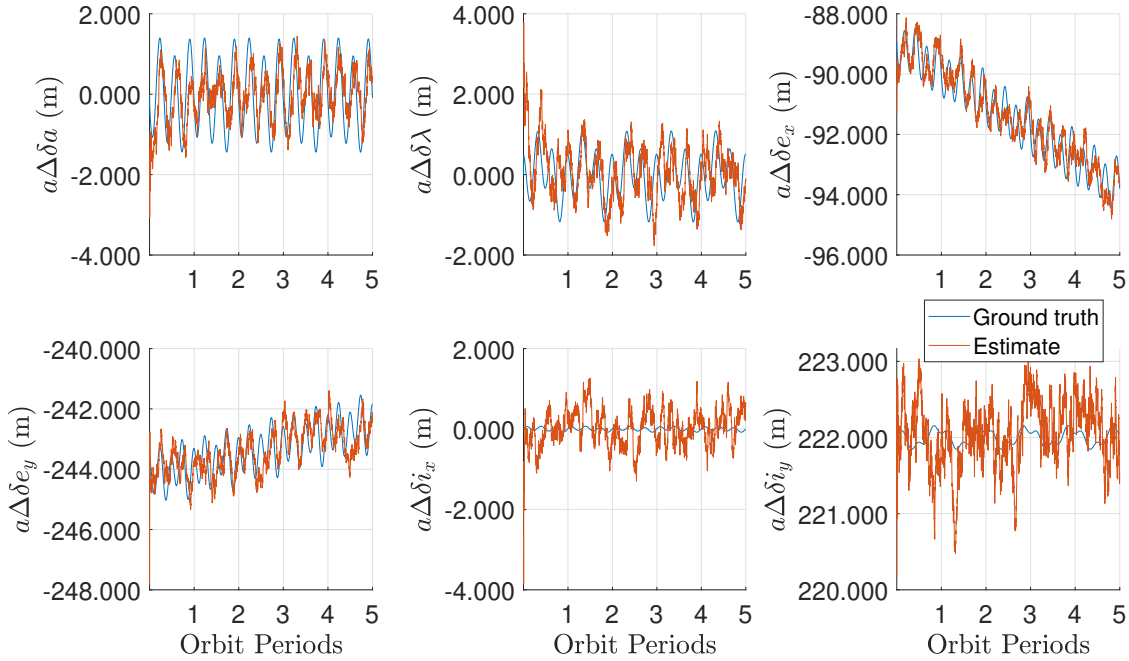


Figure 8.1: Ground truth and estimated ROE state over 5 orbits.

The estimation error is computed as the difference between the true and estimated states and is shown in Figure 8.2 with 3 standard deviation bounds. The error mostly stays within these bounds, with the most evident violations in  $\delta \lambda$  initially and near orbits 1 and 3. As before, the state begins with large error and quickly settles into a converged state estimate. Examining the plot more closely in Figure 8.3, the uncertainty drops from its high initial value and reaches steady state within 0.3 orbits, confirming the fast convergence of the EKF.

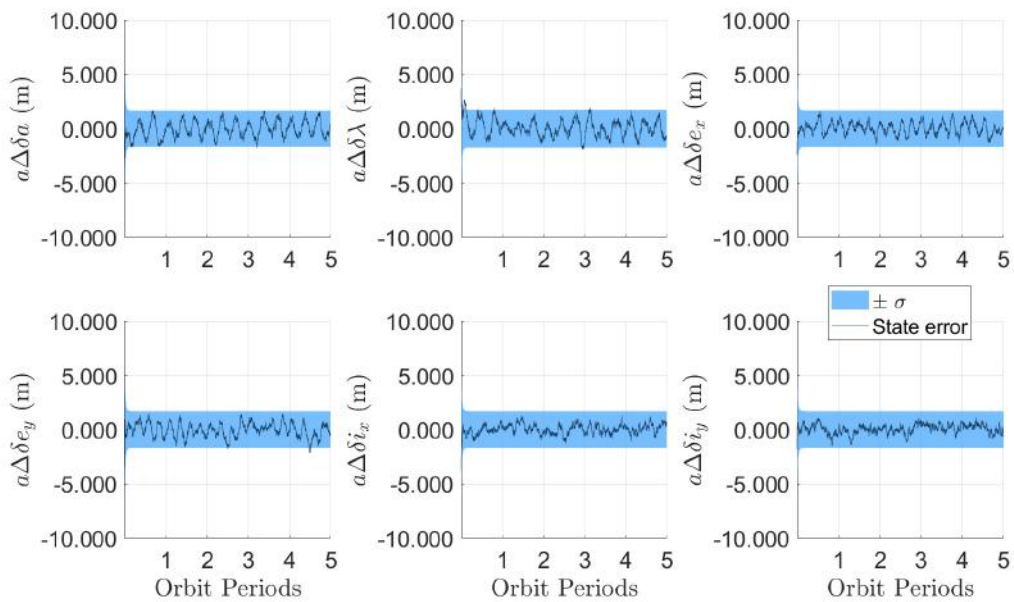


Figure 8.2: State estimation error with 3 standard deviations centered about 0.

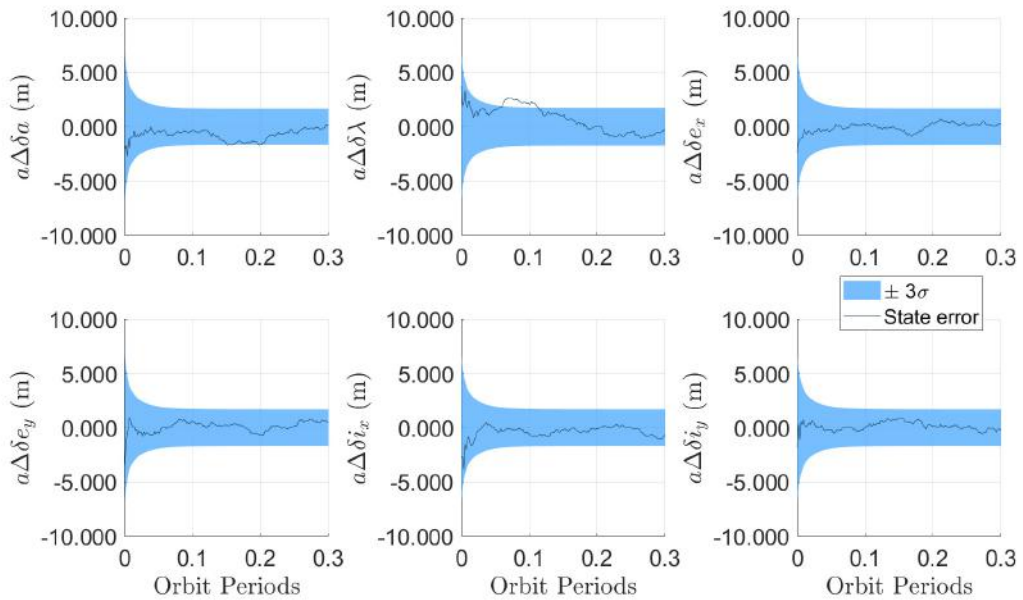


Figure 8.3: Convergence of the state estimation error within 0.3 orbits shown with 3 standard deviations.

The steady-state covariance reached after 0.3 orbits reflects the filter's increased confidence in the estimate:

$$P = \begin{bmatrix} 0.302 & -0.0740 & 0 & 0 & 0 & 0 \\ -0.0740 & 0.339 & 0 & 0 & 0 & 0 \\ 0 & 0 & 0.311 & 0 & 0 & 0 \\ 0 & 0 & 0 & 0.311 & 0 & 0 \\ 0 & 0 & 0 & 0 & 0.311 & 0 \\ 0 & 0 & 0 & 0 & 0 & 0.311 \end{bmatrix}$$

Taking the square root of the diagonal entries of  $P$ , the estimate standard deviations are approximately:

$$\sigma = [0.5495, \quad 0.5822, \quad 0.5577, \quad 0.5577, \quad 0.5577, \quad 0.5577] \text{ m}$$

In truth, the mean and standard deviation of the estimation error at steady state in the last orbit are found to be:

$$\begin{aligned} \mu_{ss} &= [-0.0142, \quad 0.0207, \quad -0.0664, \quad -0.3722, \quad 0.1455, \quad 0.1071] \text{ m} \\ \sigma_{ss} &= [0.6951, \quad 0.7545, \quad 0.5733, \quad 0.6608, \quad 0.4387, \quad 0.4001] \text{ m} \end{aligned}$$

We see from these true statistics that the estimated error and true error covariances are quite similar, indicating good convergence of the EKF.

Residuals are used in the filter update to improve the estimation in each iteration. In other words, the EKF seeks to minimize the post-fit residuals determined after the state update. In Figure 8.4, the pre-fit residuals are plotted along with the post-fit residuals. These quantities are defined as the difference between the actual observations and the state predicted by the model as given by

$$\begin{aligned} \text{pre-fit} &= y - Hx_k^- \\ \text{post-fit} &= y - Hx_k^+ \end{aligned}$$

It is observed that the residuals roughly stay within bounds of the 10-meter injected Gaussian noise. The magnitude of the post-fit residuals are slightly smaller than the pre-fit residuals as a result of the update. The mean and standard deviation of the residuals are given in Table 8.2.

	$a\delta a$	$a\delta \lambda$	$a\delta e_x$	$a\delta e_y$	$a\delta i_x$	$a\delta i_y$
Pre-fit mean	0.0140	-0.0330	0.0130	0.00400	0.0180	-0.00400
Pre-fit std. dev.	3.243	3.258	3.178	3.243	3.161	3.231
Post-fit mean	0.0130	-0.0310	0.0120	0.00300	0.0160	-0.00500
Postfit std. dev.	3.142	3.145	3.078	3.139	3.059	3.127

Table 8.2: Mean and standard deviation statistics of the pre-fit and post-fit residuals.

The implemented EKF was shown to converge quickly with maximum state error on the order of 37 centimeters. A computationally efficient and practical approach for space navigation, this filter provides a useful baseline for further development of more complex EKFs that may include additional non-dynamical parameters in the state representation.

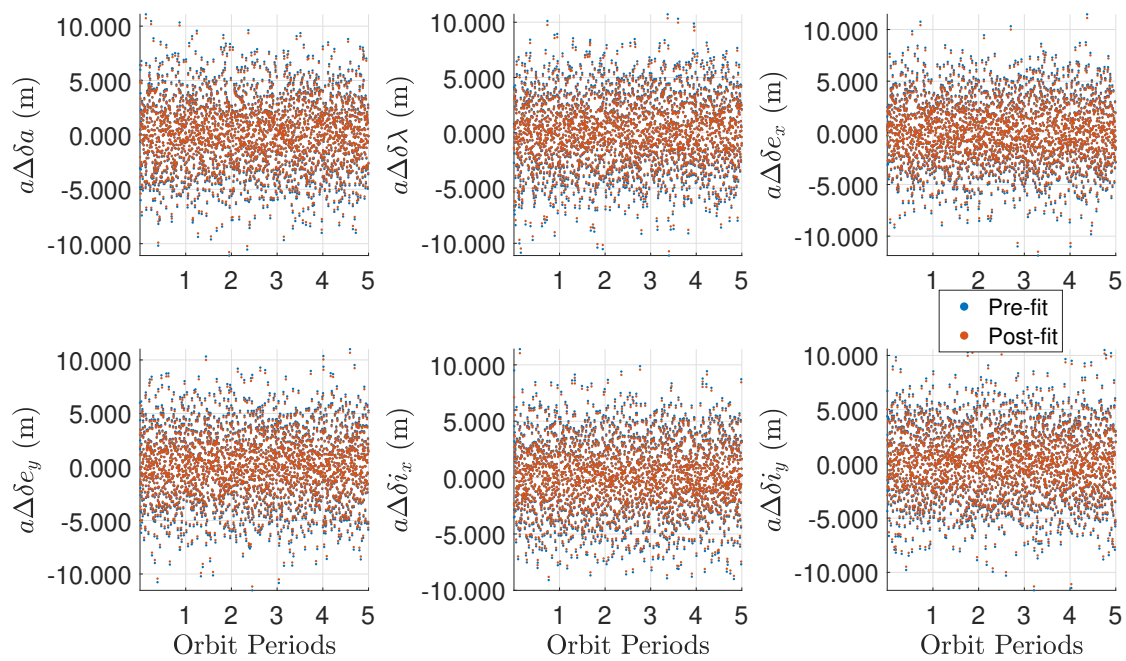


Figure 8.4: Pre-fit and post-fit residuals across 5 orbits.

## 9 Problem Set 9

### 9.1 Model Improvements

#### Problem Sets 1–3

The initial conditions for the absolute orbit of the chief and relative offset of the deputy were updated to be consistent with the rest of the problem sets. Numerical stability issues were fixed.

In addition, axes on the RTN plots were updated for clarity.

#### Problem Set 4

Initial conditions and resulting plots were updated. Previous numerical instability in  $\delta\lambda$  was resolved.

#### Problem Set 6

The  $\Delta v$  lower bounds were re-computed as in-plane and out-of-plane components for the Lyapunov controller in sections 6.1.c and 6.1.d. The results favorably show that the implemented controller is optimal for the reconfiguration maneuver, as the actual  $\Delta v$  performed is equivalent to the theoretical  $\Delta v$  lower bound with marginal numerical error.

#### Problem Set 7

The definition of the navigation filter was updated to match what was actually implemented in the following problem sets. A test case for the dynamics used in the EKF was also included.

#### Problem Set 8

State estimation error plots were updated such that the standard deviation bounds are centered on zero (Figure 8.2 and Figure 8.3), enabling points of departure from the bounds to be identified. Plots of the pre-fit and post-fit residuals in Figure 8.4 were updated using scatter for visibility. The mean and standard deviation statistics of the residuals were computed and added to the report in Table 9.3.

## 9.2 Integration of Navigation and Control

### 9.2.a Additive noise

The control law for formation-keeping as described in 5.3 was implemented previously using a double-impulse maneuver scheme. As detailed in section 5.2.c, the  $\Delta v$  magnitudes are determined dynamically by the ROE state as the orbit is propagated. Starting with the position and velocity of the chief and deputy spacecraft in the ECI frame, these are converted into osculating and mean orbital elements. From the mean orbital elements, the ROE state is obtained. Here, zero-mean Gaussian noise with a covariance of 10 meters is added to the ROE state, simulating the measured ROEs.

When the ground truth is corrupted with Gaussian noise, the controller expends more fuel as it attempts to correct the formation. In contrast to the noiseless implementation, which only required two maneuvers over 150 orbits, this controller executed 7 maneuvers, or 21 burns as illustrated in Figure 9.1. Whereas the noiseless controller expended a total  $\Delta v$  of 0.0739 m/s, this required 0.157 m/s, or more than double the amount of fuel.

As shown in Figure 9.2, there appears to be larger variation in the ROEs as to be expected with the addition of noise. However, the controller is unable to regulate  $\delta\lambda$  as before, which results in a significantly larger drift.

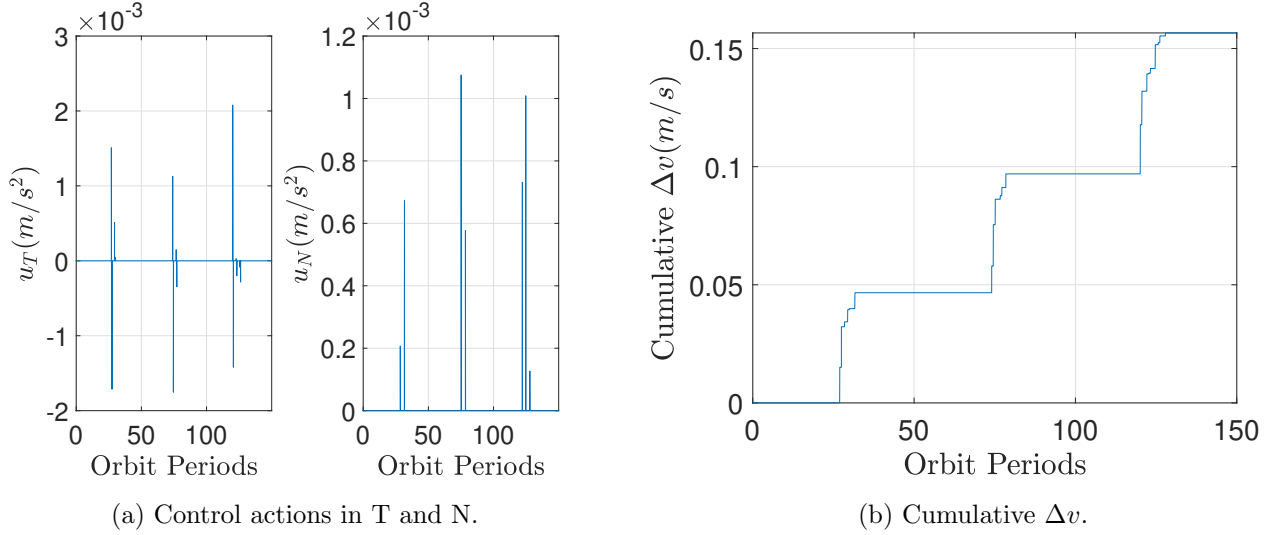


Figure 9.1: In-plane control actions and  $\Delta v$  over the formation keeping with noisy measurements.

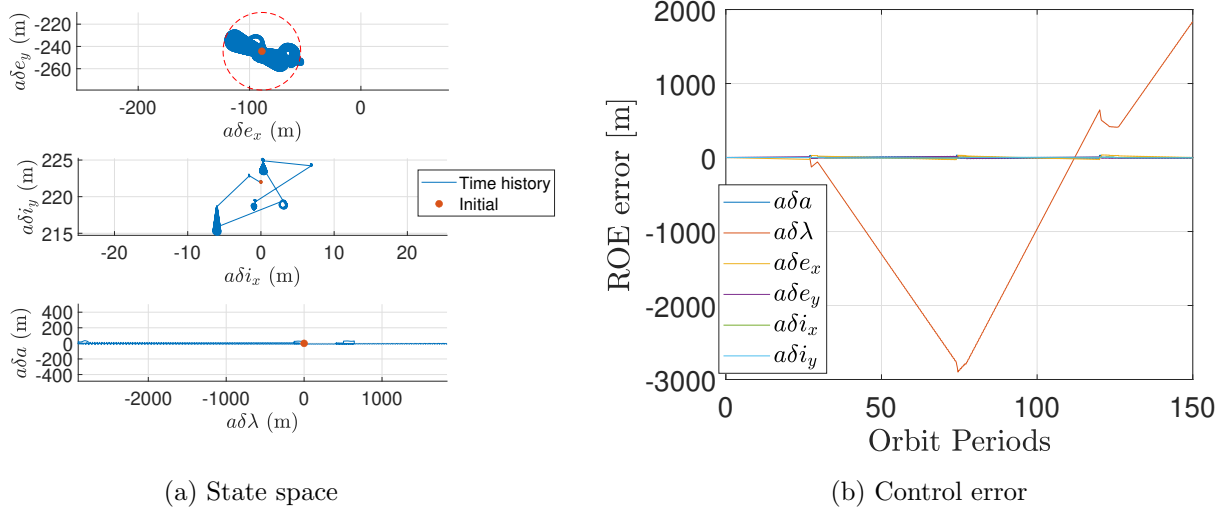


Figure 9.2: ROE state space and control error for formation keeping with noisy measurements.

### 9.2.b Filtering the measurements

The extended Kalman filter implemented in the previous problem set was applied to estimate the ROE state as extracted from noisy measurements. In this case, the control inputs are now accounted for in the prediction step. The control input matrix is a function of the true anomaly and is given by [19]:

$$B_c = \frac{1}{a_c n_c} \begin{bmatrix} \frac{2}{\eta_c} e_c \sin f_c & \frac{2}{\eta_c} (1 + e_c \cos f_c) & 0 \\ -\frac{2\eta_c^2}{1+e_c \cos f_c} & 0 & 0 \\ \eta_c \sin(\omega_c + f_c) & \eta_c \frac{(2+e_c \cos f_c) \cos(\omega_c + f_c) + e_x}{1+e_c \cos f_c} & \frac{\eta_c e_y \sin(\omega_c + f_c)}{\tan i_c \frac{1+e_c \cos f_c}{1+e_c \cos f_c}} \\ -\eta_c \cos(\omega_c + f_c) & \eta_c \frac{(2+e_c \cos f_c) \sin(\omega_c + f_c) + e_y}{1+e_c \cos f_c} & \frac{-\eta_c e_x \sin(\omega_c + f_c)}{\tan i_c \frac{1+e_c \cos f_c}{1+e_c \cos f_c}} \\ 0 & 0 & \eta_c \frac{\cos(\omega_c + f_c)}{1+e_c \cos f_c} \\ 0 & 0 & \eta_c \frac{\sin(\omega_c + f_c)}{1+e_c \cos f_c} \end{bmatrix} \quad (100)$$

The controller perceives the control window to be violated twice, executing 2 burns within the 150 orbit period as shown in Figure 9.3. Examining the ROE state space in Figure 9.4a, the eccentricity bounds are slightly violated, likely due to marginal numerical error in the  $\Delta v$  executed by the control law. Given this slight difference, it is important that the defined eccentricity bounds incorporate some margin of error in practice to account for imprecise computation as well as propulsion system inaccuracies.

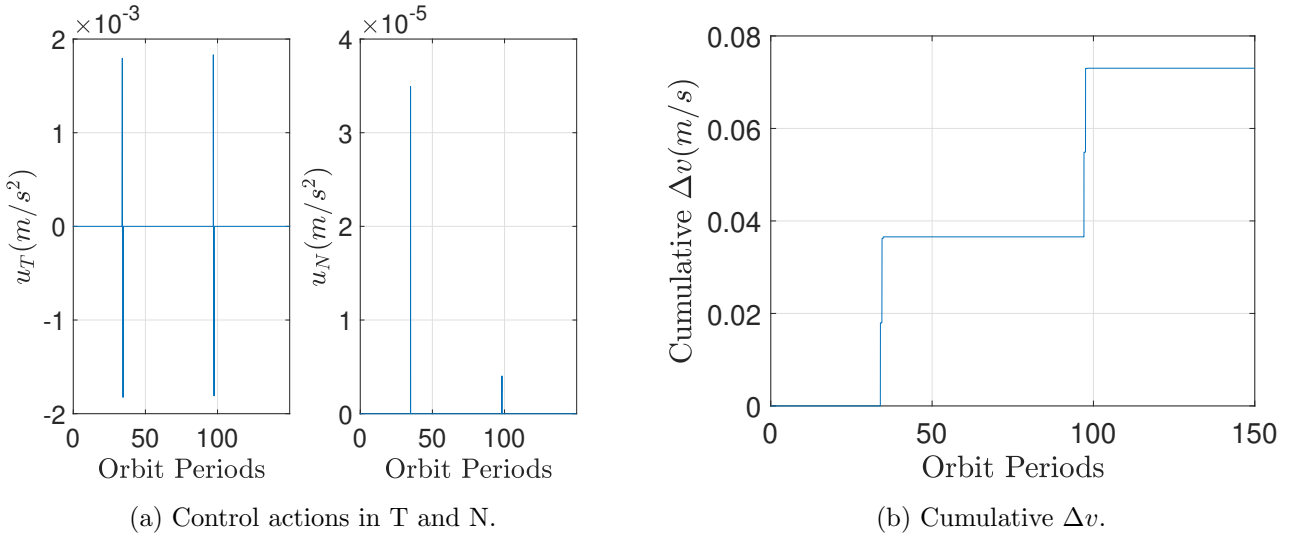


Figure 9.3: In-plane control actions and  $\Delta v$  over the formation keeping with filtered measurements.

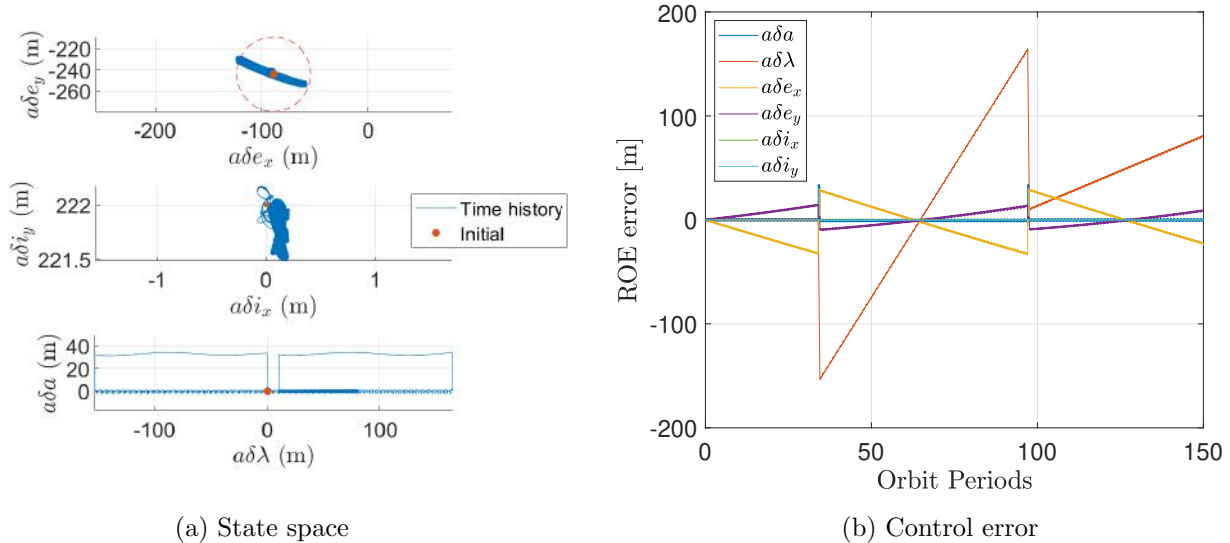


Figure 9.4: ROE state space and control error for formation keeping with filtered measurements.

### Comparison to controller with noisy measurements

With the measurements filtered by the EKF, control of the formation is re-established and the eccentricity remains within the allowed bounds. Figure 9.4 shows that control is significantly improved in  $\delta\lambda$ , as the ROE error stays within approximately  $\pm 170$  meters. The inclination vector is also better controlled, improving from within approximately 5m without the filter to within less than 1m.

The filtered controller achieves formation-keeping using fewer burns and less expended fuel. The cumulative  $\Delta v$  amounts to approximately 0.0730 m/s as shown in Figure 9.3.

### Comparison to noiseless controller

The results appear quite similar to the formation-keeping controller implemented in Problem Set 5 with perfectly noiseless tracking. The noiseless controller also achieved formation-keeping using 2 burns over 150 orbits with a comparable  $\Delta v$  of 0.0739 m/s. Control of the relative inclination vector by the filtered controller is noticeably less tight than the noiseless controller, but the relative mean latitude is regulated in both cases.

Since the timing of burns is roughly about the same in both implementations, the similar performance between the controllers validates the effectiveness of the EKF in filtering through the Gaussian noise.

### Evaluation of Control and Navigation

Control tracking errors as shown in Figure 9.4b are obtained as the difference between the desired relative motion described by the nominal ROEs and the actual relative motion. In RTN space, the errors amount to a root-mean squared error of the 3D position of approximately 62.740 meters. The magnitude of this error is largely attributed to the loosely controlled  $\delta\lambda$ , although it still satisfies the 250-meter elliptical window

mission requirement. Computed steady-state mean and standard deviation of the control tracking error as defined by the last 10 orbits are given in Table 9.1 in ROE space and in Table 9.2 in RTN coordinates.

	$a\delta a$ (m)	$a\delta \lambda$ (m)	$a\delta e_x$ (m)	$a\delta e_y$ (m)	$a\delta i_x$ (m)	$a\delta i_y$ (m)
Control error mean	-0.144	73.999	-18.000	6.759	0.145	-0.122
Control error std. dev.	0.921	3.930	2.821	1.400	0.0436	0.097

Table 9.1: Control tracking error statistics in the ROE state.

	R (m)	T (m)	N (m)	R (m/s)	T (m/s)	N (m/s)
Mean error	-3.813	-14.767	-0.168	0.272	0.107	$-1.299 \times 10^{-4}$
Std. dev. error	16.914	57.248	0.144	$7.108 \times 10^{-3}$	0.0371	$7.868 \times 10^{-5}$

Table 9.2: Control steady-state RTN error.

True navigation errors are computed by subtracting the estimated ROE state from the ground truth reference trajectory. The navigation error in ROE space is plotted in Figure 9.5 and is shown with 3 standard deviations. Large peaks observed in the relative eccentricity vector correspond to the control burns. As shown in Figure 9.6, estimation covariance settles and the EKF converges within approximately 0.34 orbits. Convergence occurs relatively quickly, which is particularly apt for this application in formation-keeping over long time scales.

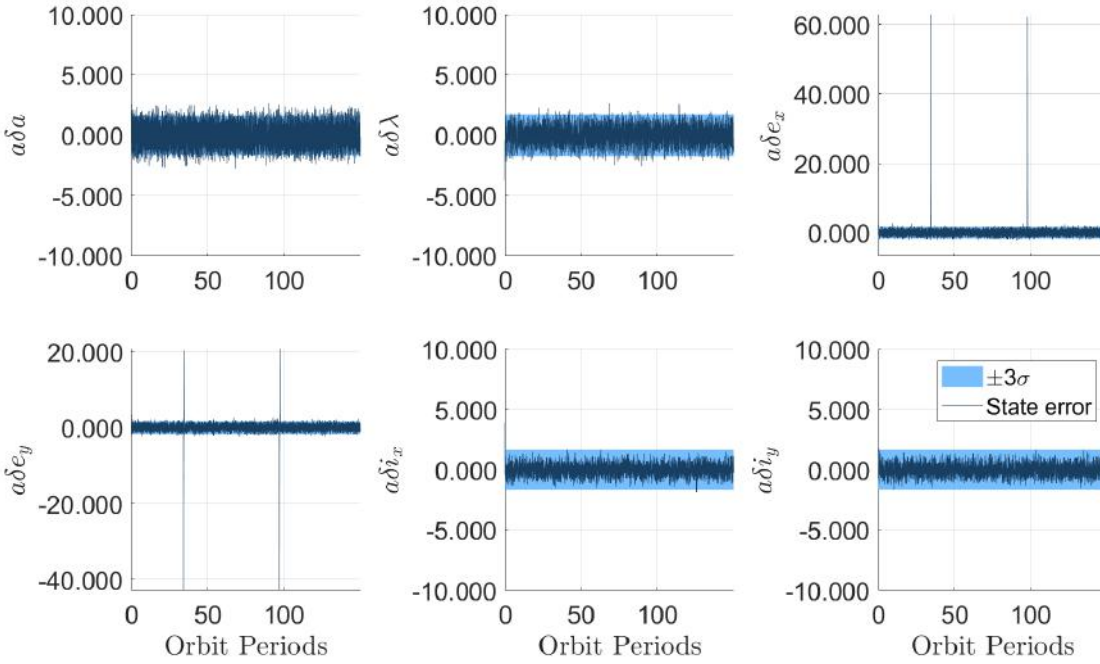


Figure 9.5: State estimation error with 3 standard deviations centered around 0.

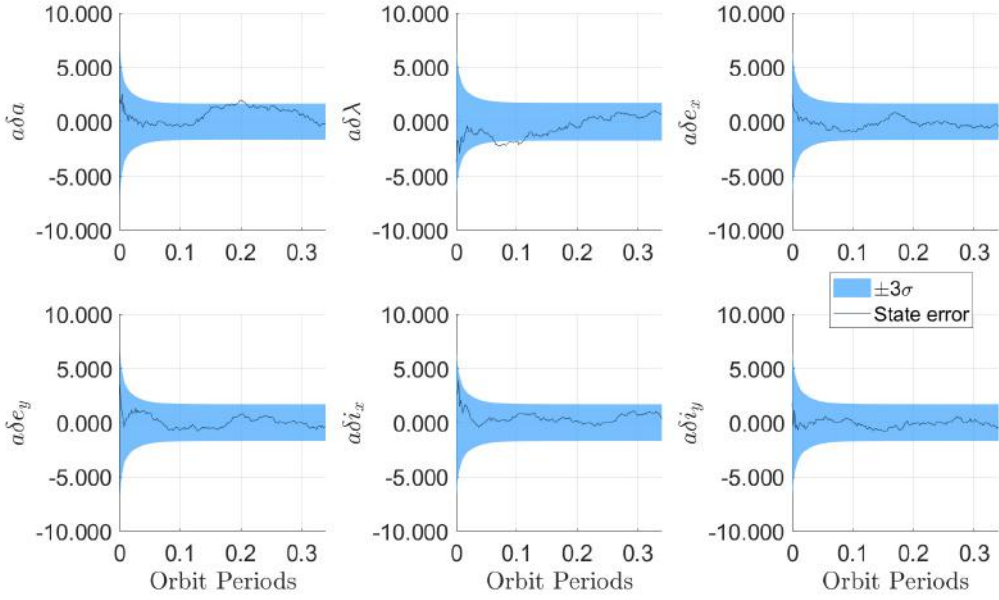


Figure 9.6: Convergence of the state estimation error within 1/3 of an orbit shown with 3 standard deviations.

A plot of the residuals in the last 10 orbits reveals that the pre-fit and post-fit residuals both remain roughly within the 10-meter Gaussian noise as shown in Figure 9.7. Throughout the simulation, the post-fit residuals are lower than the pre-fit residuals, indicating the effect of filtering. The mean and standard deviation statistics of the residuals are given in Table 9.3.

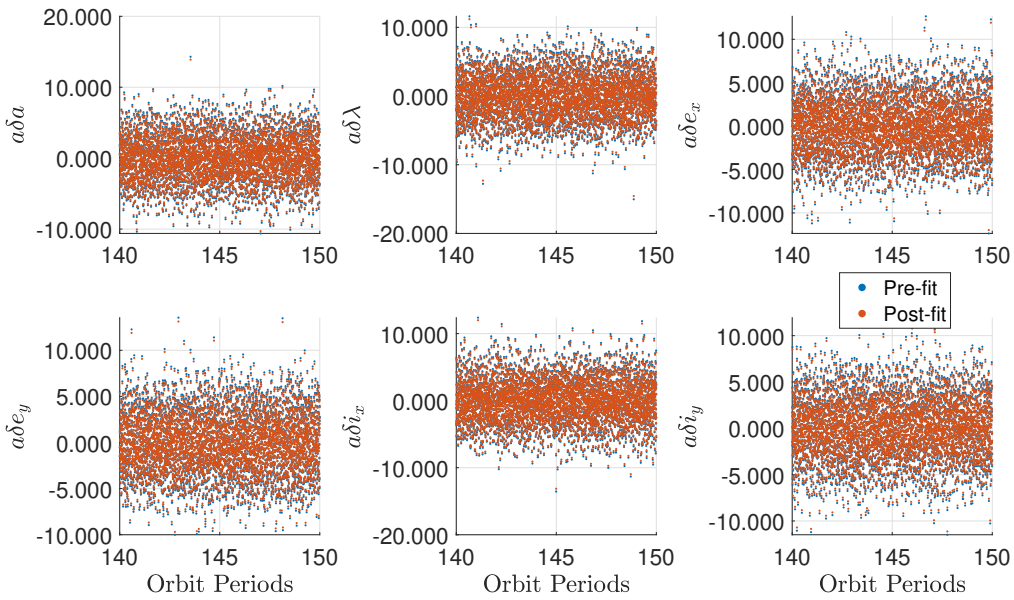


Figure 9.7: Pre-fit and post-fit residuals across the final 10 orbits.

ROE (m)	$a\delta a$	$a\delta \lambda$	$a\delta e_x$	$a\delta e_y$	$a\delta i_x$	$a\delta i_y$
Pre-fit mean	$3.894 \times 10^{-4}$	$-5.081 \times 10^{-4}$	0.0467	-0.0171	$2.237 \times 10^{-4}$	$1.005 \times 10^{-5}$
Pre-fit std. dev.	3.193	3.193	3.428	3.331	3.190	3.200
Post-fit mean	$3.632 \times 10^{-4}$	$-4.607 \times 10^{-4}$	0.0453	-0.166	$1.949 \times 10^{-4}$	$-1.111 \times 10^{-5}$
Postfit std. dev.	3.097	3.084	3.321	3.227	3.091	3.100

Table 9.3: Mean and standard deviation statistics of the pre-fit and post-fit residuals over the entire simulation.

Computed true navigation error and formal error covariances from the filter ( $P$  matrix) are tabulated in Table 9.4.

ROE (m)	$a\delta a$	$a\delta \lambda$	$a\delta e_x$	$a\delta e_y$	$a\delta i_x$	$a\delta i_y$
Navigation error true mean	0.073	-0.080	0.008	0.065	0.012	0.015
Navigation error true std. dev.	1.009	0.754	0.708	0.726	0.426	0.382
Navigation error formal std. dev.	0.549	0.583	0.558	0.558	0.558	0.558

Table 9.4: Navigation ROE error excluding the convergence phase of the EKF.

Figure 9.8 shows the relative navigation error mapped into the RTN frame, which remain within 2/3.1/5 m in radial, along-track, and cross-track directions outside of the maneuvers. Peaks in the plot reflect the impact of the two control actions executed for formation-keeping. The implemented EKF is evaluated to provide an accuracy of approximately 1.975m (3D root-mean squared error), substantially improving on the 10-meter injected noise. In this case, the navigation filter is overconfident as it produces a smaller estimated covariance compared to the true covariance.

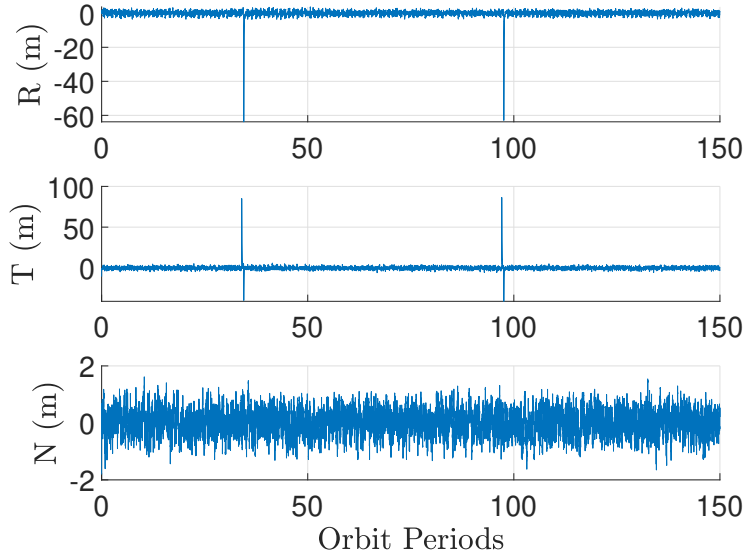


Figure 9.8: Navigation error mapped into the orbital frame aligned with radial (top), along-track (middle), and cross-track (bottom) directions.

### 9.3 Conclusions and Way Forward

#### 9.3.a Summary

Distributed space systems extend beyond the capabilities of a single spacecraft to accomplish advanced missions. Theory and methodology of spacecraft formation-flying was built up from foundational astrodynamics and methods developed in recent research to model the twin-satellite TanDEM-X mission. Requirements set by the real-life SAR mission influenced the approach to modeling the dynamics, navigation, guidance and control of the spacecraft. Various numerical and analytical algorithms were implemented, and their performance was compared through simulations. Relative dynamics were used to design safe orbits while maintaining acceptable separation between the spacecraft. Finally, a navigation stack was developed and integrated with an impulsive controller to simulate formation flying orbit-keeping for the preliminary mission phase.

#### 9.3.b Critical Assessment of Results

The results were shown to favorably adhere to the control window and navigation requirements, so the implemented algorithms are likely robust to the given simulation. The simulation itself, though, is not a full representation of the truth as many processes are modeled ideally or simplified. For better validation of performance in the true space environment, one could include more perturbing elements to the dynamics (drag, SRP, higher order gravity, and third body effects), modeling of maneuver inaccuracies, and better navigation sensor modeling.

That being said, as these algorithms were flown on TDX and other missions, we are confident they can translate well to higher fidelity simulations.

#### 9.3.c Lessons Learned

State representation can strongly impact modeling, computational efficiency and error, whether using singular, quasi-nonsingular, or purely non-singular orbital elements; position and velocity in the inertial or orbital frame; or relative orbital elements. Transformations between representations may be needed to implement certain algorithms and even slight numerical differences can accumulate into larger effects on the results.

Guidance and control of distributed space systems can be decoupled into two distinct problems. Guidance deals with motion over timescales longer than a single orbit, whereas the timescale in control is shorter. Guidance and maneuver planning can leverage the natural dynamics of spacecraft can to achieve optimal reconfigurations with minimal consumption of fuel.

There is no single ideal model for the dynamics, control, navigation, or guidance of formation-flying spacecraft missions. Rather, model design may be influenced by a number of factors depending on the mission application, including relevant perturbations for the orbit regime of interest, number of spacecraft, science requirements, and availability of absolute or relative measurements. Simpler linearized models such as STM propagation enable rapid computation and are therefore suitable for onboard processing, but at the cost of accuracy for higher-order non-linearities. Ground models generally ought to be higher-fidelity to provide an accurate reference for command and control.

### 9.3.d Potential Continuations

The following continuations were considered that could improve upon the simulation and algorithms:

- Implement GRAPHIC and Single Difference Carrier Phase (SDCP) measurements and incorporate GPS receiver clock offsets and biases into the navigation filter for a more realistic model.
- Explore other ways to achieve controllability of  $\delta\lambda$ .
- Model other sources of uncertainty to be more realistic, including actuators.
- Modeling higher-fidelity dynamics (drag, SRP, higher-order gravity, third body effects).

Additionally, a performance comparison of the simulation against the true flight data may bring up some additional areas of improvement for either implementation. In doing so, one could investigate how using an Unscented Kalman Filter may have performed in real flight.

## 10 References

- [1] H. J. Kramer. “Tdx (tandem-x).” (Sep. 2016), [Online]. Available: <https://www.eoportal.org/satellite-missions/tandem-x>.
- [2] G. Krieger, A. Moreira, H. Fiedler, *et al.*, “TanDEM-x: A satellite formation for high-resolution SAR interferometry,” *IEEE Transactions on Geoscience and Remote Sensing*, vol. 45, no. 11, pp. 3317–3341, Nov. 2007, ISSN: 1558-0644. DOI: [10.1109/TGRS.2007.900693](https://doi.org/10.1109/TGRS.2007.900693).
- [3] H. J. Kramer. “Tsx (terrasar-x).” (Jun. 2012), [Online]. Available: <https://www.eoportal.org/satellite-missions/terrasar-x>.
- [4] A. I. Flores-Anderson, K. E. Herndon, R. B. Thapa, and E. Cherrington, *The Synthetic Aperture Radar (SAR) Handbook: Comprehensive Methodologies for Forest Monitoring and Biomass Estimation*. SERVIR Global Science Coordination Office, Apr. 2019. DOI: [10.25966/nr2c-s697](https://doi.org/10.25966/nr2c-s697).
- [5] R. R. Bate, D. D. Mueller, and J. E. White, *Fundamentals of astrodynamics*, en. New York: Dover Publications, 1971, ISBN: 978-0-486-60061-1.
- [6] D. A. Vallado, *Fundamentals of Astrodynamics and Applications*. 1997.
- [7] K. T. Alfriend, S. R. Vadali, P. Gurfil, J. P. How, and L. S. Breger, *Spacecraft Formation Flying: Dynamics, Control, and Navigation*. Elsevier Astrodynamics Series, 2010.
- [8] O. Montenbruck, R. Kahle, S. D’Amico, and J.-S. Ardaens, “Navigation and control of the TanDEM-x formation,” *The Journal of the Astronautical Sciences*, vol. 56, no. 3, pp. 341–357, Sep. 1, 2008, ISSN: 0021-9142. DOI: [10.1007/BF03256557](https://doi.org/10.1007/BF03256557). [Online]. Available: <https://doi.org/10.1007/BF03256557>.
- [9] S. D’Amico, “Autonomous formation flying in low earth orbit,” Ph.D. dissertation, Technical University of Delft, 2010.
- [10] M. B. Willis, “Analytical theory of satellite relative motion with applications to autonomous navigation and control,” Ph.D. dissertation, Stanford University, 2023.
- [11] O. Montenbruck and E. Gill, *Satellite Orbits: Models, Methods, and Applications* (Physics and astronomy online library). Springer Berlin Heidelberg, 2000, ISBN: 9783540672807. [Online]. Available: <https://books.google.com/books?id=hABRnDlDkyQC>.
- [12] A. W. Koenig, T. Guffanti, and S. D’Amico, “New state transition matrices for spacecraft relative motion in perturbed orbits,” *Journal of Guidance, Control, and Dynamics*, vol. 40, no. 7, pp. 1749–1768, Jul. 2017. DOI: [10.2514/1.G002409](https://doi.org/10.2514/1.G002409).
- [13] S. D’Amico and O. Montenbruck, “Proximity operations of formation-flying spacecraft using an eccentricity/inclination vector separation,” en, *Journal of Guidance, Control, and Dynamics*, vol. 29, no. 3, May 2006. DOI: [10.2514/1.15114](https://doi.org/10.2514/1.15114). [Online]. Available: <https://doi.org/10.2514/1.15114> (visited on 05/07/2023).
- [14] M. Bachmann and T. Kraus, “The tandem-x mission phases—ten years of bistatic acquisition and formation planning,” en, *IEEE Journal of Selected Topics in Applied Earth Observations and Remote Sensing*, vol. 14, pp. 3504–3518, 2021. DOI: [10.1109/JSTARS.2021.3065446](https://doi.org/10.1109/JSTARS.2021.3065446). (visited on 05/07/2023).
- [15] R. Kahle, B. Schlepp, S. Aida, M. Kirschner, and M. Wermuth, “Flight dynamics operations of the tandem-x formation,” en, Jun. 2012. DOI: [10.2514/6.2012-1275094](https://doi.org/10.2514/6.2012-1275094). [Online]. Available: <https://doi.org/10.2514/6.2012-1275094> (visited on 05/07/2023).
- [16] “*1n, 20n, 400n, and heritage thruster*”, ”ArianeGroup”. [Online]. Available: <https://www.space-propulsion.com/brochures/hydrazine-thrusters/hydrazine-thrusters.pdf>.

- [17] M. Chernick and S. D'Amico, "New closed-form solutions for optimal impulsive control of spacecraft relative motion," *Journal of Guidance, Control, and Dynamics*, vol. 41, no. 2, pp. 301–319, 2018. DOI: [10.2514/1.G002848](https://doi.org/10.2514/1.G002848). eprint: <https://doi.org/10.2514/1.G002848>. [Online]. Available: <https://doi.org/10.2514/1.G002848>.
- [18] L. Steindorf, "Constrained low-thrust satellite formation-flying using relative orbit elements," University of Wurzburg and Lulea University of Technology, 2016.
- [19] M. Chernick, "Optimal impulsive control of spacecraft relative motion," Ph.D. dissertation, Stanford University, 2021.
- [20] L. Steindorf, S. D'Amico, J. Scharnagl, F. Kempf, and K. Schilling, "Constrained low-thrust satellite formation-flying using relative orbit elements," Jan. 2017.
- [21] S. Leung and O. Montenbruck, "Real-time navigation of formation-flying spacecraft using global-positioning-system measurements," *Journal of Guidance, Control, and Dynamics*, vol. 28, no. 2, pp. 226–235, 2005. DOI: [10.2514/1.7474](https://doi.org/10.2514/1.7474). eprint: <https://doi.org/10.2514/1.7474>. [Online]. Available: <https://doi.org/10.2514/1.7474>.

## 11 Appendix A: Code

All code for this project can be found in the following [GitHub repository](#).